

Научном већу Института за физику

Земун, 24 септембар 2020.

предмет: покретање поступка за реизбор у звање научни сарадник

Молим Веће да покрене процедуру за мој реизбор у звање научни сарадник. Молби  
прилажем:

сагласност руководиоца лабораторије

стручно--биографске податке

преглед научне активности

елементе за квалитативну оцену доприноса

елементе за квантитативну оцену доприноса

списак радова

списак цитата

копију решења о претходном избору у звање

У комисију предлажем:

Др. Радоша Гајића, научног саветника ИФ у пензији

Др. Александра Белића, научног саветника ИФ

Др. Зорана Кнежевића, редовног члана САНУ

С поштовањем,

Др. Владан Челебоновић

научни сарадник ИФ

Научном већу Института за физику

Земун, 24 септембар 2020.

предмет: мишљење о молби др. В.Челебоновића за покретање поступка за реизбор  
у звање научни сарадник

Др. Владан Челебоновић, научни сарадник Института за физику, запослен је у Лабораторији за физику материјала под екстремним условима и учествује у раду Лабораторије за графен чији сам руководиоца био до краја 2019. Бави се проблематиком транспортних и оптичких особина нискодимензионих материјала и фазним прелазима у материјалима под високим притиском. Веома мало му фали до испуњења услова за звање виши научни сарадник. Континуитета ради сагласан сам са његовом молбом за покретање поступка за реизбор у звање научни сарадник.

С поштовањем,

Др. Радош Гајић

Научни саветник ИФ у пензији

## 1. Стручно-биографски подаци

Владан Челебоновић рођен је 1955. године у Београду. Завршио је основну школу "Браћа Рибар", а затим Прву београдску гимназију. Дипломирао је на Физичком факултету 1982., магистрирао 1989. и докторирао 2001.

Од 1985. запослен је у Институту за физику у Лабораторији за интердисциплинарна истраживања, која се последњих година зове Лабораторија за физику материјала под екстрем -ним условима (ЛЕКС).

У периоду март-децембар 1987. био је у Паризу као стипендиста француске владе. Бора- вак је протекао у Лабораторији за молекулске интеракције и високе притиске

( L.I.M.H.P) Универзитета Париз 13. Циљ боравка било је овладавање лабораторијским техникама за истраживања под високим притиском.

Другу стипендију у Француској користио је у периоду октобар 1989.- новембар 1991. Овога пута боравио је у Лабораторији за физику чврстог стања Универзитета Париз 11 у Орсеју крај Париза. Прве године радио је у групи академика Д.Жерома (D.J  rome) на експериментима са квази једнодимензионим органским проводницима под високим притиском и на ниској температури. Друге године радио је у теоријској групи лабораторије са проф. Х.Ј.Шулцем ( H.J.Schulz). Циљ је било израчунавање електричне проводљивости органских проводника помоћу Хабардовог модела. Добијен је израз који садржи мерљиве параметре ових материјала, и који се добро слаже са експериментима. Као претходни корак, изведен је израз за хемијски потенцијал електронског гаса у 1Д, који се успешно наставља на светски познати резултат из литературе.

Средином деведесетих година кандидат је почео да развија контакт са Лоренцовим институтом Универзитета у Лајдену (Lorentz Institute, Leiden University) у Холандији. Овај контакт је на почетку био користан за библиотеку ИФ, јер су из Лајдена као донација директора института долазили бројеви једног од часописа који су тада недостајали у ИФ. Конкретно, реч је о Europhysics Letters. Сличних контаката и донација за библиотеку било је и са неколико других универзитета и института из САД а све у оквиру "Journal donation program" American Physical Society.

Веза са Лоренцовим институтом добила је научну димензију 2001. када је кандидат позван да посети институт и одржи семинар. Посета је довела до тога да је колега Челебоновић добио позив да одабере тему и учеснике и у Лајдену организује скуп. Осим тога, разговори кандидата са колегама у Лоренцовом институту у току те посете помогли су да троје студената из Београда буде примљено у Лајден на докторате.

Коорганизатори скупа били су проф. Вернер Депен (Werner Dappen, Univ. of Southern California, LA) и проф. Даглас Гоф (Douglas Gough, FRS, Univ. of Cambridge, UK). Тема су били фазни прелази у астрофизичкој материји, било је око 40 учесника а зборник радова публикован је као vol.731 серије AIP Conference Proceedings 2004. Први уредник је др. Челебоновић.

Кандидат од 2004. активно учествује у раду Летње школе физике чврстог стања коју у Варни у Бугарској организује Институт за физику чврстог стања Бугарске академије наука. Од 2010. је члан научног комитета школе а од 2004. држи предавања по позиву.

Од 2012. кандидат је отпочео контакте са Међународним центром за теоријску физику (ICTP) у Трсту. Први боравак је трајао неколико дана, а за 2019. годину било му је одобрено чак 7 недеља.

За 2020. му је одобрен боравак од 5 недеља. На жалост, све активности у ИСТР су до даљег отказане због пандемије корона вируса. У току сваког дужег боравка кандидат припреми по једну публикацију. У току боравка у зависности од потреба посла, у консултацији је са др. Михајлом Кисељевим из Одсека за физику кондензованог стања и статистичку физику ИЦТП. Поред онога што тражи МПНТР, на крају стоји и захвалност ИЦТП.

Vladan Čelebonović: radovi 2015.-2020.

M13

1. V. Čelebonović: Hubbard model in material science: electrical conductivity and reflectivity of models of some 2D materials izašlo kao poglavlje u knjizi "Advanced 2D Materials", ed. by A. Tiwari et al., pp.115 -144 Wiley-Scrivener Publishing LLC, USA (2016) ISBN 978-1-119-24249-9

<https://www.wiley.com/en-us/Advanced+2D+Materials-p-9781119242499>

2. V. Čelebonović: Material Science and Impact Crater Formation, poglavlje u knjizi "Horizons in World Physics": Volume 291, ed by A.Reimer, pp.251-267, Nova Science Publishers, New York, USA (2017), ISBN 978-1-53611-008-1

<https://novapublishers.com/shop/horizons-in-world-physics-volume-291/>

3. V. Čelebonović: The Hubbard Model: Some Applications to Nanomaterials, in: Advances in Nanotechnology, vol.22, pp.83-98, Ed. by Z.Bartul and J.Trenor, Nova Science Publishers, New York (USA) (2019), ISBN 978-1-53615-558-7

<https://novapublishers.com/shop/advances-in-nanotechnology-volume-22/>

M21

1. M. D Rabasović, B. D Murić, V. Čelebonović, M. Mitrić, B. M Jelenković and M. G. Nikolić : Luminescence thermometry via the two-dopant intensity ratio of Y<sub>2</sub>O<sub>3</sub>:Er<sup>3+</sup>, Eu<sup>3+</sup> J. Phys. D: Appl. Phys. **49** (2016) 485104 (6pp) doi:10.1088/0022-3727/49/48/48510

M22

1. V. Čelebonović, J. Pešić, R. Gajić, B. Vasić and A. Matković: Selected transport, vibrational and mechanical properties of low-dimensional systems under strain. J. of Appl. Phys., **125** 154301 (2019). <https://aip.scitation.org/doi/10.1063/1.5054120>

## M23

1. V. Čelebonović and M.G. Nikolić: Heating and Melting in Impacts: Basic Theory and Possible Applications, Int.J.Thermophys.,**36**, pp.2916-2921 (2015)  
<http://link.springer.com/article/10.1007/s10765-015-1936-x>
2. V. Čelebonović: Condensed Matter Analogy of Impact Crater Formation, Journal of Earth Science and Engineering, **5**,pp.44-51 (2015)  
<http://www.davidpublisher.org/index.php/Home/Article/index?id=6141.html>
3. V. Čelebonović and M.G. Nikolić: The Hubbard Model and Piezoresistivity, J.Low Temp.Phys.,**190** (3-4),pp.191-199 (2018).  
<https://link.springer.com/article/10.1007/s10909-017-1830-y>
4. V.Čelebonović: The origin of impact craters:some ideas,Bulgarian Astronomical Journal,**33**,pp. 20-29, (2020). <http://astro.bas.bg/AIJ/issues/n33/VCelebonovic.pdf>

## M24

V.Челебоновић: Павле Савић,Радивоје Кашанин и материјали под високим притиском, Флогистон, **23**,67-83 (2015) <https://www.scribd.com/doc/297729125/Flogiston-br-23>

## M31

1. V. Čelebonović: Some calculational improvements in applying the Hubbard model to nanomaterials; Lecture at the 19 ISSP Summer School, Varna, Bulgaria, August 29.- September 2 2016.; J.Phys.:Conf.Ser. **794** 012008 (2017). <https://doi.org/10.1088/1742-6596/794/1/012008>
2. V. Čelebonović and M.G.Nikolić: Theoretically choosing multifunctional materials; Lecture at the 20 ISSP Summer School, Varna, Bulgaria, September 3.-7. 2018.; J.Phys.:Conf.Ser. **1186** 012001 (2019) <https://doi.org/10.1088/1742-6596/1186/1/012001>

## M32

1. V. Čelebonović, “Strain-tunable conductivity and reflectivity of low dimensional systems within the Hubbard model” Book of Abstracts of 21 Internat.School of Cond.Matt.Phys “Progress and Perspectives in Functional Materials” p.29  
[http://iscmp.issp.bas.bg/images/BOOK\\_ABSTRACTS\\_21ISCOMP.pdf](http://iscmp.issp.bas.bg/images/BOOK_ABSTRACTS_21ISCOMP.pdf)

## M61

1. V. Čelebonović: , Condensed matter physics and impact crater formation; invited lecture na XVII National Conference of Astronomers of Serbia, Belgrade, 23.-27.September 2014.,Publ.Astron.Obs.Belgrade,**96**, 63-70 (2017).  
<http://publications.aob.rs/96/pdf/063-070.pdf>

## 1. Анализа научног рада кандидата

По тематици којом се баве, сви радови кандидата могу се поделити на следеће целине:

- Ниско димензиони системи
- Понашање материјала под високим притиском и примене у астрофизици
- Статистичка физика

У периоду 2015.- 2020. на који се односи овај извештај, кандидат се највише бавио нискодимензионим системима. За ове материјале заинтересовао се још у периоду када је као стипендиста боравио у Француској. Од тада је у овој области постигао важне резултате.

Извео је израз за хемијски потенцијал електронског гаса у 1Д, који се уклапа у познате резултате из литературе, а који омогућава да се узме у обзир зависност од притиска, допирања и температуре. Извео је израз за електричну проводљивост 1Д система, и нашао једоставан начин за његово проширење на 2Д системе. Бавио се оптичким особинама 1Д и 2Д система, и показао да је могуће теоријски предвидети зависност коефицијента рефлексије ових материјала од њихових мерљивих параметара.

Кандидат се на почетку каријере бавио истраживањем понашања материјала по високим притиском. У каснијим фазама рада заинтересовао се за проблем порекла тзв. сударних кратера и могућност одређивања особина импактора на основу мерљивих параметара тих кратера. Сударни кратери су резултат удаа о површину Земље малих тела. Кандидат је показао да је користећи стандардну физику кондензованог стања и мерене податке, могуће доћи до неких особина тела која су ударима направила те кратере. Поред чисто научног, ови радови имају и велик практични значај, јер постоји могућност да се деси такав удар у густо насељену област.

## Елементи за квантитативну анализу рада

Остварени бодови

| Категорија | М бодова<br>по раду | Број радова | Укупно бодова |
|------------|---------------------|-------------|---------------|
| M13        | 7                   | 3           | 21            |
| M21        | 8                   | 1           | 8             |
| M22        | 5                   | 1           | 5             |
| M23        | 3                   | 4           | 12            |
| M24        | 2                   | 1           | 2             |
| M31        | 3.5                 | 2           | 7             |
| M32        | 1.5                 | 1           | 1.5           |
| M61        | 1.5                 | 1           | 1.5           |
|            |                     | Збир        | 58            |

Поређење захтеваних и остварених бодова приказано је у следећој табели. Из ње се види да кандидат испуњава услов о потребном броју М бодова, а такође и да испуњава број бодова из обе обавезне комбинације бодова које мора да има.

|                             | Има | Треба |
|-----------------------------|-----|-------|
| Укупно М поена              | 58  | 16    |
| M10+M20+M31+M32+M33+M41+M42 | 53  | 10    |
| M11+M12+M21+M22+M23         | 25  | 6     |

## Елементи за квалитативну оцену рада кандидата

### 3.1 Квалитет

#### 3.1.1 Научни ниво и значај резултата

Из сваке од три области којима се кандидат бавио, издвајамо неколико радова за даљу анализу. У извештајном периоду објавио је укупно 11 радова различитих категорија, од радова у монографијама до абстракта саопштења на конференцијама.

По важности издвајамо следећих пет радова кандидата у извештајном периоду, поређаних хронолошки:

1. V. Čelebonović: Hubbard model in material science: electrical conductivity and reflectivity of models of some 2D materials izašlo kao poglavlje u knjizi “Advanced 2D Materials”, ed. by A. Tiwari et al., pp.115 -144 Wiley-Scrivener Publishing LLC, USA (2016) ISBN 978-1-119-24249-9.
2. M. D Rabasović, B. D Murić, V. Čelebonović, M. Mitrić, B. M Jelenković and M. G. Nikolić : Luminescence thermometry via the two-dopant intensity ratio of Y2O3:Er3+, Eu3+ J. Phys. D: Appl. Phys. **49** (2016) 485104 (6pp) [doi:10.1088/0022-3727/49/48/48510](https://doi.org/10.1088/0022-3727/49/48/48510) IF=2.829
3. V. Čelebonović: The Hubbard Model:Some Applications to Nanomaterials, in: Advances in Nanotechnology, vol.22, pp.83-98, Ed. by Z.Bartul and J.Trenor, Nova Science Publishers, New York (USA) (2019), ISBN 978-1-53615-558-7
4. V.Čelebonović, J.Pešić, R.Gajić, B.Vasić and A.Matković: Selected transport, vibrational and mechanical properties of low-dimensional systems under strain. J. of Appl. Phys., **125** 154301 (2019). <https://aip.scitation.org/doi/10.1063/1.5054120> IF=2.328
5. V.Čelebonović: The origin of impact craters:some ideas.  
Bulgarian Astronomical Journal., **33**, 21 (2020)  
<http://astro.bas.bg/AIJ/issues/n33/VCelebonovic.pdf>

Рад број 1 је приказ резултата које је кандидат постигао у претходне две деценије. Говори се о Хабардовом моделу, његовој примени на квази једно димензионе органске проводнике, размотрен је прелаз са 1Д на 2Д материјале, зависност електричне проводљивости од параметара материјала. Обрађен је проблем израчунавања коефицијента рефлексije материјала, и показано је да је могуће мењати га променама параметара материјала. По нашем мишљењу, овај рад представља одличан заокружен увод у проблематику Хабардовог модела и његових примена.



Рад број 2 је експериментални. Испитивана је фотолуминесценција у функцији температуре  $Y_2O_3:Er^{3+},Eu^{3+}$ . Циљ је био утврдити може ли овај материјал да се користи као сензор температуре. Узорци су побуђивани ласером таласне дужине 532nm у температурном интервалу  $303 \leq T[K] \leq 573$ . Показано је да релативна осетљивост овог сензора износи  $1.4\%K^{-1}$  на доњој граници испитиваног интервала температура, што га чини употребљивим у биолошким експериментима.

Рад број 3 је поново теоријски. Садржи преглед основних резултата о Хабардовом моделу и могућности његове примене у теоријском моделовању мултифункционалних нано материјала. Важно је истаћи да је у овом раду предложена геометријска идеја за рачунање електричне проводљивости дводимензионих материјала чија јединична ћелија није правоугаона.

Рад број 4 је прегледни, настао као резултат сарадње кандидата са сарадницима Лабораторије за графен у Институту за физику. Обухватио је теоријске прорачуне (Хабардов модел и ДФТ), нумеричке и експерименталне резултате. Све је рађено узимајући у обзир напрезање (strain) коме је материјал подвргнут. Показано је да критична температура за прелаз у суперпроводно стање расте са порастом напрезања. Рад је оцењен веома добро и од момента објављивања (април 2019. ) закључно са 19.07 2020. тражен је на сајту часописа чак 608 пута. О интересовању које је овај рад изазвао сведочи и чињеница да му је Амерички институт за физику (AIP) посветио посебно саопштење за јавност. <https://publishing.aip.org/publications/latest-content/strain-enables-new-applications-of-2d-materials/> .

У раду број 5 кандидат је обрадио познат проблем из области астрономије али на потпуно нов начин. Дуго се зна да на површини Земље постоје кратери који су резултат удара о површину тзв. малих тела, дакле језгара комета или делова астероида. Ови кратери се углавном анализирају користећи скалирање, дакле повезују се са кратерима насталим у вештачки изазваним експлозијама, где су сви услови познати. Кандидат је обрадио проблем користећи стандардну физику кондензованог стања. Метод који је разрадио применио је на неке познате случајеве и добио реалистичне резултате, у сагласности са познатим. По новом методу, разрађеном у детаље, овај његов рад први у нашој земљи, а један од ретких у свету.

Citati

Mihailo D Rabasović<sup>1</sup>, Branka D Murić<sup>1</sup>, Vladan Čelebonović<sup>1</sup>, Miodrag Mitrić<sup>2</sup>, Branislav M Jelenković<sup>1</sup> and Marko G Nikolić<sup>1</sup>

Published 7 December 2016

[Journal of Physics D: Applied Physics](#), [Volume 49](#), [Number 48](#),485104

citirano u:

2. [Improved photoluminescence, thermal stability and temperature sensing performances of K+ incorporated perovskite BaTiO<sub>3</sub>: Eu<sup>3+</sup> red emitting phosphors](#)

DK Singh, K Mondal, J Manam - *Ceramics International*,**43**,(16),13602 (2017) .

3. [Effects of temperature and pressure on luminescent properties of Sr<sub>2</sub>Ce: Eu<sup>3+</sup> nanophosphor](#)

A Vlastic, [D Sevic](#), [MS Rabasovic](#), J Krizan... - *J. of Luminescence*,**199**,285 (2018)

4. [Orange-Reddish Light Emitting Phosphor GdVO<sub>4</sub>: Sm<sup>3+</sup> Prepared by Solution Combustion Synthesis](#)

[MS Rabasovic](#), J Krizan, [S Savic-Sevic](#), et.al,- *Journal of Spectroscopy*,article id 3413864,**(2018)** (2018) - hindawi.com

5. [Luminescence and energy transfer in β-NaGdF<sub>4</sub>: Eu<sup>3+</sup>, Er<sup>3+</sup> nanocrystalline samples from a room temperature synthesis](#)

G.[Tessitore](#), [AVMudring](#), KW Krämer - *New journal of chemistry*, **42**,237 (2018) -

6.[Luminescence thermometry using Gd<sub>2</sub>Zr<sub>2</sub>O<sub>7</sub>:Eu<sup>3+</sup>](#)

MG Nikolic, [MS Rabasovic](#), J Krizan... - *Optical and Quantum Electronics*,**50**,258 ..., (2018)

MF Volhard, [T Jüstel](#) - *International Conference on ...*, 2017 - pdfs.semanticscholar.org

7. [Near Infrared-to-Near Infrared Excited-State Absorption in LaPO<sub>4</sub>: Nd<sup>3+</sup> Nanoparticles for Luminescent Nanothermometry](#)

[K Treigis, K Maciejewska...](#) - ACS Applied Nano Mater., **3**(5),4818 (2020)

[\[PDF\] unigoa.ac.in](#)

8. [Preparation, Characterization and Material Studies on Spinel Ferrites and Mixed Rare Earth Oxides](#)

CC Naik - 2019 - [irgu.unigoa.ac.in](#)

[http://irgu.unigoa.ac.in/drs/bitstream/handle/unigoa/5987/naik\\_c\\_c\\_2019.pdf?sequence=1](http://irgu.unigoa.ac.in/drs/bitstream/handle/unigoa/5987/naik_c_c_2019.pdf?sequence=1)

9. [\*\*YVO<sub>4</sub>: Eu<sup>3+</sup> nanopowders: multi-mode temperature sensing technique\*\*](#)

[D Sevic, MS Rabasovic, J Krizan...](#) - Journal of Physics **D53**,015106, 2019

<https://doi.org/10.1088/1361-6463/ab499f>

10. [\*\*Phosphor thermometry instrumentation for synchronized acquisition of luminescence lifetime decay and intensity on thermal barrier coatings\*\*](#)

Q Fouliard, J Hernandez, B Heeg... - Measurement Science and Technology,**31**,054007 (2020)

<https://doi.org/10.1088/1361-6501/ab64ac>

11. Carlos Zaldo Lanthanide-based luminescent thermosensors: From bulk to nanoscale

Advanced Nanomaterials,pp.335-379 (2018)

12. [Some possible astrophysical applications of diamond anvil cells](#)

astro-ph/9812374

Wyzga,P.: 2015,Influence of the sintering conditions on selected properties of TiN-TiB<sub>2</sub> composite, Works of the Institute of Advanced Manufacturing Technologies. Science notebooks, vol.91,p.125

<https://yadda.icm.edu.pl/baztech/element/bwmeta1.element.baztech-bc866b66-5057-43a0-a231-899273ad9d88>

**13.** V. Čelebonović, J. Pešić, R. Gajić, B. Vasić and A. Matković [Selected transport, vibrational, and mechanical properties of low-dimensional systems under strain](#)

J.of Appl.Phys., **125**,154301 (2019) <https://doi.org/10.1063/1.5054120>

Zbigniew Koziol<sup>1</sup>, Grzegorz Gawlik<sup>2</sup> and Jacek Jagielski<sup>1,2</sup>, 2019, Chinese Physics, **B28**, (9),096101.

Basic notions of static high pressure experiments

**14.** V. Čelebonović, The Hubbard model and optics: reflectivity of 1D and 2D systems, J.Phys.:Conf.Series,**398**,012009 (2012)

dato kao "further reading" u  
van den Brink, J. Travels in one dimension. *Nature Mater* **5**, 427–428 (2006).

**15.** V. Čelebonović and M.G.Nikolić, Theoretically choosing multifunctional materials, J.Phys.:Conf.Ser.,**1186** 012001 (2019).

dato kao "further reading" u Giamarchi, T. A firmer grip on the Hubbard model. *Nature* **545**, 414–415 (2017).

**16** V. Čelebonović, The Hubbard model: basic notions and selected applications, J.of Optoelectronics and Advanced materials, **11**,1135 (2009)

citirao Luka Pavešić, 2018, Simulating the Bose-Hubbard model in optical lattices, Univerzitet u Ljubljani,

[http://mafija.fmf.uni-lj.si/seminar/files/2017\\_2018/Pavesic\\_Luka\\_Simulating\\_the\\_Bose\\_Hubbard\\_model\\_in\\_optical\\_lattices.pdf](http://mafija.fmf.uni-lj.si/seminar/files/2017_2018/Pavesic_Luka_Simulating_the_Bose_Hubbard_model_in_optical_lattices.pdf)

17. Mihailo D Rabasović<sup>1</sup>, Branka D Murić<sup>1</sup>, Vladan Čelebonović<sup>1</sup>, Miodrag Mitrić<sup>2</sup>, Branislav M Jelenković<sup>1</sup> and Marko G Nikolić<sup>1</sup>

[Journal of Physics D: Applied Physics](#), [Volume 49](#), [Number 48](#),485104

citirali ga

D.Sevic,M.S.Rabasovic,J.Krizan,S.S.Sevic,M.D.Rabasovic,B.Marinkovic,

M.G.Nikolic, "Effects of temperature on luminescent properties of Gd<sub>2</sub>O<sub>3</sub>:Er,Yb nanophosphor"

2020 [Optical and Quantum Electronics](#), vol52(5),232 (2020)

DOI: 101007/s 11082-020-02348-y

18. . Mihailo D Rabasović<sup>1</sup>, Branka D Murić<sup>1</sup>, Vladan Čelebonović<sup>1</sup>, Miodrag Mitrić<sup>2</sup>, Branislav M Jelenković<sup>1</sup> and Marko G Nikolić<sup>1</sup>

[Journal of Physics D: Applied Physics](#), [Volume 49](#), [Number 48](#),485104

citirali ga

M.G.Nikolić,M.S.Rabasović,J.Križan,S.Savić

Šević,M.D.Rabasović,B.P.Rabasović,B.P.Marinković,A.Vlašić and D.Šević Luminescence thermometry using Gd<sub>2</sub>Zr<sub>2</sub>O<sub>7</sub>:Eu<sup>3+</sup>

[Optical and Quantum Electronics](#) **50**,258 (2018)

**19.** M.D.Rabasović,B.D.Murić,V.Čelebonović et al.,2016

D.Kumar,S.Kanchan,M.J.Manam,Effects of temperature and pressure on luminescent properties of Sr<sub>2</sub>CeO<sub>4</sub>:Eu<sup>3+</sup> nanophosphor

[Ceramics International](#),**43**(16),13602 (2017)

20. K.Trejgis,A.Bednarkiewicz and L.Marciniak [Engineering excited state absorption based nanothermometry for temperature sensing and imaging](#)

Nanoscale,**12**,4667 (2020)

21. [YVO4: Eu3+ nanopowders: multi-mode temperature sensing technique](#)

D Sevic<sup>1,3</sup>, M S Rabasovic<sup>1</sup>, J Krizan<sup>2</sup>, S Savic-Sevic<sup>1</sup>, M G Nikolic<sup>1</sup>, B P Marinkovic<sup>1</sup> and M D Rabasovic<sup>1</sup>

2019, J.Phys.D., **53**(1),015106

22 . [Phosphor thermometry instrumentation for synchronized acquisition of luminescence lifetime decay and intensity on thermal barrier coatings](#) Q Fouliard<sup>1</sup>, J. Hernandez<sup>1</sup>, B. Heeg<sup>2</sup>, R. Ghosh<sup>1</sup> and S. Raghavan<sup>1</sup> ,2020  
Measur.Sci.Technol,(**31**)5 054007\_s

23. [Luminescence and energy transfer in  \$\beta\$ -NaGdF<sub>4</sub>: Eu<sup>3+</sup>, Er<sup>3+</sup> nanocrystalline samples from a room temperature synthesis](#)

[New J. Chem.](#), **2018**, 42, **237-245**

G.Tessitore,A.-V.Mudring and K. W. Krämer

[Near Infrared-to-Near Infrared Excited-State Absorption in LaPO<sub>4</sub>: Nd<sup>3+</sup> Nanoparticles for Luminescent Nanothermometry](#)

K. Trejgis, K. Maciejewska, A. Bednarkiewicz , L. Marciniak\*

Acs.Appl.Nano Matter., **3** (5) 4818 (2020)

<https://doi.org/10.1021/acsanm.0c00853>

24. Jonathan Hunt, James Martin, Vanessa Rosing, Josh Winner and Henry E. Montgomery, Jr.\*

[Pressure-induced Ionization of Hydrogen: A Computational Project](#)

Chem. Educator,**19**, 384–389 (2014)

<http://chemeducator.org/bibs/0019001/19140384.html>

25. The Hubbard model: basic notions and selected applications

A Navarro Gallinad - 2017,<https://ddd.uab.cat/record/202564>

26. Nikolic, M.G., Rabasovic, M.S., Krizan, J. *et al.* Luminescence thermometry using  $\text{Gd}_2\text{Zr}_2\text{O}_7:\text{Eu}^{3+}$ . *Opt Quant Electron* 50, 258 (2018). <https://doi.org/10.1007/s11082-018-1529-6>  
citirali J.Phys.D,2016

27. Šević, D., Rabasović, M.S., Križan, J. *et al.* Effects of temperature on luminescent properties of Gd<sub>2</sub>O<sub>3</sub>:Er, Yb nanophosphor. *Opt Quant Electron* **52**, 232 (2020). <https://doi.org/10.1007/s11082-020-02348-y>

citirali J.Phys.D,2016

28. Nemes-Incze, P., Kukucska, G., Koltai, J. *et al.* Preparing local strain patterns in graphene by atomic force microscope based indentation. *Sci Rep* **7**, 3035 (2017). <https://doi.org/10.1038/s41598-017-03332-5>

Further reading:

- [Selected transport, vibrational, and mechanical properties of low-dimensional systems under strain](#)
- V. Celebonovic, J. Pesic, R. Gajic, B. Vasic, A. Matkovic

Journal of Applied Physics (2019)

29. Engineering excited state absorption based nanothermometry for temperature sensing and imaging†

[K. Trejgis](#), [A. Bednarkiewicz](#) and [L. Marciniak](#)

*Nanoscale*, 2020, **12**, 4667-4675

citirali J.Phys.D 2016

30. YVO<sub>4</sub>:Eu<sup>3+</sup> nanopowders: multi-mode temperature sensing technique

D Sevic<sup>1,3</sup>, M S Rabasovic<sup>1</sup>, J Krizan<sup>2</sup>, S Savic-Sevic<sup>1</sup>, M G Nikolic<sup>1</sup>, B P Marinkovic<sup>1</sup> and M D Rabasovic<sup>1</sup> Published 15 October 2019 • © 2019 IOP Publishing Ltd

[Journal of Physics D: Applied Physics](#), [Volume 53](#), [Number 1](#)



citirali J.Phys.D,2016

31. José Daniel Lago da Silva Neves Gouveia

Propriedades magnéticas de sistemas electrónicos  
quânticos com geometrias não-triviais

Magnetic properties of quantum electronic  
systems with non-trivial geometries

Tese apresentada à Universidade de Aveiro para cumprimento dos requisitos  
necessários à obtenção do grau de Doutor em Física, realizada sob a orientação  
científica do Doutor Ricardo Assis Guimarães Dias, Professor Auxiliar do  
Departamento de Física da Universidade de Aveiro.

Universidade de Aveiro Departamento de Física (2017)

<https://pdfs.semanticscholar.org/b48a/6cb7c327521d5fe33ba3f9e4731853869462.pdf>

citirao: V.Čelebonović,J.Optoel.Adv.Materials,**11**,1135 (2009)

32. S.Fazzini,L.Barbiero and A.Montorsi

Low energy quantum regimes of 1D dipolar Hubbard model with correlated hopping

J.Phys.:Conf.Series,**841**,012016 (2017)

"You may be interested in":

V.Čelebonović:Some calculational improvements in applying the Hubbard model to nanomaterials

J.Phys.:Conf.Series,**794**,012008 (2017)


# Selected transport, vibrational, and mechanical properties of low-dimensional systems under strain

Cite as: J. Appl. Phys. **125**, 154301 (2019); <https://doi.org/10.1063/1.5054120>

Submitted: 29 August 2018 . Accepted: 15 March 2019 . Published Online: 16 April 2019

V. Celebonovic , J. Pesic , R. Gajic, B. Vasic, and A. Matkovic 

## COLLECTIONS

 This paper was selected as Featured



View Online



Export Citation



CrossMark

## ARTICLES YOU MAY BE INTERESTED IN

[Terahertz monolithic integrated waveguide transmission lines based on wide bandgap semiconductor materials](#)

Journal of Applied Physics **125**, 151616 (2019); <https://doi.org/10.1063/1.5083097>

[Inter-valley phonon-assisted Auger recombination in InGaAs/InP quantum well](#)

Journal of Applied Physics **125**, 155703 (2019); <https://doi.org/10.1063/1.5085493>

[A perspective on topological nanophotonics: Current status and future challenges](#)

Journal of Applied Physics **125**, 120901 (2019); <https://doi.org/10.1063/1.5086433>



## Instruments for Advanced Science

Contact Hiden Analytical for further details:

**W** [www.HidenAnalytical.com](http://www.HidenAnalytical.com)

**E** [info@hiden.co.uk](mailto:info@hiden.co.uk)

[CLICK TO VIEW](#) our product catalogue

**Gas Analysis**

- dynamic measurement of reaction gas streams
- catalysis and thermal analysis
- molecular beam studies
- dissolved species probes
- fermentation, environmental and ecological studies

**Surface Science**

- UHV/TPD
- SIMS
- end point detection in ion beam etch
- elemental imaging - surface mapping

**Plasma Diagnostics**

- plasma source characterization
- etch and deposition process reaction kinetic studies
- analysis of neutral and radical species

**Vacuum Analysis**

- partial pressure measurement and control of process gases
- reactive sputter process control
- vacuum diagnostics
- vacuum coating process monitoring

# Selected transport, vibrational, and mechanical properties of low-dimensional systems under strain

Cite as: J. Appl. Phys. **125**, 154301 (2019); doi: [10.1063/1.5054120](https://doi.org/10.1063/1.5054120)

Submitted: 29 August 2018 · Accepted: 15 March 2019 ·

Published Online: 16 April 2019



View Online



Export Citation



CrossMark

V. Celebonovic,<sup>1,a)</sup> J. Pesic,<sup>2</sup> R. Gajic,<sup>2</sup> B. Vasic,<sup>2</sup> and A. Matkovic<sup>2,3</sup>

## AFFILIATIONS

<sup>1</sup>LEX Laboratory, Institute of Physics, University of Belgrade, Pregrevica 118, 11080 Belgrade, Serbia

<sup>2</sup>Graphene Laboratory, Center for Solid State Physics and New Materials, Institute of Physics, University of Belgrade, Pregrevica 118, 11080 Belgrade, Serbia

<sup>3</sup>Institute of Physics, Montanuniversität Leoben, Franz Josef Strasse 18, Leoben 8700, Austria

<sup>a)</sup>[vladan@ipb.ac.rs](mailto:vladan@ipb.ac.rs)

## ABSTRACT

The aim of the present paper is to discuss some recent results concerning the behavior of low-dimensional materials under strain. This concerns the electrical conductivity calculations of 1D structures under strain, within the Hubbard model, as well as *ab initio* investigations of phonon, electron-phonon, and superconducting properties of doped graphene and MgB<sub>2</sub> monolayer. Two different experimental approaches to strain engineering in graphene have been considered regarding local strain engineering on monolayer flakes of graphene using atomic force microscopy and dynamic plowing lithography technique as well as the effects of mechanical straining on liquid phase exfoliated graphene and change of sheet resistance of graphene films.

Published under license by AIP Publishing. <https://doi.org/10.1063/1.5054120>

## I. INTRODUCTION

Strain engineering is widely used in materials science to tune various properties of materials and eventually enhance the performance of devices. Engineering of strain in low-dimensional materials promises to revolutionize the field of nanotechnology with the possibility of creating new artificial materials. Two-dimensional materials are a remarkable ground to study the influence of strain, as they can sustain very large deformations without breaking. The unique mechanical properties of graphene present an excellent opportunity for research of strain-induced modifications; for example, graphene is the strongest 2D material ever measured, with Young's modulus of 1 TPa and an intrinsic strength of 130 GPa.<sup>1</sup> What is more important is its ability to sustain reversible elastic tensile strain as large as 25%<sup>1</sup> and this allows the possibility for strain engineering in order to modify or tune graphene properties for specific applications. Since its discovery in 2004 with the size of a micrometer,<sup>2</sup> graphene has attracted increased attention. It is a truly two-dimensional (2D) plane of sp<sub>2</sub>-hybridized carbon atoms arranged in a honeycomb lattice. The unit cell has two identical

carbon atoms giving rise to electronic linear dispersion near the Fermi level and peculiar massless electron dynamics governed by the Dirac–Weyl relativistic equations.<sup>3,4</sup> This unique lattice of graphene leads to many extraordinary properties that include exceptionally high charge carrier mobility,<sup>2,3</sup> high mechanical strength and elasticity,<sup>1,5</sup> optical transparency,<sup>6,7</sup> and a wide variety of possible chemical modifications.<sup>8–10</sup> All of these properties make graphene an ideal material to investigate not only fundamental scientific problems in condensed matter physics, but also practically a wide variety of applications including flexible electronics,<sup>11–14</sup> optoelectronics,<sup>15,16</sup> sensors, and transistors.<sup>17,18</sup> The outstanding stretchability of graphene has made it suitable for application in flexible electronic devices as well as in superconducting electronics based on 2D materials since the electron-phonon (e-ph) coupling is greatly enhanced by the biaxial strain causing the change of superconducting critical temperatures.<sup>19–23</sup>

In this paper, we study and discuss selected transport, vibrational, and mechanical properties of low-dimensional systems under strain with the main focus on strain-induced changes on

conductivity. In Sec. II, we present theoretical approaches for strain engineering in low-dimensional systems. Section II A discusses the effects of the application of strain on conductivity studied in the one-dimensional Hubbard model. Section II B presents the *ab initio* study of the effects of the biaxial strain on doped graphene and isostructural new material  $\text{MgB}_2$  monolayer, namely, both materials are considered superconducting,<sup>24–26</sup> and here it is demonstrated that biaxial strain can cause softening of the phonons, affecting the total electron-phonon interaction and resulting in a significantly higher critical transition temperature. These two-dimensional materials not only share a similar structure, a hexagonal structure with an adatom in the center of a hexagon, but also have a similar electronic structure, and very interestingly, both are electron-phonon mediated superconductors.<sup>1,34–39</sup> Engineering of strain in those materials opens the road to new artificial structures with the improved electron-phonon coupling and higher critical temperatures.

Application of the strain in graphene and 2D materials is an intensively studied topic, both theoretically and experimentally;<sup>1,40,41</sup> for example, application of the strain on graphene can induce changes in the vibrational properties,<sup>42,43</sup> in the electronic bandgaps<sup>44,45</sup> and significant changes in conductivity at both local and macroscopic levels.<sup>46–48</sup> The type of the strain is a very important feature, since the graphene lattice symmetry determines its band structure. The breaking of the hexagonal symmetry will modify the band structure of graphene,<sup>49,50</sup> causing the opening of the bandgap and many other effects.<sup>51,52</sup>

In intercalated graphene, it is known that not all types of intercalant atoms produce superconductivity or significantly increase  $T_c$ . In Li-intercalated graphene (Li-GIC), a strong confinement for electrons along the z-axis exists and it prevents the occupation of the interlayer state. In the monolayer,<sup>24,35</sup> there is a significant reduction of a charge transfer that is beneficial for superconductivity. The charge transfer from the interlayer state formed by the presence of the adatom is a crucial ingredient. Though it is necessary, the completion of the charge transfer is deleterious for the enhancement of the superconductivity.<sup>24,35</sup> For example, in the Li-GIC, a strong confinement along the z-axis exists and it prevents the occupation of the interlayer state. When the quantum confinement is removed as in the monolayer, it results in the reduction of charge transfer which is beneficial for the superconductivity. In Sec. III, we discuss the effects of strain, as shown above, on the most prominent example of low-dimensional materials, graphene.

We present two different experimental approaches to strain engineering in graphene. In Sec. III A, we discuss local strain engineering on monolayer flakes of graphene produced by micromechanical exfoliation using atomic force microscopy (AFM) and dynamic plowing lithography (DPL). In Sec. III B, we present the effects of mechanical straining on the liquid phase exfoliated graphene and the change of sheet resistance graphene films obtained in that way. These two techniques are diametrically different, both in results and in the procedure. Micromechanical exfoliation is a clean technique where high-quality, well-defined monolayer samples are produced using the Scotch tape method.<sup>1</sup> However, samples produced this way though very pure, ideal monolayer without vacancies, are small in scale (maximally, hundreds of

micrometers), making this technique excellent for state-of-the-art nanodevices and fundamental research. Nonetheless, for applications, especially macroscopic ones, this kind of production technique is not applicable. Liquid phase exfoliation (LPE) is an alternative where solution processing of graphite flakes breaks van der Waals forces creating liquid graphene dispersion. Samples produced from this dispersion can be very large in scale, macroscopic; however, they are not monolayers, but few-layer graphene flakes overlap in between forming graphene films.<sup>27,28</sup> We study how strain can be engineered in both samples, where in the first experimental section we focus more on a fine technique for the induction of the local strain in monolayer samples, and in the second one, where strain can be induced and engineered in a much more simple way (since we can work with macroscopic samples), the spotlight is on the effect of the strain quality of the film and eventually on sheet resistance, hence conductivity. Straining the monolayer graphene sample shows that a high enough local pressure induced by an AFM tip will result in protrusion at a neighboring point. The generated local strain introduced in this way is well controlled, and it is expected to affect conductivity along protrusion. The other presented case, the sample of which is produced in LPE, shows the change of resistivity with the application of strain, as it is presented that this is not the intrinsic strain of single graphene flakes but is more of a macroscopic effect. The small flakes that the film consists of are deposited onto the elastic substrate, and when mechanical strain is applied, the substrate surface stretches but individual flakes do not get strained. The total resistance of LPE films comes from the points of the overlap between neighboring flakes, and stretching the LPE graphene film results in effective pulling apart of individual flakes, and thus an increase in the sheet resistivity of the whole film (and vice versa).

## II. THEORY

### A. Effects of strain on the conductivity in 1D system—The Hubbard model study

Toward the middle of the last century, the metal to insulator transition was one of the outstanding problems of condensed matter physics. A general model of the metal to insulator transition was proposed by John Hubbard, in a series of papers starting from Ref. 29. Apart from the metal to insulator transition, the Hubbard model has found applications in studies of transport processes in 1D and 2D correlated electron systems. These calculations have often been performed using the memory function method. A detailed review is available in Ref. 30, while the main results are given in the following.

The initial point for a study of the transport properties of any system is the knowledge of its Hamiltonian. Using the second quantization formalism, the Hamiltonian of the 1D Hubbard model has the following form:

$$H = -t \sum_{i=1, \sigma}^N (c_{i+1, \sigma}^\dagger c_{i, \sigma} + c_{i, \sigma}^\dagger c_{i+1, \sigma}) + U \sum_l n_{l, \uparrow} n_{l, \downarrow}. \quad (1)$$

The symbols  $N$ ,  $t$ , and  $U$  denote the number of nodes in a lattice, the mean kinetic energy of the electrons (the so-called hopping

energy), and the interaction energy of pairs of electrons with opposing spins on the same lattice node;  $\sigma$  stands for the electron spin. The symbols in the parenthesis denote the creation and annihilation operators.

Calculations of the electrical conductivity have been performed using the memory function method.<sup>30</sup> These basic expressions are

$$\chi_{AB} = \ll A; B \gg = -i \int_0^\infty e^{izt} \langle [A(t), B(0)] \rangle dt, \quad (2)$$

$$\sigma(\omega) = i \frac{\omega_p^2}{4\pi z} \times \left[ 1 - \frac{\chi(z)}{\chi(0)} \right]. \quad (3)$$

The symbol  $\omega_p^2 = \frac{4\pi n_e e^2}{m_e}$  denotes the square of the plasma frequency

and  $\chi_0 = \frac{n_e}{m_e}$  is the zero frequency limit of the dynamical susceptibility.

Expression (2) is the general definition of the linear response of a physical quantity corresponding to operator  $A$  to the perturbation by another physical quantity described by operator  $B$ .  $A(t)$  denotes the Heisenberg representation of operator  $A$ . Inserting  $A = B = [j, H]$ , with  $j$  denoting the current operator and  $H$  the Hamiltonian, leads to the definition of the current-current correlation function. Details of the calculation of the electrical conductivity are presented in Ref. 30. The final result is

$$\sigma_R(\omega_0) = \left( \frac{1}{2\chi_0} \right) \left( \frac{\omega_p^2}{\pi} \right) \frac{1}{\omega_0^2 - (bt)^2} \left( \frac{Ut}{N^2} \right)^2 \times S, \quad (4)$$

where  $S$  denotes the following function:

$$S = \frac{42.49916}{(1 + \exp[\beta(-\mu - 2t)])^2} + \frac{78.2557}{(1 + \exp[\beta(-\mu + 2t) \cos(1 + \pi)])^2} + \frac{bt}{\omega_0 + bt} \left[ \frac{4.53316}{(1 + \exp[\beta(-\mu - 2t)])^2} + \frac{24.6448}{(1 + \exp[\beta(-\mu + 2t) \cos(1 + \pi)])^2} \right]. \quad (5)$$

The symbol  $\mu$  denotes the chemical potential of the electron gas on a 1D lattice, given by the following (Ref. 30 and references therein):

$$\mu = \frac{(\beta t)^6 (ns - 1) |t|}{1.1029 + 0.1694(\beta t)^2 + 0.0654(\beta t)^4}. \quad (6)$$

*The practical calculation of the conductivity:* Inserting values of material parameters into Eqs. (4)–(6) leads to the electrical conductivity expressed as a function of these parameters. Some examples of such calculations have been discussed in Refs. 32–35 and references therein.

As this paper focuses on nanomaterials under strain, this section considers the problem of treating the material under strain within the Hubbard model. This problem is not only of academic, but also of practical, interest. There already exist examples of stretchable electronics (some examples are given in Refs. 31 and 33). By changing an initial material length from  $l_0$  to  $l$ , the strain is defined as

$$\varepsilon = \frac{l - l_0}{l_0}. \quad (7)$$

If a material is subdued to nonzero strain, the overlap between wave functions of electronic wave functions in adjacent atoms changes, leading to changes in the hopping energy and all material parameters which contain the lattice constant. The dependence of the hopping on the interatomic distance is represented by<sup>31</sup>

$$t = t_0 \times \left[ 1 + r + \frac{1}{3} r^2 \right] \exp[-r], \quad (8)$$

where the distance is expressed in Bohr radii.

All expressions used in the calculations discussed in this section are analytically tractable but too long to be explicitly stated here. Therefore, only a few resulting graphs are presented (Fig. 1).

Figure 1 shows the electrical conductivity of a 1D Hubbard model expressed as a function of the strain to which it is exposed. The data are normalized to 1 at  $n = 1.25$ ,  $t = 0.01$ ,  $T = 116$ ,  $\varepsilon = 0$ .

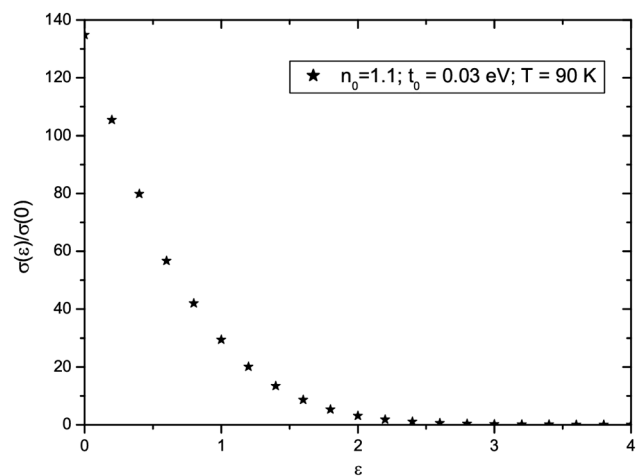


FIG. 1. Normalized conductivity of 1D HM as a function of strain.

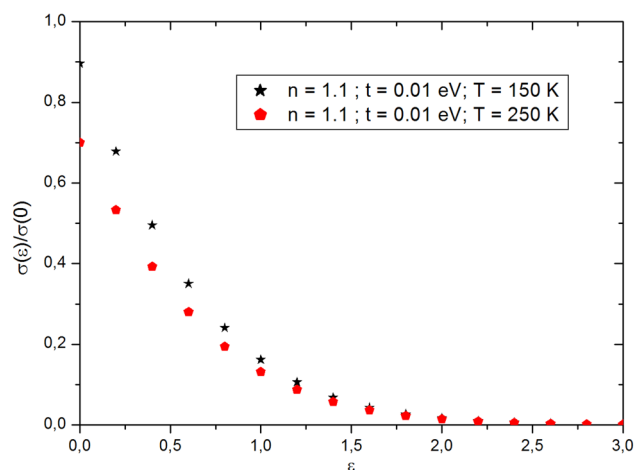


FIG. 2. Normalized conductivity for  $T = 150$  K and  $T = 250$  K.

Figure 2 taken from Ref. 31 shows the behavior of the conductivity for two values of the temperature  $T$ . It could be objected here that extending the value of the strain up to  $\epsilon = 3$  in Fig. 2 is unphysical, as no real material can withstand such a large value of strain. Indeed, this should be understood just as a mathematical extension. The values of various constants needed for the calculation leading to Fig. 2 are given in Ref. 31.

Figure 3 shows the normalized conductivity for a fixed value of the strain,  $\epsilon = 0.05$ , and the band filling factor,  $n = 0.9$ . The conductivity is normalized to 1 at  $T = 116$  K,  $n = 1.25$ .

Note that there is a big difference in the behavior of curves presented in Figs. 2 and 3. The curve in Fig. 3 changes sign at a certain point (at  $T \cong 100 - 110$  K).

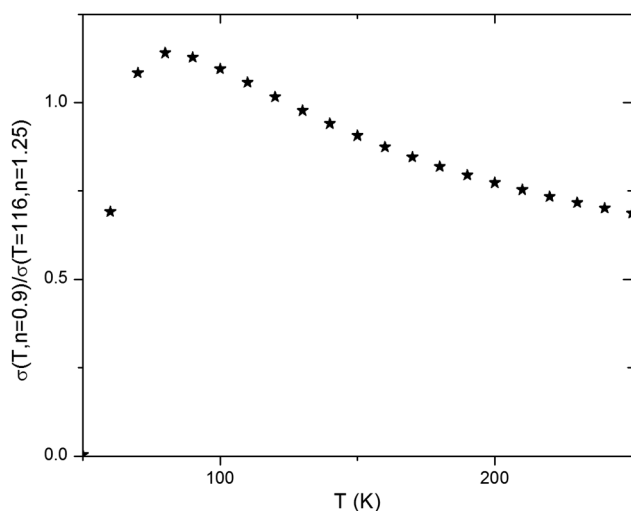


FIG. 3. Normalized conductivity for strain 0.05.

This result has considerable theoretical importance. Namely, practical attempts in applications of stretchable and flexible electronics may require such changes of material characteristics for different sets of material parameters. Therefore, results presented here, and some more which are forthcoming, can contribute to the development of various applications.

## B. Strain effects on vibrational properties in 2D structures—*Ab initio* calculations

In this section, we study the effect of strain on vibrational properties and electron-phonon coupling in two-dimensional materials. The low-dimensional materials are characterized by strong covalent in-plane bonds and weak interlayer van der Waals interactions which give them a layered structure. An application of homogenous strain in bulk materials would be practically impossible outside of the theoretical discussion, and in low-dimensional material, it is rather simple.

Based on this concept, we present computational study within the density functional theory framework of the effects of the (equi) biaxial strain on the two isostructural two-dimensional materials, Li-intercalated graphene and magnesium-diboride monolayer. We used Quantum Espresso software package<sup>53</sup> with both local-density approximation (LDA) and generalized gradient approximation (GGA) Perdew-Burke-Ernzerhof (PBE) functionals and vibrational properties and the electron-phonon interaction is calculated using density functional perturbation theory implemented in this software package.

Here, it is shown that tensile biaxial strain causes softening of the phonons, affecting the total electron-phonon interaction and resulting in significantly a higher critical temperature. In particular, in Li-doped graphene, the in-plane phonons will be dramatically softened, whereas the out-of-plane ones will be less affected.<sup>52</sup> By application of strain, we achieve the increase of the density of states at the Fermi level and softening of the modes.<sup>54,55</sup> Without drastically modifying the structure, this results in great effects on the electron-phonon coupling constant.<sup>55,56</sup> In principle, both these effects can be achieved rather easily in low-dimensional systems.

In order to strain the  $\text{LiC}_6$ -mono and increase the lattice constant, the in-plane distance between C atoms is increased leaving the hexagonal symmetry unaffected. The Li adatom is placed above the H site in graphene (the center of a hexagon). The modification of the lattice constant does not interfere with the Li adatom position which remains fixed in the center of the hexagon, leaving the symmetry unbroken. Due to the expansion of the carbon atom distances and the invariance of the hexagonal symmetry the Li adatom shifts only along the z-axis. The change in the distance between the carbon plane and the Li adatom is presented in Table I. The obtained results are in agreement with other similar studies and experimental results.<sup>24,36,54</sup>

The effects of several values of the strain, which increase the lattice constant by 3%, 5%, 7%, and 10%, are studied. Larger strains are not applied due to the instabilities that occur after the attempt of geometrical optimization and relaxation.<sup>57</sup> The distance between the Li adatom and graphene decreases with the strain, as the Li adatom moves down deeper toward graphene. When the strain is applied, the distance between neighboring C atoms increases and the graphene pi bonds repulse the Li adatom less, which then

**TABLE I.** Changes of bond lengths in Li-doped graphene with application on tensile equibiaxial strain.

| Strain % | Distance between Li adatom and carbon layer (Å) | Carbon-carbon bond length (Å) |
|----------|---|-------------------------------|
| 0        | 1.80  | 1.42                          |
| 3        | 1.69  | 1.46                          |
| 5        | 1.64  | 1.49                          |
| 7        | 1.61  | 1.52                          |
| 10       | 1.54  | 1.57                          |

moves down along the z-axis. The small shift of the Fermi level is observed with the strain.

In the phonon dispersion spectrum of doped graphene, the three regions can be distinguished: the adatom-related modes are associated with low-energy regions ( $0\text{--}400\text{ cm}^{-1}$ ), where  $300\text{--}400\text{ cm}^{-1}$  are Li modes mixed with the out-of-plane carbon modes ( $C_z$ ), the midregion ( $400\text{--}900\text{ cm}^{-1}$ ) can be associated with  $C_z$  modes and the high-energy region with carbon-carbon stretching modes.<sup>1</sup>

The main contributions to lambda come from the low-energy lithium modes and the carbon vibrations along the z-axis, with an additional contribution from the C-C stretching modes (in agreement with Refs. 24 and 35). When strain is applied, significant softening of phonons occurs, as shown in Fig. 4. In green color, phonon dispersion is depicted for the 3% strained  $\text{LiC}_6$ -mono and in red for 10%. The softening of the high-energy C-C stretching modes is strongly present with a larger strain. In addition, the consequent increase of the phonon DOS in the low-energy region occurs as well. Although the low-energy modes slightly move upwards in energy, the main effect on the electron-phonon coupling is the softening of graphene high-energy C-C stretching modes.

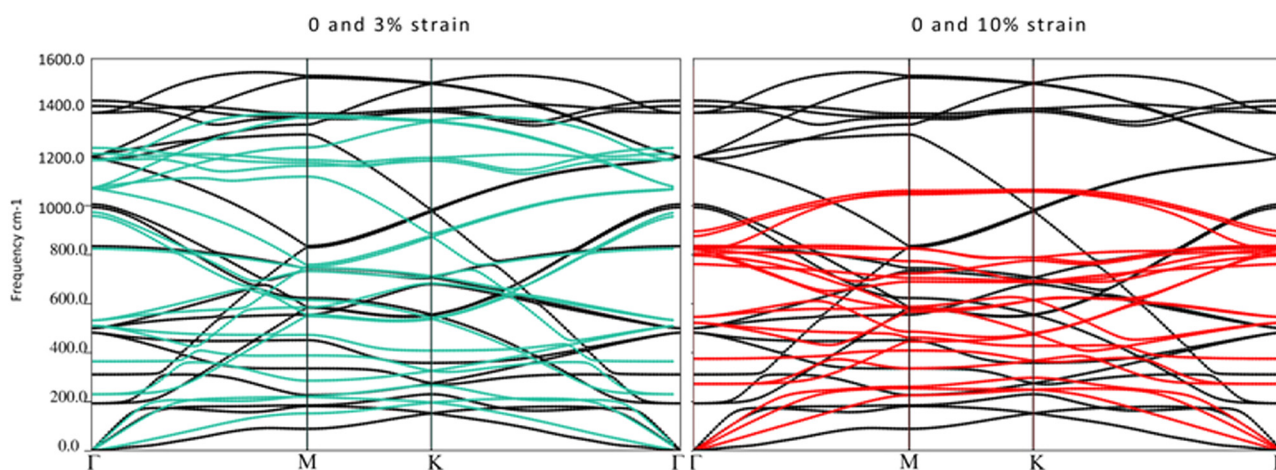
At the same time, with stretching of C-C bonds, another structural change occurs. For the small strain, the Li adatom drops

down toward the center of a hexagon and its orbitals overlap more with the carbon  $\pi$  orbitals. That causes an increase in charge transfer and emptying of the interlayer band, which reduces  $\lambda$ . When more strain is applied, the carbon bonds are elongated and the  $\pi$  orbitals move away, both from each other and the center of the hexagon. The orbital overlap is reduced, and after the certain critical value,  $\lambda$  increases, following the strain. Figure 5 presents the effects of the different strain on electronic localization function (ELF).

The significant changes for the large strain are presented, depicting the above-described effects. For ELF at 10% of the strain, the electron localization region is greatly lowered as graphene and adatom separate one from another and as a C-C bond are elongated. The critical temperature is enhanced with straining of structure, up to  $T_c = 29\text{ K}$  where the electron-phonon coupling constant is  $0.73$ .<sup>34</sup> It is important to stress that this increase in  $T_c$ , achieved by the described mechanism, can be experimentally realized. A pristine graphene is experimentally confirmed to be elastically stretchable up to 25%<sup>1</sup> making here considered strains feasible.

Following structural and electronic similarity we explored the effect of the biaxial strain on the  $\text{MgB}_2$  monolayer.<sup>25</sup> As in graphene the application of the biaxial strain leaves the symmetry of the system unchanged, yet a tensile (compressive) strain moves boron atoms further (closer) from (to) each other in the same proximity, allowing the Mg atom to move along the z-axis. This causes a change in the charge transfer from the magnesium atoms to the boron plane increasing (decreasing) DOS on the Fermi level. The other effects concern the softening (hardening) of modes of the boron atoms due to an elongation (compression) of the B-B bonds.

We compare phonon dispersion for nonstrained  $\text{MgB}_2$ -mono with compressively and tensely strained ones (Fig. 6). Significant softening (hardening) of high-energy modes is present with elongation (compression) of bonds between boron atoms, following the general trend for phonons, as distances between atoms increase, the interatomic bonds become less stiff, resulting in a decrease

**FIG. 4.** Phonon dispersion for the  $\text{LiC}_6$ -mono; black lines are for the nonstrained  $\text{LiC}_6$ -mono, and green and red for the 3% and 10% tensile biaxial strain, respectively.



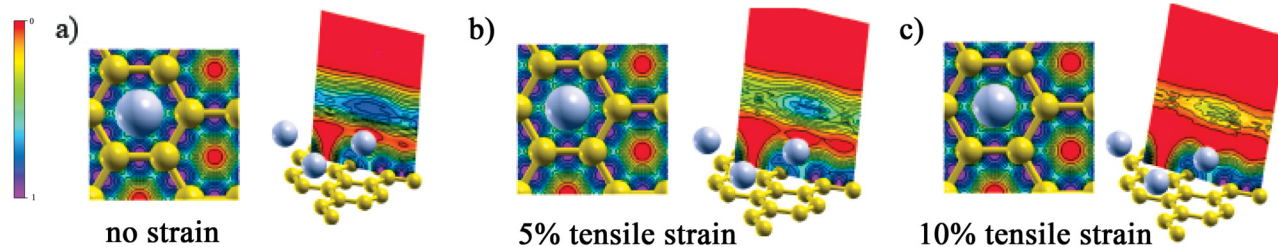


**FIG. 5.** ELF (electron localization function) for the  $\text{LiC}_6$ -mono without (a) and with strain [5% (b) and 10% (c)] (first image in pair ELF on the  $xy$  direction, second, ELF on the  $xz$  direction).

of phonon frequencies (and vice versa). In electron-phonon coupling strongest contribution to coupling comes from  $E_2$  optical mode.<sup>37,38</sup>

In Fig. 6, a significant shift of  $E_2$  mode is visible, it changes frequency for almost  $100 \text{ cm}^{-1}$  with the application of strain. However straining of structure results same as in graphene, not only in a variation of B-B bonds occurs but as well position of Mg adatom above the center of boron hexagon changes. As the distance between B atoms increases (i.e., for tensile strain) Coulomb repulsion is reduced allowing Mg atom to sink deeper towards the center of the hexagon. For compression opposite situation occurs. The repulsion is stronger and the Mg atom gets more remote. This has an effect on charge transfer from Mg to B layer.

To investigate this we study electron localization function (ELF). It is noticeable that straining not only affects ELF in the B layer but as well on the Mg layer. For both compressive and tensile strain in the Mg layer, ELF becomes denser than in the non-strained case. Due to the closing of B atoms in hexagon ELF increases B plane increases for compression (and vice versa) (Fig. 7). As in  $\text{LiC}_6$ -mono application of the biaxial strain dramatically increases critical temperature, more than 30 K.<sup>25,26</sup>

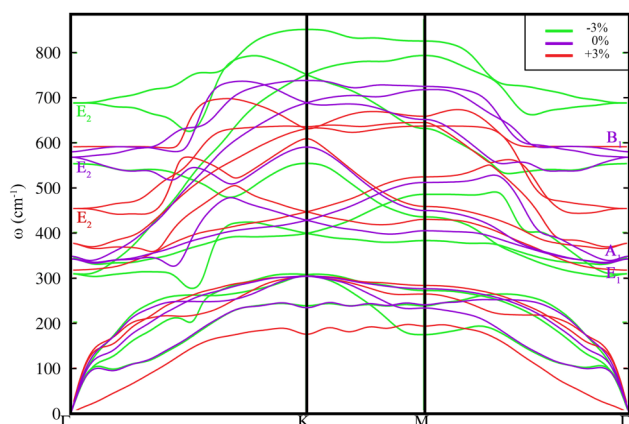


**FIG. 6.** Comparison of phonon dispersion for nonstrained  $\text{MgB}_2$  (violet) and compressively (green) and tensely (red) strained (for 3% each).

The question of the reduction of dimensionality of superconducting materials to its limit, a truly atomic-scale 2D system and the consequence of this<sup>57–62</sup> are highly relevant not only to fundamental science but to nanotechnology and it will be crucial for the production of superconducting devices in future. Engineering of strain in such systems could lead to significant improvements in their superconducting properties and pave the way toward new applications.

### III. EXPERIMENT

#### A. Local strain engineering of graphene by atomic force microscopy

A typical way to introduce a local strain into graphene is its transfer on a prepatterned substrate, containing, for example, arrays of nanopillars.<sup>63</sup> Atomic force microscopy (AFM) based lithography offers additional possibilities for graphene reshaping and patterning at the nanoscale. The typical curvature radius of AFM tips is around 5–10 nm making them appropriate for the fabrication of various graphene nanostructures, based on either AFM scratching<sup>64</sup> or AFM based local anodic oxidation.<sup>64–66</sup> In a similar way, a local strain can be introduced into the graphene lattice by applying a local pressure from AFM tips without graphene tearing.<sup>67,68</sup>

Our approach to generating a local strain in graphene is based on the AFM dynamic plowing lithography (DPL),<sup>68</sup> employing the so-called tapping AFM mode. In this mode, the AFM cantilever oscillates above a sample during scanning. The amplitude of the cantilever oscillations, represented by the amplitude set-point, is kept constant during scanning in the tapping mode. In order to hold constant the interaction between the AFM tip and the sample, the AFM scanner together with the sample moves up and down, in the  $z$ -direction according to the sample topography. Then, the scanner movement in the  $z$ -direction is proportional to the sample topography. On the other hand, during DPL, it is necessary to increase the mechanical interaction between the AFM tip and the considered sample in order to induce local changes in morphology. For this purpose, in order to increase a tip-sample interaction needed for graphene deformation, the free oscillation amplitude of the employed AFM cantilevers is first increased by around 10 times. The tip-sample interaction, controlled by the amplitude set-point in the tapping AFM mode, is then additionally increased by decreasing the set-point by 10–100 times compared to ordinary

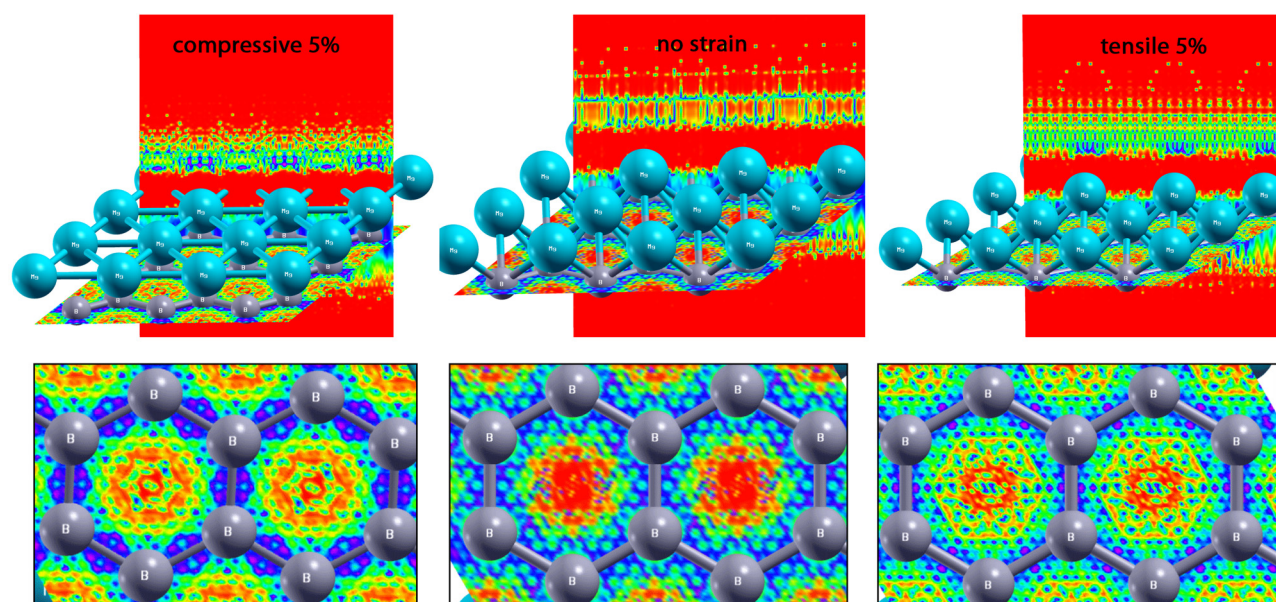


**FIG. 7.** Electron localization function (ELF) for  $\text{MgB}_2$ -mono nonstrained and compressively (left) and tensely (right) strained. Top: 3D projection of ELF with focus on the Mg layer. Bottom: ELF projection on the B layer.

AFM imaging. Benefits of using DPL instead of more traditional AFM scratching lithography stem from the fact that the AFM cantilever is vibrating and not in continuous contact with a sample surface, as in the case of the static plowing (AFM based scratching lithography) employed using the AFM contact mode. As a result, the lateral and friction forces between the AFM tip and the sample surface are minimized, so there is no undesirable dragging, pushing, and pulling of graphene sheet during DPL. At the same time, the AFM cantilever during DPL is free from a torsion caused by lateral forces, which facilitates the fabrication of nanostructures with well-defined edges. AFM imaging and DPL were done using the NTEGRA Prima measuring system, manufactured by NT-MDT ([www.ntmdt-si.com](http://www.ntmdt-si.com)). Since the lithography is based on the mechanical tip-sample interaction, we used robust and wear resistant diamond coated DCP20 probes from NT-MDT.

The selected nanostructures fabricated by DPL of graphene are presented in Fig. 8. All graphene samples were made by the standard mechanical exfoliation onto the Si/SiO<sub>2</sub> substrate. The local strain in graphene can be generated along straight and curved trenches as depicted in Figs. 8(a) and 8(b), respectively, whereas more complex structures can be made by overlapping basic patterns, as presented in Fig. 8(c). DPL can be also used for the fabrication of point-like deformations of graphene, as shown in Fig. 8(d). These deformations were made by local amplitude-distance curves in the tapping mode, with an increased free oscillation amplitude of the employed AFM cantilever and with decreased set-point in order to increase the tip-sample interaction. During the measurement of the amplitude-distance curves, there is no lateral movement and scanning, just a vertical movement of the AFM scanner holding a sample, which finally gives point-like local strain in graphene.

Common for all fabricated nanostructures is a smooth surface without bumps, protrusions, or cuts, implying that the graphene together with the underlying silicon-dioxide substrate is just locally deformed and strained. The only exception is presented in Fig. 8(c) where a small bump appeared parallel and next to the graphene trench. This example shows that for a high enough local pressure,

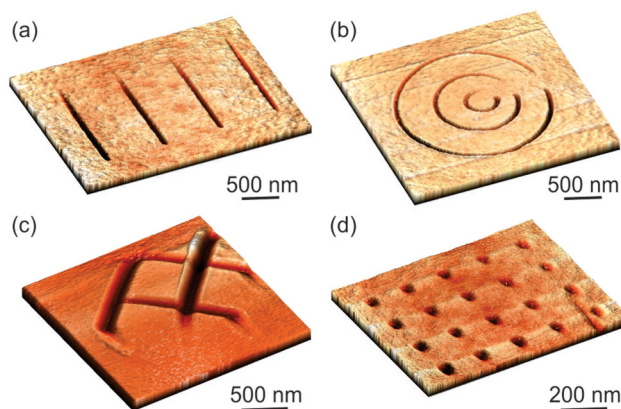


**FIG. 8.** Local strain in graphene nanostructures generated by DPL: (a) straight (z-height 3 nm) and (b) curved trenches (z-height 7 nm), (c) a more complicated pattern obtained by crossing straight trenches (z-height is 11 nm), and (d) point-like local deformation made by DPL during the measurement of amplitude-distance curves in the tapping AFM mode (z-height is 3.5 nm).

the sample compression at one point inevitably results in a protrusion at an adjacent point.

The local strain generated in graphene sheet in percent can be estimated according to the formula  $(L - L_0)/L_0 \times 100\%$ ,<sup>68</sup> where  $L_0$  and  $L$  are the lengths of graphene segments before and after the deformation by DPL, respectively. Therefore,  $L_0$  and  $L$  can be then considered as the graphene trench width and perimeter, respectively, and the values of which can be approximately calculated from measured AFM topographic images (the perimeter can be calculated from the measured trench width and perimeter). For the typical trench widths and depths of around 50–100 nm and several nanometers, respectively, the generated local strain in graphene is in the order of 0.1%. The trench width is dominantly determined by the AFM probe width. In the considered case, since we employed DCP20 probes with a rather large tip radius curvature of 50–70 nm, probably it would not be possible to make narrower trenches. Produced trenches in graphene could be an excellent platform in order to study local changes in graphene conductivity due to strain.<sup>87,88</sup>

## B. Axial strain in liquid phase exfoliated graphene films

Many potential applications of graphene and other 2D materials<sup>27,69,70</sup> rely on continuous films, either polycrystalline or single crystals. Chemical vapor deposition (CVD) techniques are commonly the fabrication methods of choice when large area graphene is considered.<sup>71–73</sup> However, CVD based films require a transfer from a catalyst on which these are grown onto a targeted substrate for their application. Usually, this step introduces many undesired features in the films, such as cracks, wrinkles, and transfer residues, and hinders intrinsic properties of graphene.<sup>74,75</sup>

A low-cost alternative to large area CVD graphene films is based on solution processing of either graphene oxide or graphite flakes.<sup>28,74–80</sup> In particular, LPE using solvers that do not covalently bond with graphene sheets can result with graphene-based films that are very promising for many applications—as strain gauges—where coatings are needed on an industrial scale.<sup>81</sup> Since these

coatings are made out of many overlapping small (100 nm–10  $\mu\text{m}$ ) single-crystal sheets of graphene or multilayer graphene, their response to strain is rather different from the case of continuous films. Understanding the strain mechanisms in these complex nanoscaled systems is crucial for their future applications. In this section, we demonstrate how axial strain of the flexible support affects the electrical properties of LPE graphene films, and similar mechanisms are to be expected for the coatings and films of other 2D materials, fabricated via solution processes.

LPE graphene films were prepared following the route described in Ref. 28. 500  $\mu\text{m}$  mesh high purity and high crystallinity graphite powder was dispersed in N-methylpyrrolidone (15–20 mg/ml), sonicated in a low-power ultrasonic bath for 14 h, and finally centrifuged at 300 rpm. The top part of the resulting solution (with 0.3–0.4 mg/ml graphene concentration) was drop casted on the water surface, and the film formed on a water-air interface was transferred to substrates by the Langmuir–Blodgett technique. Figure 9(a) shows an AFM topography of the film's edge deposited on a  $\text{SiO}_2/\text{Si}$  substrate. The film thickness was estimated from the AFM cross-sections [as presented in Fig. 9(b)], giving  $(4.0 \pm 1.5)$  nm thick films (including also batch-to-batch variations). Typical Raman spectra of the deposited LPE graphene films on a  $\text{SiO}_2/\text{Si}$  substrate are presented in Fig. 9(c), for comparison also showing the spectra obtained from the starting graphite powder (measured within a single graphite flake). Raman spectra were obtained using a TriVista 557S&I GmbH spectrometer ( $\lambda = 532$  nm) under ambient conditions. Intensity ratios of Raman active modes can be used to estimate the quality of the film and to point out the types of defects.<sup>82–85</sup> For the samples used in this study, the  $I(\text{D})/I(\text{G})$  ratio was found to be  $(0.6 \pm 0.1)$ . In particular, the  $I(\text{D})/I(\text{D}')$  ratio of  $(2.8 \pm 0.4)$  was observed, indicating that mainly it is the edges of the flakes that contribute to D mode intensity observed in the spectra.<sup>82</sup>

In order to examine the influence of the uniaxial strain on the electrical conductivity of these LPE graphenes—in the same manner as described above—the films were deposited onto flexible polyethylene terephthalate (PET) foils. Figure 10 gives an example of how LPE graphene films commonly respond to axial strain.

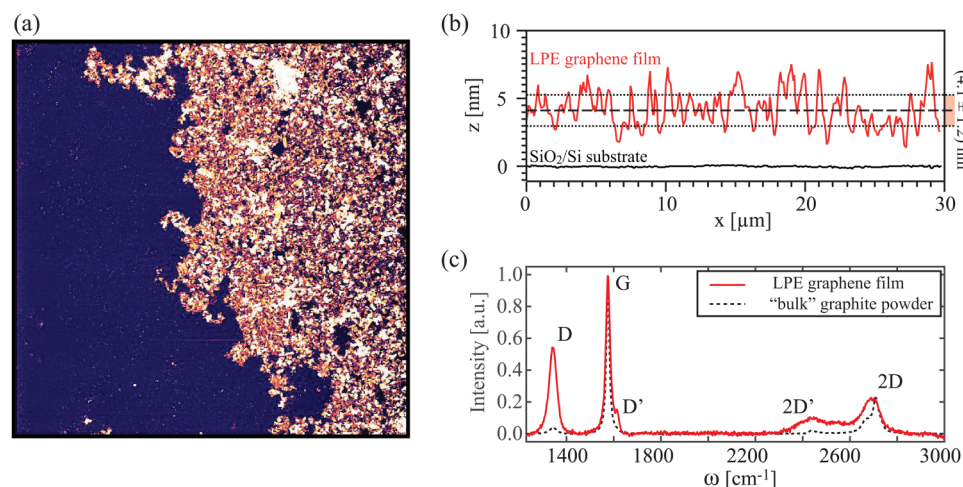


**FIG. 9.**  $50 \times 50 \mu\text{m}^2$  ( $z$  scale 10 nm) of a LPE graphene film edge, deposited on a  $\text{SiO}_2/\text{Si}$  substrate. (b) shows  $30 \mu\text{m}$  long height profiles on the film and on the substrate, averaging  $10 \mu\text{m}$  in width. (c) Raman spectra of the LPE graphene film (solid line) compared with the starting graphite powder (dashed line). Most relevant modes of graphene/graphite are labeled. Spectra are normalized to  $I(\text{G}) = 1$ .

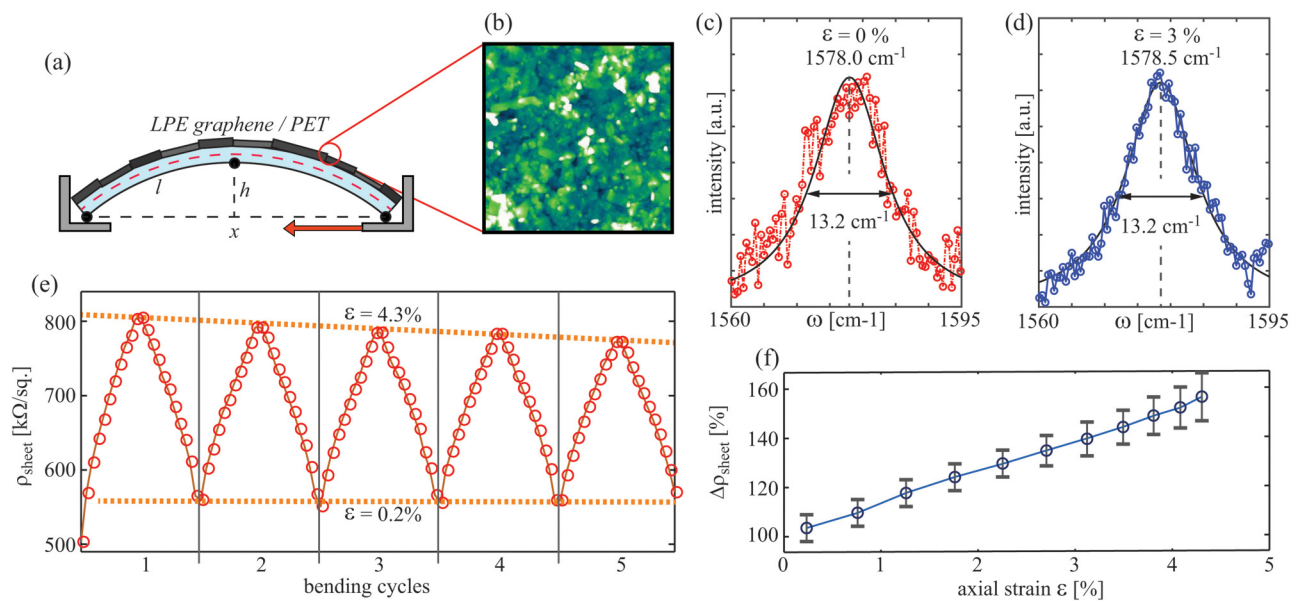


**FIG. 10.** (a) Scheme of the setup used for stretching of LPE graphene films. (b) Typical surface morphology of the films ( $5 \times 5 \mu\text{m}^2$ ,  $z$  scale 40 nm). (c) and (d) Normalized Raman spectra of graphene's G mode without strain, and with 3% of axial strain, respectively. (e) Sheet resistance as a function of alternating axial strain between 0.2% and 4.3%, showing five subsequent bending cycles. (f) Relative sheet resistance (with respect to nominal values) as a function of axial strain, averaged over several LPE films used in this study.

The film was exposed to uniaxial stretching through bending of the PET support, as schematically presented in Fig. 9(a). For this purpose, a micrometer screw was used and controlled by an integrated step motor with the precision down to  $10 \mu\text{m}$ , thus allowing a precise control over the distance between the two fixed points of the PET support. Axial strain that the LPE graphene film exhibits in such a case depends on the bending curvature of the PET support (expressed through geometrical parameters  $x$ ,  $l$ , and  $d$ ) and the thickness of PET ( $200 \pm 20 \mu\text{m}$ ). The structure of the film was investigated using atomic force microscopy [Fig. 9(b)], showing how many small flakes overlap into a continuously conducting film.

A clear fingerprint of stretching the hexagonal lattice of graphene can be obtained from Raman spectroscopy.<sup>82–85</sup> However, in the presented case when many small flakes are deposited onto the PET substrate, the substrate surface stretches but individual flakes are not strained. This can be clearly seen from the lack of both the shift and broadening of graphene's characteristic Raman active mode at  $\sim 1580 \text{ cm}^{-1}$  (G mode).<sup>82–85</sup> By measuring Raman spectra of graphene on PET, while bending the support, effective axial strain was introduced up to  $\sim 3\%$ . Higher values of axial strain during Raman spectroscopy measurements were not possible to reach with a particular setup used in this study. Figures 10(c) and 10(d) show examples of the G mode without and upon 3% of axial strain. The presented spectra have been renormalized, and the spectra of clean PET have been deduced. The G mode was fitted by a single Lorentzian function [solid lines in Figs. 10(c) and 10(d)]. No significant shift (above local variations on the sample) or any

trend of either the mode frequency, intensity, or width was detected within the applied stretching range.

Although individual flakes were not exposed to axial strain in the bending experiments, sheet resistivity of the entire film exhibits a strong dependence on axial strain. Since the main contribution to the total resistance of LPE films comes from the points of overlap between neighboring flakes,<sup>28</sup> stretching the LPE graphene film results in effective pulling apart of individual flakes, and thus an increase in the sheet resistivity of the whole film. Figure 10(e) presents five repeated cycles of stretching and relaxing of the LPE graphene film on PET.

Maximal axial strain applied to the films in the case presented in Fig. 10(e) was estimated to be  $\sim 4.3\%$ . Figure 10(f) shows the dependence of relative sheet resistance increase (with respect to the unstrained value) of the LPE graphene film as a function of axial strain ( $\epsilon$ ). The data were obtained by measuring in a two-point probe configuration by considering several films, with the length of the films varying between 10 mm and 20 mm. The width of the films was fixed to 10 mm. Contact resistance was determined by varying the length of the films and found to be negligible, commonly being over two orders of magnitude smaller than the resistance of LPE graphene films. A strong increase of sheet resistivity was observed upon stretching of the films, increasing linearly by  $\sim 10\%$  for 1% of axial strain. These values are much larger than in the case of CVD graphene,<sup>11</sup> as expected, since the mechanism behind the change in sheet resistance is fundamentally different. Such a large change of resistance upon bending, with the opportunity to further optimize the fabrication, opens up many possibilities

to use LPE graphene films in sensing applications such as strain gauges, pressure sensors, e-skin, and touch screens.<sup>86</sup>

#### IV. CONCLUSION

As we have outlined, strain engineering has an unprecedented ability to manipulate the plethora of properties of low-dimensional materials. Design of new materials with desired features, engineered through the introduction of mechanical deformations, could lead to the production of novel devices and the low-dimensional materials offering a great possibility for manipulation and engineering, especially with techniques that are not available in bulk materials. As demonstrated in this paper, conductivity can be strongly modified with strain. We have shown how electrical conductivity can be tuned with the application of strain in one-dimensional systems. For two-dimensional materials, we demonstrated a significant effect of the biaxial strain on phonons and its drastic modification of superconducting coupling in doped graphene and isostructural MgB<sub>2</sub>-monolayer. We showed that critical temperature of the superconducting state can be enhanced up to several times by the application of strain in order to modify the electron-phonon coupling. All proposed strains are within experimental reach; however, they are beyond the scope of techniques used in this research.

To further understand the effects of strain on realistic 2D materials, we experimentally study an introduction of strain on graphene samples. On two essentially different types of samples, we demonstrate strain effects, both locally and macroscopically. This concerns a possible strain engineering of monolayer graphene by atomic force microscopy and the influence of an axial strain in liquid phase exfoliated graphene films. Manipulation of properties of these different nanomaterials in a controllable fashion through strain engineering has been proven achievable and potentially useful for the design of next generation devices. We showed that AFM produced trenches in graphene could be an excellent platform in order to study local changes in graphene conductivity due to strain. Results of such a study could be related to our theoretical prediction on the effects of strain on conductivity in the 1D-like system. This opens the path for further research on this topic. Application of strain of LPE films has a significant effect on their predicted applications. The sheet resistivity in the entire LPE graphene film exhibits a strong dependence on axial strain. Stretching results in effective pulling apart of individual flakes, and thus an increase in the sheet resistivity of the whole film. This could have a significant impact on their use as flexible electrodes; however, it will open the possibility for a new set of applications such as pressure sensors and strain gauges.

All these results together indicate the effects of the application of strain; tensile and compressive and uniaxial and biaxial strains have significant effects on conductivity and have to be carefully considered depending on the application or concept that we are researching for.

#### ACKNOWLEDGMENTS

DFT calculations were performed using computational resources at Johannes Kepler University, Linz, Austria. This work was supported by the Serbian Ministry of Education, Science and

Technological Development under Project Nos. OI 171005 and III45018. This research was also supported by Qatar National Research Fund, under Grant No. NPRP 7-665-1-125. A.M. acknowledges support from a Lise Meitner fellowship by FWF (Grant No. M2323-N36).

#### REFERENCES

- <sup>1</sup>C. Lee, X. Wei, J. Kysar, and J. Hone, "Measurement of the elastic properties and intrinsic strength of monolayer graphene," *Science* **321**, 385–388 (2008).
- <sup>2</sup>K. S. Novoselov, V. I. Falko, L. Colombo, P. R. Gellert, M. G. Schwab, and K. Kim, *Nature* **490**, 192–200 (2012).
- <sup>3</sup>K. S. Novoselov, A. K. Geim, S. V. Morozov, D. Jiang, Y. Zhang, S. V. Dubonos, I. V. Grigorieva, and A. A. Firsov, "Electric field effect in atomically thin carbon films," *Science* **306**, 666–669 (2004).
- <sup>4</sup>M. I. Katsnelson, "Graphene: Carbon in two dimensions," *Mater. Today* **10**, 1–2 (2007).
- <sup>5</sup>S.-K. Lee, H. Y. Jang, S. Jang, E. Choi, B. H. Hong, J. Lee, S. Park, and J.-H. Ahn, *Nano Lett.* **12**, 3472–3476 (2012).
- <sup>6</sup>R. R. Nair, P. Blake, A. N. Grigorenko, K. S. Novoselov, T. J. Booth, T. Stauber, N. M. R. Peres, and A. K. Geim, *Science* **320**, 1308 (2008).
- <sup>7</sup>S. Bae, H. Kim, Y. Lee, X. Xu, J.-S. Park, Y. Zheng, J. Balakrishnan, T. Lei, H. Ri Kim, Y. I. Song, Y.-J. Kim, K. S. Kim, B. Ozyilmaz, J.-H. Ahn, B. H. Hong, and S. Iijima, *Nat. Nanotechnol.* **5**, 574–578 (2010).
- <sup>8</sup>Z. Sun, D. K. James, and J. M. Tour, *J. Phys. Chem. Lett.* **2**, 2425–2432 (2011).
- <sup>9</sup>K. P. Loh, Q. Bao, P. K. Ang, and J. Yang, *J. Mater. Chem.* **20**, 2277–2289 (2010).
- <sup>10</sup>S. Niyogi, E. Bekyarova, J. Hong, S. Khizroev, C. Berger, W. de Heer, R. C. Haddon, and J. Phys., *Chem. Lett.* **2**, 2487–2498 (2011).
- <sup>11</sup>K. S. Kim, Y. Zhao, H. Jang, S. Y. Lee, J. M. Kim, K. S. Kim, J.-H. Ahn, P. Kim, J.-Y. Choi, and B. H. Hong, *Nature* **457**, 706–810 (2009).
- <sup>12</sup>C.-C. Lu, Y.-C. Lin, C.-H. Yeh, J.-C. Huang, and P.-W. Chiu, *ACS Nano* **6**, 4469–4474 (2012).
- <sup>13</sup>B. J. Kim, H. Jang, S.-K. Lee, B. H. Hong, J.-H. Ahn, and J. H. Cho, *Nano Lett.* **10**, 3464–3466 (2010).
- <sup>14</sup>S.-K. Lee, B. J. Kim, H. Jang, S. C. Yoon, C. Lee, B. H. Hong, J. A. Rogers, J. H. Cho, and J.-H. Ahn, *Nano Lett.* **11**, 4642–4646 (2011).
- <sup>15</sup>P. Avouris, *Nano Lett.* **10**, 4285–4294 (2010).
- <sup>16</sup>F. Bonaccorso, Z. Sun, T. Hasan, and A. C. Ferrari, *Nat. Photonics* **4**, 611–622 (2010).
- <sup>17</sup>Y.-M. Lin, C. Dimitrakopoulos, K. A. Jenkins, D. B. Farmer, H.-Y. Chiu, A. Grill, and P. Avouris, *Science* **327**, 662 (2010).
- <sup>18</sup>F. Schwierz, *Nat. Nanotechnol.* **5**, 487–496 (2010).
- <sup>19</sup>G. G. Naumis, S. Barraza-Lopez, M. Oliva-Leyva, and H. Terrones, "Electronic and optical properties of strained graphene and other strained 2D materials: A review," *Rep. Prog. Phys.* **80**, 096501 (2017).
- <sup>20</sup>C. Si, Z. Suna, and F. Liu, "Strain engineering of graphene: A review," *Nanoscale* **8**, 3207 (2016).
- <sup>21</sup>B. Amorim, A. Cortijo, F. de Juan, A. G. Grushin, F. Guinea, A. Gutiérrez-Rubio, H. Ochoa, V. Parente, R. Roldán, P. San-Jose, J. Schiefele, M. Sturla, and M. A. H. Vozmediano, "Novel effects of strains in graphene and other two dimensional materials," *Phys. Rep.* **617**, 1 (2016).
- <sup>22</sup>M. A. Bissett, M. Tsuji, and H. Ago, "Strain engineering the properties of graphene and other two-dimensional crystals," *Phys. Chem. Chem. Phys.* **16**, 11124 (2014).
- <sup>23</sup>D. Akinwande *et al.*, "A review on mechanics and mechanical properties of 2D materials—Graphene and beyond," *Ext. Mech. Lett.* **13**, 42 (2017).
- <sup>24</sup>G. Profeta, M. Calandra, and F. Mauri, "Phonon-mediated superconductivity in graphene by lithium deposition," *Nat. Phys.* **8**, 131 (2012).
- <sup>25</sup>J. Pesic, "Investigation of superconductivity in graphene and related materials, using ab-initio methods," Ph.D. thesis (University of Belgrade, 2017).

- <sup>26</sup>J. Bekaert, A. Aperis, B. Partoens, P. M. Oppeneer, and M. V. Milosevic, "Evolution of multigap superconductivity in the atomically thin limit: Strain-enhanced three-gap superconductivity in monolayer  $\text{MgB}_2$ ," *Phys. Rev. B* **96**, 094510 (2017).
- <sup>27</sup>Y. Hernandez *et al.*, *Nat. Nanotechnol.* **3**, 563–568 (2008).
- <sup>28</sup>A. Matkovic *et al.*, *2D Mater.* **3**, 015002 (2016).
- <sup>29</sup>J. Hubbard, "Electron correlations in narrow energy bands," *Proc. R. Soc. Lond. A* **276**, 238 (1963).
- <sup>30</sup>V. Celebonovic, "Hubbard model in materials science: Electrical conductivity and reflectivity of models of some 2D materials," in *Advanced 2D Materials*, edited by A. Tiwari and M. Syvajarvi (Scrivener Publishing LLC, 2016), pp. 115–144.
- <sup>31</sup>V. Celebonovic, "The hubbard model: Useful for stretchable nanomaterials?," *J. Phys. Conf. Ser.* **558**, 012006 (2014).
- <sup>32</sup>V. Celebonovic, "Some calculational improvements in applying the hubbard model to nanomaterials," *J. Phys. Conf. Ser.* **794**, 012008 (2017).
- <sup>33</sup>J. van den Brand, M. de Kok, M. Koetse *et al.*, "Flexible and stretchable electronics for wearable health devices," *Solid State Electron.* **113**, 116–120 (2015).
- <sup>34</sup>K. Szalowski, "Critical temperature of  $\text{MgB}_2$  ultrathin superconducting films: BCS model calculations in the tight-binding approximation," *Phys. Rev. B* **74**, 094501 (2006).
- <sup>35</sup>M. Calandra, G. Profeta, and F. Mauri, "Superconductivity in metal-coated graphene," *Phys. Status Solidi B* **12**, 2544 (2012).
- <sup>36</sup>B. M. Ludbrook, G. Levy, P. Nigge, M. Zonno, M. Schneider, D. J. Dvorak, C. N. Veenstra, S. Zhdanovich, D. Wong, P. Dosanjh, C. Strasser, A. Stohr, S. Forti, C. R. Ast, U. Starke, and A. Damascelli, "Evidence for superconductivity in Li-decorated monolayer graphene," *Proc. Natl. Acad. Sci. U.S.A.* **112**(38), 11795–11799 (2015).
- <sup>37</sup>J. Nagamatsu, N. Nakagawa, T. Muranaka, Y. Zentani, and J. Akimitsu, "Superconductivity at 39 K in magnesium diboride," *Nature* **410**, 63–64 (2001).
- <sup>38</sup>J. M. An and W. E. Pickett, "Superconductivity of  $\text{MgB}_2$ : Covalent bonds driven metallic," *Phys. Rev. Lett.* **86**, 4366 (2001).
- <sup>39</sup>Z. H. Ni, T. Yu, Y. H. Lu, Y. Y. Wang, Y. P. Feng, and Z. X. Shen, "Uniaxial strain on graphene: Raman spectroscopy study and band-gap opening," *ACS Nano* **11**, 2301 (2008).
- <sup>40</sup>M. Huang, H. Yan, C. Chen, D. Song, T. F. Heinz, and J. Hone, "Phonon softening and crystallographic orientation of strained graphene studied by Raman spectroscopy," *Proc. Natl. Acad. Sci. U.S.A.* **106**, 7304 (2009).
- <sup>41</sup>V. M. Pereira, A. H. Castro Neto, and N. M. R. Peres, "A tight-binding approach to uniaxial strain in graphene," *Phys. Rev. B* **80**, 045401 (2009).
- <sup>42</sup>F. Ding, H. Ji, Y. Chen, A. Herklotz, K. Dorr, Y. Mei, A. Rastelli, and O. G. Schmidt, "Stretchable graphene: A close look at fundamental parameters through biaxial straining," *Nano Lett.* **10**, 3453 (2010).
- <sup>43</sup>T. M. G. Mohiuddin, A. Lombardo, R. R. Nair, A. Bonetti, G. Savini, R. Jalil, N. Bonini, D. M. Basko, C. Galiotis, N. Marzari, K. S. Novoselov, A. K. Geim, and A. C. Ferrari, "Uniaxial strain in graphene by Raman spectroscopy: G peak splitting, Grüneisen parameters, and sample orientation," *Phys. Rev. B* **79**, 205433 (2009).
- <sup>44</sup>N. Levy, S. A. Burke, K. Meaker, M. L. Panlasigui, A. Zettl, F. Guinea, A. H. C. Neto, and M. F. Crommie, "Strain-induced pseudo-magnetic fields greater than 300 Tesla in graphene nanobubbles," *Science* **329**, 544–547 (2010).
- <sup>45</sup>F. Guinea, M. I. Katsnelson, and A. K. Geim, "Energy gaps and a zero-field quantum Hall effect in graphene by strain engineering," *Nat. Phys.* **6**, 30–33 (2009).
- <sup>46</sup>M. L. Teague, A. P. Lai, J. Velasco, C. R. Hughes, A. D. Beyer, M. W. Bockrath, C. N. Lau, and N.-C. Yeh, "Evidence for strain-induced local conductance modulations in single-layer graphene on  $\text{SiO}_2$ ," *Nano Lett.* **9**, 2542 (2009).
- <sup>47</sup>M. Huang, T. A. Pascal, H. Kim, W. A. Goddard, and J. R. Greer, "Electronic-mechanical coupling in graphene from in situ nanoindentation experiments and multiscale atomistic simulations," *Nano Lett.* **11**, 1241–1246 (2011).
- <sup>48</sup>X.-W. Fu, Z.-M. Liao, J. X. Zhou, Y.-B. Zhou, H.-C. Wu, R. Zhang, G. Jing, J. Xu, X. Wu, W. Guo, and D. Yu, "Strain dependent resistance in chemical vapor deposition grown graphene," *Appl. Phys. Lett.* **99**, 213107 (2011).
- <sup>49</sup>S. Y. Zhou, G. H. Gweon *et al.*, "Substrate-induced band gap opening in epitaxial graphene," *Nat. Mater.* **6**, 770 (2007).
- <sup>50</sup>D. Xiao, W. Yao, and Q. Niu, "Valley-Contrasting physics in graphene: Magnetic moment and topological transport," *Phys. Rev. Lett.* **99**, 236809 (2007).
- <sup>51</sup>G. Gui, J. Li, and J. Zhong, "Band structure engineering of graphene by strain: First-principles calculations," *Phys. Rev. B* **78**, 075435 (2008).
- <sup>52</sup>C. A. Marianetti and H. G. Yevick, "Failure mechanisms of graphene under tension," *Phys. Rev. Lett.* **105**, 245502 (2010).
- <sup>53</sup>P. Giannozzi, A. V. Fedorov, G.-H. Gweon, P. N. First *et al.*, *J. Phys.: Condens. Matter* **21**, 395502 (2009).
- <sup>54</sup>J. Pesic, R. Gajic, K. Hingerl, and M. Belic, "Strain enhanced superconductivity in Li-doped graphene," *Europhys. Lett.* **108**, 67005 (2014).
- <sup>55</sup>J. Pesic, V. Damjanovic, R. Gajic, K. Hingerl, and M. Belic, "Density functional theory study of phonons in graphene doped with Li, Ca and Ba," *Europhys. Lett.* **112**, 67006 (2015).
- <sup>56</sup>C. Si, Z. Liu, W. Duan, and F. Liu, "First-Principles calculations on the effect of doping and biaxial tensile strain on electron-phonon coupling in graphene," *Phys. Rev. Lett.* **111**, 196802 (2013).
- <sup>57</sup>A. Romero-Bermudez and A. M. Garca-Garca, "Size effects in superconducting thin films coupled to a substrate," *Phys. Rev. B* **89**, 064508 (2014).
- <sup>58</sup>A. Bingyun, Z. Zhengjun, T. Tao, and Z. Yiping, "Potential enhancement of superconductivity in  $\text{MgB}_2$  nanosheets: First-principles calculations," *Chem. Phys. Lett.* **591**, 185 (2014).
- <sup>59</sup>C. Zhang, Y. Wang, D. Wang, Y. Zhang, Z.-H. Liu, Q.-R. Feng, and Z.-Z. Gan, "Suppression of superconductivity in epitaxial  $\text{MgB}_2$  ultrathin films," *J. Appl. Phys.* **114**, 023903 (2013).
- <sup>60</sup>N. Acharya, M. A. Wolak, T. Tan, N. Lee, A. C. Lang, M. Taheri, D. Cunnane, B. S. Karasik, and X. X. Xi, " $\text{MgB}_2$  ultrathin films fabricated by hybrid physical chemical vapor deposition and ion milling," *APL Mater.* **4**, 086114 (2016).
- <sup>61</sup>A. Romero-Bermudez and A. M. Garca-Garca, "Shape resonances and shell effects in thin-film multiband superconductors," *Phys. Rev. B* **89**, 024510 (2014).
- <sup>62</sup>D. Valentini, D. van der Marel, and C. Berthod, "Rise and fall of shape resonances in thin films of BCS superconductors," *Phys. Rev. B* **94**, 054516 (2016).
- <sup>63</sup>A. Reserbat-Plantey, D. Kalita, Z. Han, L. Ferlazzo, S. Autier-Laurent, K. Komatsu, C. Li, R. Weil, A. Ralko, L. Marty, S. Guéron, N. Bendiab, H. Bouchiat, and V. Bouchiat, "Strain superlattices and macroscale suspension of graphene induced by corrugated substrates," *Nano Lett.* **14**, 5044–5051 (2014).
- <sup>64</sup>A. J. M. Giesbers, U. Zeitler, S. Neubeck, F. Freitag, K. S. Novoselov, and J. C. Maan, "Nanolithography and manipulation of graphene using an atomic force microscope," *Solid State Commun.* **147**, 366 (2008).
- <sup>65</sup>L. Weng, L. Zhang, Y. P. Chen, and L. P. Rokhinson, "Atomic force microscope local oxidation nanolithography of graphene," *Appl. Phys. Lett.* **93**, 093107 (2008).
- <sup>66</sup>S. Masubuchi, M. Ono, K. Yoshida, K. Hirakawa, and T. Machida, "Fabrication of graphene nanoribbon by local anodic oxidation lithography using atomic force microscope," *Appl. Phys. Lett.* **94**, 082107 (2009).
- <sup>67</sup>P. Nemes-Incze, G. Kukucska, J. Koltai, J. Kürti, C. Hwang, L. Tapasztó, and L. P. Biró, "Preparing local strain patterns in graphene by atomic force microscope based indentation," *Sci. Rep.* **7**, 3035 (2017).
- <sup>68</sup>B. Vasić, M. Kratzer, A. Matković, A. Nevsad, U. Ralević, D. Jovanović, C. Ganser, C. Teichert, and R. Gajić, "Atomic force microscopy based manipulation of graphene using dynamic plowing lithography," *Nanotechnology* **24**, 015303 (2013).
- <sup>69</sup>A. C. Ferrari *et al.*, *Nanoscale* **7**, 4598–4810 (2014).
- <sup>70</sup>F. Bonaccorso, L. Colombo, G. Yu, M. Stoller, V. Tozzini, A. C. Ferrari, R. S. Ruoff, and V. Pellegrini, *Science* **347**, 1246501 (2015).
- <sup>71</sup>J. Coraux, A. T. N'Diaye, C. Busse, and T. Michely, *Nano Lett.* **8**, 565–570 (2008).
- <sup>72</sup>A. Reina, X. Jia, J. Ho, D. Nezich, H. Son, V. Bulovic, M. S. Dresselhaus, and J. Kong, *Nano Lett.* **9**, 30–35 (2008).
- <sup>73</sup>X. Li *et al.*, *Science* **324**, 1312–1314 (2009).
- <sup>74</sup>A. V. Zaretski and D. J. Lipomi, *Nanoscale* **7**, 9963–9969 (2015).

- <sup>75</sup>M. Kratzer *et al.*, *Appl. Phys. Lett.* **106**, 103101 (2015).
- <sup>76</sup>P. Blake *et al.*, *Nano Lett.* **8**, 1704–1708 (2008).
- <sup>77</sup>S. Stankovich, D. A. Dikin, G. H. Dommett, K. M. Kohlhaas, E. J. Zimney, E. A. Stach, R. D. Piner, S. T. Nguyen, and R. S. Ruoff, *Nature* **442**, 282–286 (2006).
- <sup>78</sup>S. Stankovich, D. A. Dikin, R. D. Piner, K. A. Kohlhaas, A. Kleinhammes, Y. Jia, Y. Wu, S. T. Nguyen, and R. S. Ruoff, *Carbon* **45**, 1558–1565 (2007).
- <sup>79</sup>G. Eda, G. Fanchini, and M. Chhowalla, *Nat. Nanotechnol.* **3**, 270–274 (2008).
- <sup>80</sup>M. Cai, D. Thorpe, D. H. Adamson, and H. C. Schniepp, *J. Mater. Chem.* **22**, 24992–25002 (2012).
- <sup>81</sup>M. Segal, *Nat. Nanotechnol.* **4**, 612–614 (2009).
- <sup>82</sup>A. Eckmann, A. Felten, A. Mishchenko, L. Britnell, R. Krupke, K. S. Novoselov, C. Casiraghi, “Probing the nature of defects in graphene by Raman spectroscopy,” *Nano Lett.* **12**, 3925–3930 (2012).
- <sup>83</sup>A. C. Ferrari and D. M. Basko, *Nature Nanotech.* **8**, 235 (2013).
- <sup>84</sup>T. Mohiuddin, A. Lombardo, R. R. Nair *et al.*, *Phys. Rev. B* **79**, 205433 (2009).
- <sup>85</sup>F. Ding, H. Ji, Y. Chen, A. Herklotz, K. Dorr, Y. Mei, A. Rastelli, and O. G. Schmidt, *Nano Lett.* **10**, 3453–3458 (2010).
- <sup>86</sup>Y. Zang, F. Zhang, C.-a. Di, and D. Zhu, *Mater. Horiz.* **2**, 140–156 (2015).
- <sup>87</sup>M. Huang, T. A. Pascal, H. Kim, W. A. Goddard, and J. R. Greer, *Nano Lett.* **11**, 1241–1246 (2011).
- <sup>88</sup>M. L. Teague, A. P. Lai, J. Velasco, C. R. Hughes, A. D. Beyer, M. W. Bockrath, C. N. Lau, and N. C. Yeh, *Nano Lett.* **9**, 2542–2546 (2009).

# Hubbard Model in Material Science: Electrical Conductivity and Reflectivity of Models of Some 2D Materials

Vladan Celebonovic

*Institute of Physics, University of Belgrade, Belgrade, Serbia*

---

## **Abstract**

The aim of this chapter is to present a self-contained introduction to the Hubbard model (HM) and results of its applications in modeling some materials. The chapter has four sections. The first part is devoted to the basics of the HM. The Hamiltonian of the model is introduced, and its structure and limits are explained. The method used for the calculation of the conductivity is introduced. The second part contains results concerning the calculation of the electrical conductivity. Expressions for the electrical conductivity of 1D systems previously derived by the author will be extended. The possibility of broadening the applicability of these results to 2D materials will be tested for rectangular 2D lattices. Starting from standard optics and the expressions for the conductivity, it becomes possible to calculate the reflectivity. Within the HM, it is dependent on various experimentally measurable parameters, and for some values of these parameters, it approaches zero. Physical implications of the reflectivity of a 2D material approaching zero will be discussed. At the end, some ideas for future work are briefly mentioned.

**Keywords:** Modeling materials, Hubbard model, memory function method, electrical conductivity, reflectivity

## **4.1 Introduction**

The fact that some materials are metals and some are not is known to mankind for thousands of years. A logical consequence of this fact was

---

*Corresponding author:* vladan@ipb.ac.rs

---

Ashutosh Tiwari and Mikael Syväjärvi (eds.) *Advanced 2D Materials*, (115–144) © 2016 Scrivener Publishing LLC



to hypothesize that there must exist “some way” in which insulators and metals can somehow undergo mutual transformations. At the end of the nineteenth century, in 1897, the electron was discovered [1]. It was thought at the time that metals contained electrons, which were free to move and conduct electricity, while in insulators the electrons were “motionless” for some reason.

A partially correct explanation was obtained in the early days of quantum mechanics, when the Schrödinger equation was applied to a periodic structure, and the existence of zones of allowed energies was discovered. It then emerged that if the first zone is completely filled and the second one is empty, the system will be insulating. For an account of early work on the metal to insulator transition ( $M \rightarrow I$  transition for short), see, for example, [2]. A modern account is available in [3].

However, the first general model of the  $M \rightarrow I$  transition is due to John Hubbard [4]. The ideas that he started developing in [4] form the basis of what is now called the Hubbard model (HM). Although it was proposed a little more than 50 years ago, the HM is still very attractive with a broad range of applications [5]. This is well illustrated by the number of papers using it in work on various problems. Just as an example, a search at the time of this writing (end of October 2015) at <http://prola.aps.org/> with the keywords “Hubbard model” gave 260 titles of papers containing these words published in American Physics Society journals within the last year. A search at <http://www.google.com> gave a huge number of approximately 16 million hits with the same keywords.

The aim of this chapter is to present a self-contained introduction to the HM. With such a huge literature on the subject existing and readily accessible, it would be impossibly ambitious to cover all aspects of the model in a relatively limited number of pages. Therefore, this chapter will present the basics of the model and its limits, the method for the calculation of the electrical conductivity and reflectivity starting from the Hamiltonian, and the applicability of these calculations to modelization of 2D materials.

## 4.2 The Hubbard Model

### 4.2.1 The Hubbard Model in 1D

Qualitatively speaking, the HM is seemingly very simple. It takes into account some well-known facts: that a solid has a lattice structure; that electrons can circulate within the lattice; and that in each node of the

lattice, there are two electrons with opposing spins, which mutually interact. According to basic principles of statistical physics, the behavior of any physical system is specified by its Hamiltonian. The Hamiltonian of the HM has a seemingly very simple form:

$$H = H_0 + H_I \quad (4.1)$$

The first term denoted by  $H_0$  is called the “kinetic energy term”, while  $H_I$  is the interaction term. Complications start to appear when attempting to write this Hamiltonian explicitly, and even more if one tries to solve the HM for spatial dimensionality of the system greater than one. When interest in correlated electron systems arose, near the middle of the last century, the prevailing opinion was that 2D materials were thermodynamically unstable and accordingly could not exist. This was the result of work of some of the greatest theoretical physicists of the time like Landau and Peirels (quoted in [6]).

Their work was somewhat later extended by Mermin [7], and the results were taken for granted for decades. Then, to the amazement of the condensed matter community, graphene was discovered as a 2D allotrope of carbon in 2004. During the time elapsed since the discovery of graphene, the situation has so completely changed that now the science and technology roadmap for graphene is a publication of more than 200 pages [8].

In one spatial dimension (1D for short), and within the formalism of second quantization, the Hamiltonian of the HM has the following form:

$$H = -t \sum_{i=1, \sigma}^N \left( c_{i+1, \sigma}^+ c_{i, \sigma} + c_{i, \sigma}^+ c_{i+1, \sigma} \right) + U \sum_l n_{l, \uparrow} n_{l, \downarrow} \quad (4.2)$$

The symbols  $N$ ,  $t$ , and  $U$  denote, respectively, the number of nodes of a lattice, the mean kinetic energy of the electrons (also called the hopping energy), and the interaction energy of two electrons with opposing spins on the same node of the lattice, and  $\sigma$  is the electron spin. The symbols in parenthesis denote the creation and annihilation operators. Apart from  $t$  and  $U$ , the third important parameter of the HM is the band filling  $n$ . The band filling is defined as the ratio of the number of electrons in the band and the number of lattice sites. For example, the symbol  $c_{i, \sigma}$  denotes the operator that creates an electron of spin  $\sigma$  at lattice site  $i$ .

The obvious question is can Eq. (4.1) be solved, and what physical knowledge can be gained from it. From the purely physical point of view,  $t$  and  $U$  can have arbitrary values. However, there exist two limiting cases in which solving Eq. (4.1) is not very complicated; these are the so-called *atomic* and *band* limits.

The *atomic* limit corresponds to the  $t = 0$ ,  $U \neq 0$  case. This means that electrons do not move, which further implies that there is no transport of electricity. In practical terms, the atomic limit of the HM is not interesting from the point of view of the transport properties, and therefore will not be discussed.

The *band* limit corresponds to  $U = 0$ ,  $t \neq 0$ ; that is, electrons move through the lattice, but there is no interaction of electrons on a given lattice node. The system in this case has some finite electrical conductivity. The Hamiltonian contains only the kinetic term:

$$H = -t \sum_l \left( c_{i+1,\sigma}^+ c_{i,\sigma} + c_{i,\sigma}^+ c_{i+1,\sigma} \right) \quad (4.3)$$

Fourier transforming the operators in Eq. (4.3) by relations of the form

$$c_{i,\sigma}^+ = \frac{1}{\sqrt{N}} \sum_{k_1} e^{ik_1 s} c_{k_1,\sigma}^+ \quad (4.4)$$

where  $s$  is the lattice constant, after some algebra, one gets that the electron energy is given by

$$\varepsilon(k) = -2t \cos ks \quad (4.5)$$

Solving the Hamiltonian of the HM in a general case, would mean finding the ground-state energy, wave function, and chemical potential for arbitrary values of  $U$  and  $t$ .

The limits discussed above could be called “the extremes”. In any real material, both  $t$  and  $U$  will have non-zero values, and the obvious question is how does one solve the HM in such a case.

A general solution of the HM in 1D was published in [9], where the ground-state energy, wave function, and the chemical potential were obtained. The system considered in [9] is a short-range one-band model, in which electrons hop between the sites and interact with a repulsive interaction energy when they the same lattice site. Two problems were especially interesting: the existence (or non-existence) of a Mott transition between the conducting and insulating states, with the increase in the strength of the interaction, and the magnetic nature of the ground state.

The crystal studied in [9] contains  $N_a$  lattice sites and  $N$  electrons. The dimensionality of the system is arbitrary at the beginning of the paper, and the Hamiltonian is given by Eq. (4.2). Paper [9] is too short, and the calculations in it are too complex to reproduce them here. Assuming that an equal number of spins point in the up and down direction, one gets that the ground-state energy of the system considered is given by

$$E = -4N_a \int_0^{\infty} \frac{J_0(\omega)J_1(\omega)d\omega}{\omega \left[ 1 + \exp\left(\frac{1}{2}\omega U\right) \right]} \quad (4.6)$$

where  $J_0$  and  $J_1$  are Bessel functions and  $U$  is the interaction energy of two electrons with opposite spins on the same lattice node.

The electrical transport properties are investigated in [9] by calculating the chemical potentials, which are there defined as

$$\begin{aligned} \mu_+ &= E(M+1, M; U) - E(M, M; U) \\ \mu_- &= E(M, M; U) - E(M-1, M; U) \end{aligned} \quad (4.7)$$

where  $M$  denotes the number of spin-down electrons. If these two chemical potentials are equal, the system is a conductor. If  $\mu_+ > \mu_-$ , the system is an insulator [9]. It has been shown in [9] that in the case of a half-filled band the ground state is insulating for any nonzero  $U$  and conducting for  $U = 0$ . The chemical potential tends to zero for vanishing values of  $U$ . This implies that there is no Mott transition for nonzero  $U$ . The paper of Lieb and Wu is short but mathematically difficult. Due to limited space, many details were not explained in sufficient detail. The authors realized it and some time ago prepared a sequel [10].

#### 4.2.2 The Hubbard Model in 2D

What about the HM in 2D? As can be expected, the situation is more complex than in the 1D case. The Hamiltonian of the 2D HM is clearly more complicated.

It has the following form

$$H = -\sum_{i,j} \sum_{\sigma} t_{ij} c_{i\sigma}^+ c_{j\sigma} + \frac{1}{2} \sum_{i,j,k,l} \sum_{\sigma,\sigma'} \langle ij|v|kl \rangle c_{i,\sigma}^+ c_{j,\sigma}^+ c_{l,\sigma} c_{k,\sigma'} \quad (4.8)$$

Lattice sites are denoted by Latin indices,  $\sigma$  is the spin index, symbols of the form  $c_{i,\sigma}^+$  denote second quantization operators creating an electron with spin  $\sigma$  at a lattice site  $i$ . The hopping energy is denoted by  $t_{ij}$ , and  $v$  is the coulomb interaction.

In the case of the HM in 2D, solutions “in the spirit” of [9] do not exist, so work has to be performed numerically. The best-known method for such studies is the so-called density matrix renormalization group (DMRG). In short, DMRG is a numerical method designed to give the low-energy

physics of quantum many body systems. It was invented by S.R. White [11, 12] and has continued to develop ever since.

A serious problem encountered in quantum many-body systems is the fact that the size of the Hilbert space in any given problem grows with the number of degrees of freedom of the system. Just as an example, a chain of length  $L$  of particles of spin  $1/2$  in 1D has  $2^L$  degrees of freedom, which can easily become an impressive number. DMRG is a numerical method devised with the idea of reducing the number of degrees of freedom of the system to those, which are most important for the ground state of the system.

The method divides the system under consideration in two blocks, which can be of unequal sizes and two sites in between the blocks. A set of representative states is chosen for each block at the start of the procedure. The two blocks and the two sites between them form a “superblock”. Using the representative states of the blocks, the ground state of the superblock can be found. A certain number of iterations will be needed in order to obtain precise results.

The ground state of the superblock is then projected on the subspaces for each block, and they are accordingly improved. The calculation advances in “sweeps”. In the calculations, the size of the blocks increases. A sweep is the number of steps needed for the blocks to become of equal sizes.

Since the appearance of the two founding papers by White, DMRG has hugely developed. There exist many excellent reviews, examples of which are [13–15]. Reference [15] is especially interesting, as it is devoted to the use of DMRG in modeling 2D materials. The software needed for the calculations is open source and can be freely downloaded. One of the web sites is <http://alps.comp-phys.org/>. Another excellent source of information on DMRG is at the University of Hannover: <http://www.itp.uni-hannover.de/~jeckelm/dmrg/>.

The present author has done a certain amount of work in studies of the HM in 1D. The electrical conductivity of the HM in 1D was calculated and applied to modeling of 1D materials. Attempts of extending the applicability of these results to certain types of 2D lattices were also made. Broadly speaking, the remainder of this chapter is devoted to a review and possible extensions of these results.

The starting question in such work is the choice of the method of calculation of the conductivity. Two possibilities were obvious: the formalism developed by Kubo [16] and the memory function method (MFM) [17].

Paper [16] was prepared with the aim of developing a theory of the calculation of transport coefficients, and, in general terms, admittance of the system when it is exposed to external forces. It ranks among the best-known papers of modern statistical physics.

The proclaimed aim of the paper has been fulfilled by setting up a kinetic equation for the particle distribution function, and then solving it. Such an approach is in line with the general principles of statistical physics. Pursuing this reasoning, details of which can be found in [16], one gets the following expression for the components of the conductivity tensor:

$$\sigma_{\mu\nu} = \int_0^\infty \int_0^\beta d\lambda \langle J_\nu(-i\hbar\lambda) J_\mu(t) \rangle \quad (4.9)$$

which can also be expressed as

$$\sigma_{\mu\nu} = \lim_{s \rightarrow 0^+} \frac{1}{s} \left[ \varphi_{\mu\nu}(0) + \int_0^\infty \varphi_{\mu\nu}(t) e^{-st} dt \right] \quad (4.10)$$

where

$$\varphi_{\mu\nu}(t) = -\frac{1}{i\hbar} \text{Tr} \rho [J_\nu, J_\mu(t)] \quad (4.11)$$

and

$$J_\mu = \sum_i e_i x_{i\mu} \quad (4.12)$$

is the total electrical current.

From the purely theoretical point of view, these equations give the result for the electrical conductivity. However, they are inapplicable to any practical calculation pertaining to any real material. The reason is purely mathematical. In order to calculate the commutators in Eq. (4.11), one needs the expression for the total current, which in turn requires the knowledge of the speeds of the conducting particles, and these are in practice not known. Therefore, although the Kubo formulae are an important result in statistical mechanics, they are not practically applicable and will not be used in this chapter.

The calculations that are discussed in the following have been performed using the so-called MFM. The MFM is a result of the continuation of the work of Kubo published by several authors. Broadly speaking, the aim of the MFM is to express the response functions in terms of a holomorphic memory function [17, 18]. A practical application of this development, in view of calculations in material science, is available in [19].

The main equations for the calculation of the electrical conductivity within the MFM are

$$\chi_{AB} = \langle\langle A; B \rangle\rangle = -i \int_0^{\infty} e^{izt} \langle\langle [A(t), B(0)] \rangle\rangle dt \quad (4.13)$$

and

$$\sigma(\omega) = i \frac{\omega_p^2}{4\pi z} \times \left[ 1 - \frac{\chi(z)}{\chi(0)} \right] \quad (4.14)$$

In these two equations,  $\omega_p^2 = 4\pi n_e e^2 / m_e$  is the square of the plasma frequency; the symbols  $n_e$ ,  $e$ , and  $m_e$  denote the electron number density, charge, and mass, respectively;  $\chi_0 = n_e / m_e$  is the zero frequency limit of the dynamical susceptibility.

Equation (4.13) is a general definition of the linear response of a physical quantity corresponding to operator  $A$ , to the perturbation by another physical quantity described by operator  $B$ . The susceptibility is an analytic function for all non-real frequencies  $z$  [19]. The Heisenberg representation of the operator  $A$  is denoted by  $A(t)$ . The explicit definition of the current-current correlation function can be obtained by inserting into Eq. (4.13)  $A = B = [j, H]$  with  $j$  denoting the current operator and  $H$  the Hamiltonian.

In early work such as [20], some objections were voiced against the MFM, on the grounds that it does not reproduce some standard results for the conductivity. However, according to more recent works such as [21], the MFM is described as a “tool of choice” for the calculation of the conductivity.

Before embarking on the calculation of the conductivity, two problems have to be solved: the “choice” of the theoretical model, which is to be applied for the electron gas, and the calculation of the chemical potential of the electron gas.

For the past 60 years, normal metals are theoretically described by the Landau Fermi liquid theory (FLT). It is known that the FLT fails in 1D systems. The reason for this is the fact that some vertices, which the FLT assumes to be finite, diverge in 1D because of the Peierls effect [22]. Until the past two decades of the preceding century, the question “FLT” or “a replacement” in 1D systems was mainly of academic nature, as experiments on low-dimensional systems were in their “infancy”. Such experiments became possible when 1D or Q1D materials, such as the organic conductors were synthesized. As a consequence, the question of the choice of a theoretical model to be used in such studies regained importance.

Pure theory indicates that the Luttinger liquid model should be used ([23] and references given there). Later, development of the field showed

that there are studies in which application of the FLT gives results in agreement with experiments [24–27]. Accordingly, the FLM will be used in the calculations, which will be discussed in the remainder of this chapter.

Before embarking on a detailed discussion of the electrical conductivity within the HM and its use in modeling 2D materials, it is appropriate to link the conductivity with the reflectivity of the HM. This link is important for experiments—the reflectivity can be measured and/or used to estimate values of various parameters of a material by comparing calculated values of the reflectivity with experimental data.

The propagation of an electromagnetic wave through a non-magnetic material is determined by the dielectric function  $\varepsilon(\omega)$  and the refractive index  $N(\omega)$ , where  $N(\omega) = \sqrt{\varepsilon(\omega)}$  [29]. Both of these functions are complex quantities, which means

$$\varepsilon(\omega) = \varepsilon_R(\omega) + i\varepsilon_I(\omega) \quad (4.15)$$

$$N(\omega) = n(\omega) + iK(\omega) \quad (4.16)$$

where the symbol  $K(\omega)$  denotes the extinction coefficient. Reflectivity is defined as the ratio [28]

$$R(\omega) = \frac{(n-1)^2 + K^2}{(n+1)^2 + K^2} \quad (4.17)$$

It can be shown [28] that

$$\varepsilon_R(\omega) = n^2 - K^2 \text{ and } \varepsilon_I(\omega) = 2nK \quad (4.18)$$

and also

$$\varepsilon = 1 + i \frac{4\pi\sigma}{\omega} \quad (4.19)$$

Inserting Eq. (4.15) into Eq. (4.18), it follows that

$$n = \frac{2\pi\sigma_R}{K\omega} \quad (4.20)$$

As  $\varepsilon_R(\omega) = 1 - \frac{4\pi\sigma_I}{\omega}$ , some algebra leads to

$$\left( \frac{2\pi\sigma_R}{\omega} \right)^2 \frac{1}{K^2} - K^2 = 1 - \frac{4\pi\sigma_I}{\omega} \quad (4.21)$$



or

$$K^4 + K^2 \left(1 - \frac{4\pi\sigma_I}{\omega}\right) - \left(\frac{2\pi\sigma_R}{\omega}\right)^2 = 0 \quad (4.22)$$

Equation (4.22) can be solved to give

$$K_{1,2}^2 = \frac{4\pi\sigma_I\omega - \omega^2 \pm \left[ (4\pi\sigma_R\omega)^2 + (\omega^2 - 4\pi\sigma_I\omega)^2 \right]^{1/2}}{2\omega^2} \quad (4.23)$$

Inserting Eq. (4.20) into Eq. (4.17) leads to the following expression for the reflectivity

$$R = \frac{(2\pi\sigma_R)^2 - K\omega \left[ 4\pi\sigma_R - K\omega(1 + K^2) \right]}{(2\pi\sigma_R)^2 + K\omega \left[ 4\pi\sigma_R + K\omega(1 + K^2) \right]} \quad (4.24)$$

### 4.3 Calculations of Conductivity

This section is devoted to a detailed account of the electrical conductivity of 1D and 2D rectangular lattices within the HM. The account of the calculation of the conductivity will rely on previous work of the author, but which will be somewhat extended here.

Calculating the conductivity within the MFM demands the knowledge of the susceptibility and that, according to Eq. (4.13), requires the knowledge of the commutator  $[j, H]$  where  $j$  is the current operator. For a system with the Hamiltonian given by the HM in 1D (Eq. 4.2), the current operator has the form

$$j = -iw \sum_{l,\sigma} \left( c_{l,\sigma}^+ c_{l+1,\sigma} - c_{l+1,\sigma}^+ c_{l,\sigma} \right) \quad (4.25)$$

The calculation of the commutator starts by a decomposition:

$$[j, H] = [j, H_0 + H_I] = [j, H_0] + [j, H_I] \quad (4.26)$$

and then proceeds as follows

$$[j, H_0] = \left[ -iw \sum_{l,\sigma} \left( c_{l,\sigma}^+ c_{l+1,\sigma} - c_{l+1,\sigma}^+ c_{l,\sigma} \right), -w \sum_{l,\sigma} \left( c_{l,\sigma}^+ c_{l+1,\sigma} + c_{l+1,\sigma}^+ c_{l,\sigma} \right) \right] \quad (4.27)$$

Using the fermionic commutation relations the last expression can be transformed into

$$[j, H_0] = 2iw^2 \sum_{l,\sigma} (n_{l,\sigma} - n_{l+1,\sigma}) = 0 \quad (4.28)$$

The calculation of  $[j, H_I]$  proceeds in a similar way, although it is a little more complex

$$[j, H_I] = \left[ -iw \sum_{l,\sigma} (c_{l,\sigma}^+ c_{l+1,\sigma} - c_{l+1,\sigma}^+ c_{l,\sigma}), U \sum_j n_{j,\uparrow} n_{j,\downarrow} \right] \quad (4.29)$$

which can be transformed into

$$[j, H_I] = \left[ -iwU \sum_{l,j,\sigma} [c_{l,\sigma}^+ c_{l+1,\sigma} - c_{l+1,\sigma}^+ c_{l,\sigma}] n_{j,\uparrow} n_{j,\downarrow} \right] \quad (4.30)$$

Using the fact that within the second quantization formalism  $n_l = c_l^+ c_l$  and the fermionic commutation rules, it can be shown that

$$A = [j, H] = [j, H_I] = -iwU \sum_{l,\sigma} (c_{l,\sigma}^+ c_{l+1,\sigma} + c_{l+1,\sigma}^+ c_{l,\sigma}) (\delta_{l+1,j} - \delta_{l,j}) n_{j,-\sigma} \quad (4.31)$$

where  $\delta$  is the Kronecker delta.

Eq. (4.31) can be Fourier transformed by four relations of the form

$$c_{l,\sigma}^+ = \frac{1}{\sqrt{N}} \sum_{k_1} e^{ik_1 l s} c_{k_1,\sigma}^+ \quad \text{and} \quad c_{l,\sigma} = \frac{1}{\sqrt{N}} \sum_{k_1} e^{-ik_1 l s} c_{k_1,\sigma} \quad (4.32)$$

which leads to

$$A(k) = -\frac{iwU}{N^2} \sum_{\{k\}, l, \sigma} e^{i(k_1 - k_2) l s} (e^{ik_1 s} + e^{-ik_2 s}) (e^{i(k_3 - k_4) s} - 1) e^{i(k_3 - k_4) l s} c_{k_1,\sigma}^+ c_{k_2,\sigma} c_{k_3,-\sigma}^+ c_{k_4,-\sigma} \quad (4.33)$$

Note that in Eqs. (4.25–4.33), the hopping has been denoted by  $w$  in order to avoid confusion with the time. The time evolution is introduced by

$$c_k^+(t) = e^{i\epsilon(k)t} c_k^+ \quad \text{and} \quad c_k(t) = e^{-i\epsilon(k)t} c_k \quad (4.34)$$

Inserting these two transformations into Eq. (4.33), one can get the expression for  $A(t)$ . Using that result and the expression for  $A(k)$  one can

finally get the expression for the dynamical susceptibility. The calculation is long and demands a meticulous approach, and the final result for the current–current correlation function is

$$\langle [A(t), A] \rangle = 4 \left( -\frac{iwU}{N^2} \right)^2 \sum_{\{k\}} (1)(2)(3)(4) (n_{k_4} n_{k_2} - n_{k_1} n_{k_3}) \quad (4.35)$$

and

$$(1)(2)(3)(4) = (e^{ik_5s} + e^{-ik_6s})(e^{i(k_7-k_8)s} - 1)(e^{ik_1s} + e^{-ik_2s})(e^{i(k_3-k_4)s} - 1)e^{it(\varepsilon_5 - \varepsilon_6 + \varepsilon_7 - \varepsilon_8)} \quad (4.36)$$

The symbols in Eq. (4.36) of the form  $\varepsilon_n$  where  $n$  is an integer denote the combination  $\varepsilon_{k_n}$ .

Inserting Eqs. (4.35) and (4.36) into Eq. (4.13), performing the integrations, gives the following final expression for the dynamical susceptibility  $\chi$  of a 1D HM. Note that the frequency, denoted by  $z$ , is here considered to be a complex quantity, which means that  $z = z_1 + iz_2$ . Details of the calculation are available in [24].

$$\chi(z) = 32i \left( -i \frac{wU}{N} \right)^2 \sum_k (n_{k_4} n_{k_2} - n_{k_1} n_{k_3}) \times \sin^2 \left[ \frac{k_2 - k_1}{2} s \right] \times [\cos(k_1 + k_3)s + \cos(k_2 - k_3)s] \times W \quad (4.37)$$

where

$$W = \frac{z_2 + i(z_1 + a + b)}{z_2^2 + i(z_1 + a + b)^2} \quad (4.38)$$

and

$$\alpha = 2w (\cos k_3s - \cos k_4s); b = 2w (\cos k_1s - \cos k_2s) \quad (4.39)$$

Expressing the frequency as a complex quantity  $z = z_1 + iz_2$  and  $z_2 = \alpha z_1$  into Eq. (4.14) and then separating the real and imaginary parts, leads to the following results for the real and imaginary parts of the electrical conductivity

$$\sigma_R = \frac{\omega_p^2}{4\pi z_1 (1 + \alpha^2)} \left[ a \left( 1 - \frac{\chi_R}{\chi_0} \right) + \frac{\chi_I}{\chi_0} \right] \quad (4.40)$$

$$\sigma_I = \frac{\omega_p^2}{4\pi z_1 (1 + \alpha^2)} \left[ 1 - \frac{\chi_R + \alpha \chi_I}{\chi_0} \right] \quad (4.41)$$

Both of these expressions become considerably simplified when  $\alpha = 0$ , that is when the frequency is a real function. Once the real part of the susceptibility is determined by the summation by Eqs. (4.37–4.39), the imaginary part can be calculated as [28]

$$\chi_I(\omega_0) = -2 \frac{\omega_0}{\pi} P \int_0^{\infty} \frac{\chi_R(\omega)}{\omega^2 - \omega_0^2} d\omega \quad (4.42)$$

where  $P$  denotes the principal value of the integral. Details of the calculation are available in [24]. The resulting expression for the electrical conductivity of a 1D HM is

$$\sigma_R(\omega_0) = \left( \frac{1}{2\chi_0} \right) \left( \frac{\omega_p^2}{\pi} \right) \frac{1}{\omega_0^2 - (bt)^2} \left( \frac{Ut}{N^2} \right)^2 \times S \quad (4.43)$$

and

$$S = \frac{42.49916}{(1 + e^{\beta(-\mu-2t)})^2} + \frac{78.2557}{(1 + e^{\beta(-\mu+2t)\cos(1+\pi)})^2} + \frac{bt}{\omega_0 + bt} \left[ \frac{4.53316}{(1 + e^{\beta(-\mu-2t)})^2} + \frac{24.6448}{(1 + e^{\beta(-\mu+2t)\cos(1+\pi)})^2} \right] \quad (4.44)$$

The symbol  $\mu$  denotes the chemical potential of the electron gas on a 1D lattice, which is given by [29]

$$\mu = \frac{(\beta t)^6 (ns - 1) |t|}{1.1029 + 0.1694(\beta t)^2 + 0.0654(\beta t)^4} \quad (4.45)$$

The symbols  $n$ ,  $s$ ,  $t$ , and  $\beta$  denote, respectively, the band filling, the lattice constant, the hopping, and the inverse temperature.

When performing the summation in Eqs. (4.37–4.39), one gets a result with more than 2000 terms [24]. This is obviously impractical, so the expression for the real part of the conductivity was derived by using various approximations; basically, the sum was limited to the first 32 terms, and this was further analyzed. The obvious question is whether increasing the number of terms being taken into account in the sums would be of practical importance when trying to model 1D and 2D materials.

As a test, while writing this contribution, the first 40 terms in the summation in Eqs. (4.37–4.39) were analyzed. The result is mathematically interesting but not very practical. Namely, the expression obtained in that case for the real part of the susceptibility was obviously more complex than when analyzing only 32 terms. This increased complexity diminished their

practical applicability in modelization of materials. In the remainder of this chapter, Eqs. (4.43–4.45) will be used.

Expressions (4.43–4.45), as they are, can be applied to 1D materials. However, a simple calculation opens up the possibility of applying them to 2D rectangular lattices. Take as an example a 2D rectangular lattice of side length  $\alpha$  and denote the lattice sides by  $x$  and  $y$ . In that case, the current flowing through the system is obviously given by

$$\vec{j} = j_x \vec{e}_x + j_y \vec{e}_y \quad (4.46)$$

where  $\vec{e}_x, \vec{e}_y$  are the unitary vectors of the lattice axes. The total current is given by

$$j = [j_x^2 + j_y^2]^{1/2} \quad (4.47)$$

By definition  $\vec{j} = \sigma \vec{E}$  where  $\sigma$  is the electrical conductivity and  $E$  is the electrical field. Assuming that the electrical fields along the two lattice axes are equal, one finally gets that the electrical conductivity of a 2D rectangular lattice is given by the expression:

$$\sigma = [\sigma_x^2 + \sigma_y^2]^{1/2} \quad (4.48)$$

Two-dimensional materials can be modeled in two ways by using this expression:

- One possibility is to carefully chose values of various parameters, which enter the expression for the conductivity of a 1D HM, and thus try to reproduce the experimental data;
- The other possibility treats the problem in the opposite way. One takes the experimental data and attempts to derive values of parameters of the HM which, when inserted into the expression for the conductivity fit as closely as possible the measured data.

An expected step in modeling a 2D material would be to use expressions derived earlier in this section for the electrical conductivity of a 1D HM, and then insert them into Eq. (4.48). As a first step, modelization can start by inserting Eq. (4.44) into Eq. (4.43), expanding and taking the first term. In this way, one gets the following approximation

$$\sigma \cong \frac{1}{1 + e^{\beta(-2t - \mu)}} \frac{6.76395 (tU\omega_p)^2}{N^4 \chi_0 [\omega_0^2 + (-bt)^2]} \quad (4.49)$$

where  $\mu$  is given by (4.45). Using Eq. (4.49) for both lattice axes (practically, it means writing this expression with all the variables having index  $x$  and then  $y$ ), taking squares and summing, it follows that the conductivity of a 2D rectangular lattice is given by

$$\sigma^2 \cong \frac{45.751(t_x U_x \omega_p)^4}{\left(1 + e^{\beta(-2t_x - \mu_x)}\right)^4 N_x^8 \chi_0^2 \left(\omega_0^2 - (bt_x)^2\right)^2} + \frac{45.751(t_y U_y \omega_p)^4}{\left(1 + e^{\beta(-2t_y - \mu_y)}\right)^4 N_y^8 \chi_0^2 \left(\omega_0^2 - (bt_y)^2\right)^2} \quad (4.50)$$

Modeling a 2D lattice by using Eq. (4.50) consists of a choice of material parameters in this expression, and a comparison of the calculated values of the conductivity with experiments for various values of the parameters. In the following, parameters were chosen in similarity with the values previously used for the organic conductors [24].

Eq. (4.50) can be simplified by introducing ratios of the values of various parameters along the two lattice axes. Let  $t_y = \alpha t_x$ ,  $U_y = \gamma U_x$ ,  $\beta_y = \beta_x$ ,  $N_y = \delta N_x$ ,  $s_y = \lambda s_x$ ,  $n_y = \theta n_x$ . All the ratios are positive numbers. Inserting the ratios into Eq. (4.50), it follows that

$$\sigma^2 = \frac{45.751(t_x U_x \omega_p)^4}{N_x^8 \chi_0^2} \left[ \frac{1}{\left(\omega_0^2 - b^2 t_x^2\right)^2 \left(1 + e^{\beta_x \left(-2t_x - \frac{(n_x s_x - 1) t_x^7 \beta_x^6}{1.1029 + 0.1694(\beta_x t_x)^2 + 0.0654(\beta_x t_x)^4}\right)}\right)^4} + \frac{(a\gamma)^4}{\delta^8 \left(\omega_0^2 - b^2 a^2 t_x^2\right)^2 \left(1 + e^{\beta_x \left(-2at_x - \frac{(\beta_x at_x)^6 a_x t_x (\theta n_x s_x - 1)}{1.1029 + 0.1694(a\beta_x t_x)^2 + 0.0654(at_x \beta_x)^4}\right)}\right)^4} \right] \quad (4.51)$$

Eq. (4.51) has two singular points:  $\omega_0 = bt_x$  and  $\omega_0 = \alpha bt_x$ . Their existence is due to the fact that Eq. (4.51) is the first approximation to the expression for the electrical conductivity of a 1D HM, derived within the MFM.

Expression (4.51) gives the possibility of following theoretically changes in conductivity with the change of various material parameters. Such calculations represent an aspect of modeling a material. The most common experimentally variable parameter is the temperature to which a material is subdued.

As an example, the following values of the ratios in Eq. (4.51) were chosen:  $\alpha = 0.25$ ,  $\gamma = 0.25$  and  $\delta = \lambda = \theta = 1$ . Values of constants occurring in Eq. (4.51) were chosen as follows:  $N_x = 150$ ;  $\chi_0 = 1/3$ ;  $b = -1.83879$ ,  $\omega_0 = 2.8t_x$ ,  $\omega_p = 12t_x$ ,  $U_x = 4t_x$  and  $\beta_x = 11600/T$ .

Inserting all these values into Eq. (4.51) and normalizing the conductivity to  $\sigma = 1$  at  $t_x = t_y = 0.01$ ,  $n_x = n_y = 0.8$  and  $T = 116$  K, one gets the following Figures 4.1 and 4.2:

Another parameter interesting for experiments and modelization is the band filling. Experimentally speaking, it can be changed by doping a specimen. Figures 4.3–4.5 show the dependence of the normalized electrical

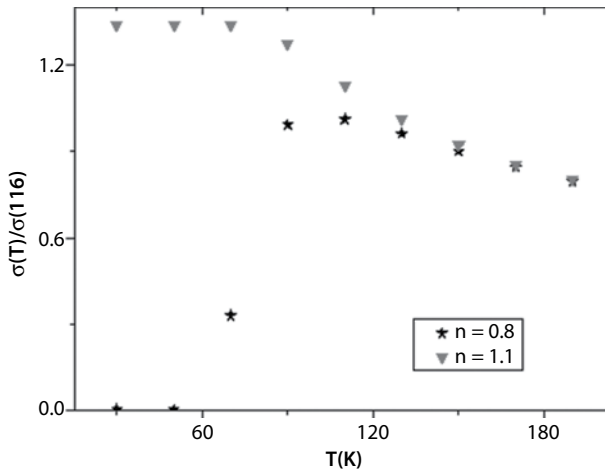


**Figure 4.1** Normalized conductivity of a rectangular 2D lattice as a function of temperature for two values of the band filling.

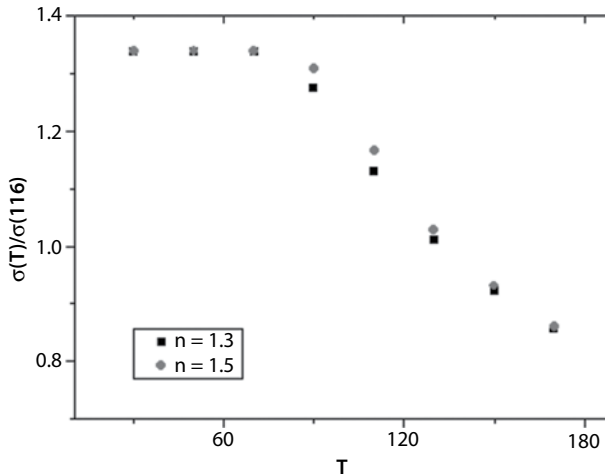


**Figure 4.2** Normalized conductivity of a 2D lattice, but for different values of the band filling.

conductivity of a rectangular 2D lattice as a function of the ratio  $\theta = n_y/n_x$ . The values of various parameters were chosen as follows:  $N_x = 150$ ,  $\chi_0 = 1/3$ ,  $\delta = 0.5$ ,  $\alpha = 0.5$ ,  $\gamma = 1$ ,  $\lambda = 1$ ,  $\omega_0 = 2.8t_x$ ,  $\omega_p = 12t_x$ ,  $s_x = 1$  and  $U = 4t_x$ . The conductivity was normalized to 1 at the point  $t_x = 0.03$ ,  $n_x = 0.9$ ,  $T = 120$  and  $\theta = 1$ .

Mathematically speaking, the parameter  $\theta$  is the ratio of the band fillings along the two lattice axes. This ratio can experimentally be changed by

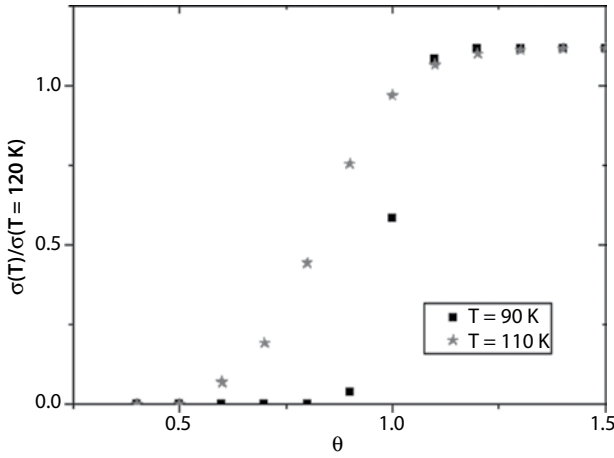


Figure 4.3 Normalized conductivity of a 2D lattice as a function of doping.

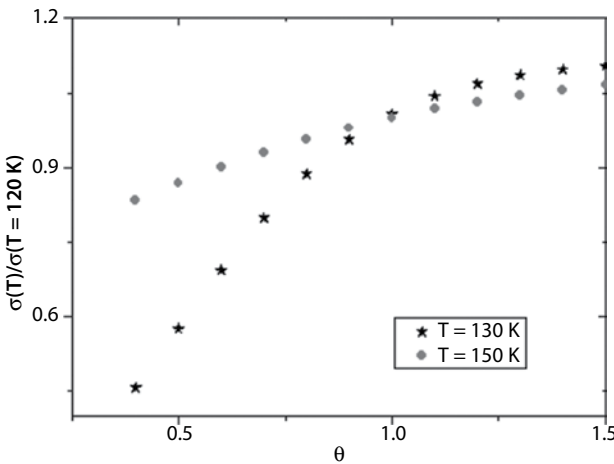
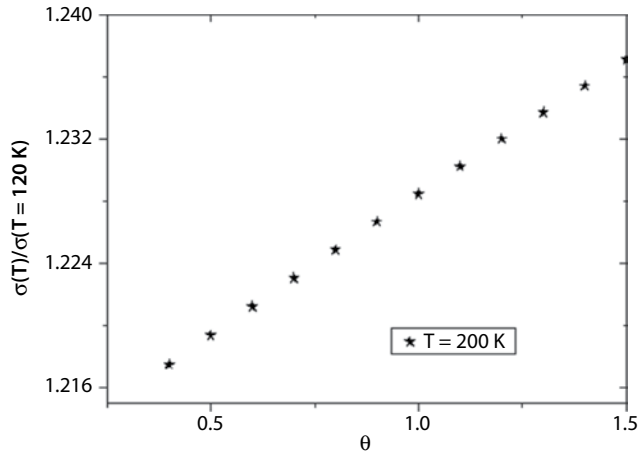


Figure 4.4 Normalized conductivity of a 2D lattice as a function of doping for  $T=130\text{ K}$  and  $T=150\text{ K}$ .





**Figure 4.5** The conductivity as a function of doping for  $T = 200 \text{ K}$ .

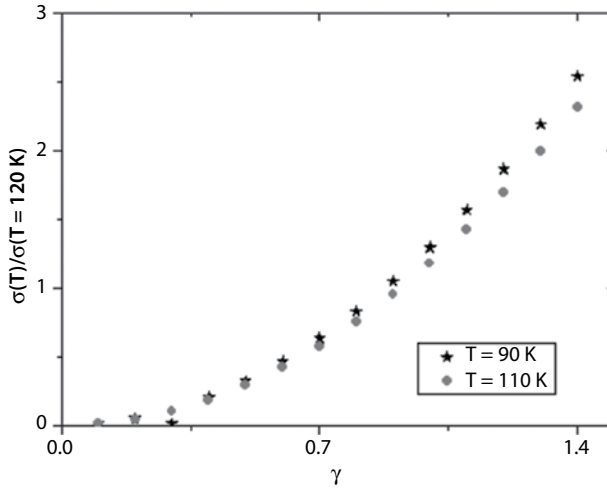
doping the specimen, which directly opens up the possibility of changing the characteristics of the material.

Figure 4.4 shows essentially the same function, but for two higher values of the temperature. The difference in behavior is obvious. The change in the dependence of the conductivity on the doping is even more clearly visible when comparing Figures 4.3–4.5. Judging from the three figures, it can be concluded that the lower the temperature the quicker is the rise of the conductivity.

In line with such a conclusion, the slope of this curve is the lowest for the highest temperature that was chosen as an example,  $T = 200 \text{ K}$ . In future work, it will be attempted to verify the validity of this conclusion (preliminary at present) for a wider range of parameters of the HM.

Figure 4.6 shows an interesting result: the normalized conductivity expressed as a function of the ratio  $\gamma$ . Physically, this is the ratio of the electron–electron interaction strength for pair of electrons in ions on the lattice sites along the two lattice axes. A small influence of the temperature is also visible on the figure.

All the calculations discussed so far contain a “hidden” assumption. Namely, it is presumed everywhere that the lattice constant is indeed a constant. However, under various circumstances, the lattice constant can vary, and the obvious question is how does one take this variation into account. The lattice constant can vary in two kinds of experimental situations: when a material is subdued to high external pressure, or, in the opposite, when it is stretched. Stretching a material may seem odd at first sight, but there exist an increasing number of experimentally relevant situations when



**Figure 4.6** The conductivity as a function of the ratio  $\gamma = U_y/U_x$ .

precisely that is being done. On the applicative side, stretchable materials are extensively investigated in view of applications in medical electronics. Examples of recent work in this direction are [30, 31]. The applicability of the HM to stretchable materials has recently been studied in [25].

Any considerations of the change of the lattice constant demand the introduction of the notion of strain  $\varepsilon$ . Applying a strain  $\varepsilon$  to an object of initial length  $l_0$  means that the length will become  $l = l_0 (1 + \varepsilon)$ .

Before embarking on a calculation of the changes of conductivity under the influence of stretching, one has to determine the changes under stretching of two important parameters: the band filling  $n$  and the hopping energy  $t$ . The band filling is in a 1D case defined as the quotient  $n = N/L$ , where  $N$  denotes the number of electrons and  $L$  is the length of the specimen. Because of the presence of strain, one can apply the defining relation of the strain:  $L(\varepsilon) = L_0 (1 + \varepsilon)$ . It follows that  $n(\varepsilon) = n_0/(1 + \varepsilon)$ . The hopping  $t$  is the physical consequence of the overlap of electronic wave functions in atoms on adjacent lattice sites. As such, it can be expected that any changes of the lattice constant leave “a trace” on the hopping energy. A first approximation to the strain dependence of the hopping can be expressed as

$$t = t_0 (1 - \varepsilon) \quad (4.52)$$

A particular case of the application of this expression is illustrated in Figure 4.7, taken from [25]. It refers to a 1D lattice for two different values of the temperature. The calculation was performed by the MFM, and the

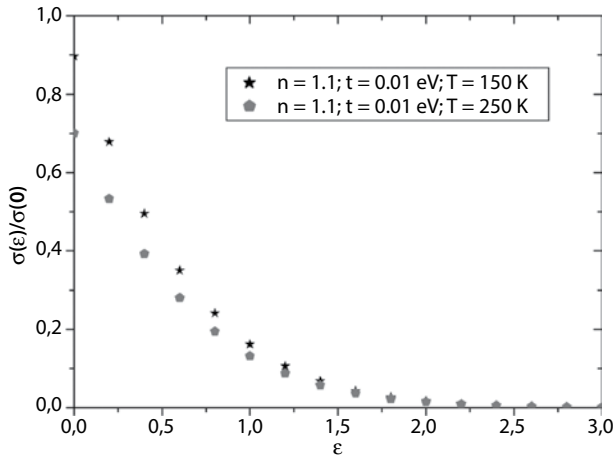


**Figure 4.7** The conductivity of a 1D lattice as a function of strain.

conductivity was normalized to 1 at the point  $n = 0.9$ ;  $T = 116$ K. Thinking in terms of a phase diagram, Figure 4.7 can be interpreted as meaning that for  $\epsilon \geq 2$  the material undergoes a phase transition from the conducting to an insulating phase. Other figures can also be interpreted in a similar way. Theoretical conclusions about the phase diagram of a material can thus be obtained.

Expression (4.52) is obviously simple. The strain dependence of the hopping energy is due to the overlap of the electronic wave functions on adjacent ions in a lattice. Determining this overlap for arbitrary ions on a lattice would be a complex quantum mechanical problem. A somewhat simplified but realistic approximation to the overlap can be found in standard quantum mechanics, which gives

$$t = t_0 \left[ 1 + r + \frac{1}{3}r^2 \right] \times e^{-r} \quad (4.53)$$

where  $r$  is the distance expressed in the Bohr radii. Inserting the definition of strain in this relation, and then developing into series in  $\epsilon$  it follows that

$$t \cong 0.86t_0 (1 - 0.2866\epsilon) \quad (4.54)$$

Figure 4.8 shows the conductivity of a 2D rectangular lattice as a function of the applied strain. Note that Figures 4.7 and 4.8 have been obtained by the full expression for the conductivity, given by Eqs. (4.43), (4.44), and (4.48) of the present chapter. The simplified form, given by Eq. (4.49), was used in the present contribution in order to render the calculations somewhat simpler.

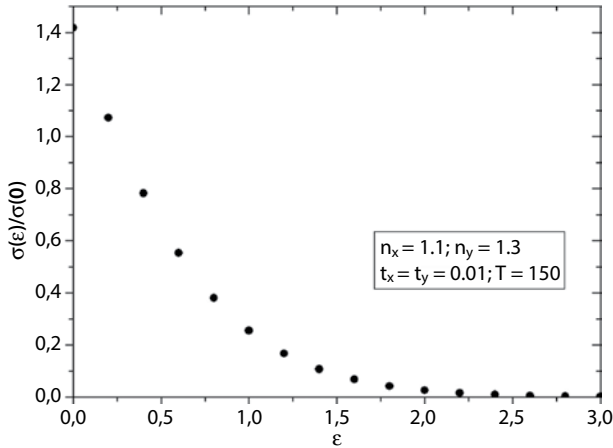


**Figure 4.8** The conductivity of a 2D lattice as a function of applied strain.

#### 4.4 The Hubbard Model and Optics

The basic equations that describe the reflection of an electromagnetic wave from a surface have already been discussed in this paper around Eq. (4.20). However, an important but so far unanswered question concerns the motivation for such calculations. Is it purely theoretical, or there is also a “hidden” experimental motivation.

As the reader may already “feel”, there is an important experimental motivation for calculating the reflectivity and attempting to link it with the conductivity. Namely, it is easier to perform a measurement of the reflectivity than to measure the conductivity. On the other hand, there are more situations in condensed matter physics and material science where values of conductivity are needed. This illustrates the necessity of establishing some form of a theoretical link between the values of the reflectivity and conductivity of a material.

Human beings and optical instruments detect cold solid objects by detecting light from some kind of a source which they reflect. It is not important if the “cold solid object” is a crater on the Moon or a laboratory object on Earth. The principle is always the same.

The possibility of “somehow” achieving invisibility of various objects has occupied writers for a long period. Although the literature on the adventures of “the invisible man” was a very interesting, real scientific research work on the subject is relatively recent. One of the main centers of research on invisibility is the group of Sir John Pendry at Imperial College in London, which is very active in work on invisibility cloaks. For details

about the work of this group, see <http://www.cmth.ph.ic.ac.uk/phonics/Newphonics/research>.

Reflectivity of any material depends on a subset of the set of all of its parameters. Logically then, a material designed with a chosen set of parameters, on which the reflectivity depends, should lead to a predictable value of the reflectivity. However, in order to enable such material design, one must have some model of the material, which of its parameters are important and a possible way of influencing and controlling them [33]. The model that will be used here is of course the HM. It will be shown that values of reflectivity can be related with values of various parameters of the HM, and ultimately with the electrical conductivity.

Reflectivity of any material can have a value between 0 and 1, where 1 means that incident light is completely reflected and 0 that there is no reflection at all. As objects are visible due to reflection of light, it follows that an object with reflectivity 0 is invisible. It will be attempted in the continuation to find values of the HM parameters for which reflectivity becomes as close as possible to zero.

Expressions for the calculation of reflectivity are given in Eqs. (4.23) and (4.24). Using the fact that

$$\frac{1-ax}{1+ay} = (1-ax) \sum_{l=0}^{\infty} (-1)^l (ay)^l \quad (4.55)$$

it can be shown that the reflectivity  $R$  can be expressed as the following series:

$$R \cong 1 - 2 \frac{K\omega_0}{\pi\sigma_R} + 2 \left( \frac{K\omega_0}{\pi\sigma_R} \right)^2 - \frac{3}{2} \left( \frac{K\omega_0}{\pi\sigma_R} \right)^3 + \dots \quad (4.56)$$

As it is formulated, Eq. (4.56) does not directly involve the dimensionality of the system under consideration. However, dimensionality enters indirectly, through the functions  $K$  and  $\sigma_R$ , because they depend on the dimensionality.

Figure 4.9 represents the dependence of the reflectivity of a 1D HM on the temperature. The band filling and hopping energy were chosen arbitrarily. The conductivity, which had to be calculated at first, was normalized to  $\sigma_R = 1$  for  $t = 0.005$  eV;  $T = 116$  K [34].

Note an interesting detail on this figure. For sufficiently low temperatures, the reflectivity becomes low, while for higher temperatures it is only slightly below 1. This means that with the decrease of  $T$  it becomes more difficult to see the object. It would be interesting to verify this conclusion for several pairs of values  $(n, t)$ , but this can be performed by the interested reader.

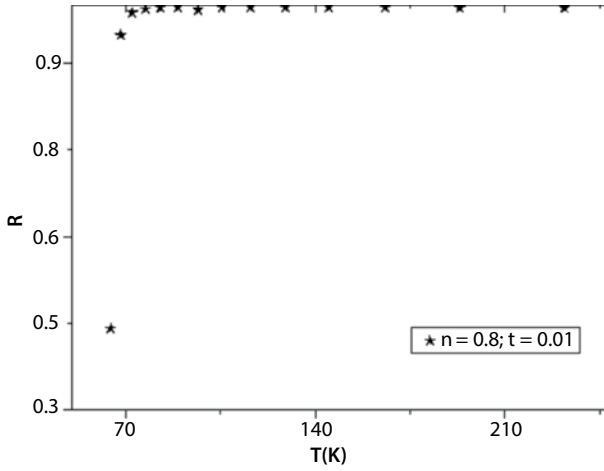


**Figure 4.9** Reflectivity as a function of temperature for a 1D HM.

A 2D HM is a physically more interesting system. The reflectivity of this system could (in principle) be determined by starting from the 2D HM and calculating the conductivity and reflectivity by using their respective definitions. Another, easier way, applicable to rectangular lattices is to introduce a change of variables:  $\sigma_R = \sqrt{\sigma_{Rx}^2 + \sigma_{Ry}^2}$ .

Inserting this change of variables in Eq. (4.56) leads to

$$R \cong 1 - \frac{2K\omega_0}{\pi\sqrt{\sigma_{Rx}^2 + \sigma_{Ry}^2}} + 2\left(\frac{K\omega_0}{\pi\sqrt{\sigma_{Rx}^2 + \sigma_{Ry}^2}}\right)^2 - \frac{3}{2}\left(\frac{K\omega_0}{\pi\sqrt{\sigma_{Rx}^2 + \sigma_{Ry}^2}}\right)^3 + \dots \quad (4.57)$$

Now assume that the conductivities along the two lattice sides are mutually independent, and introduce their ratio

$$\frac{\sigma_{Ry}}{\sigma_{Rx}} = \Gamma \quad (4.58)$$

Taking that the imaginary component of the conductivity is zero, some algebra leads to the following result for the function  $K$

$$K_{1,2}^2 = -\frac{1}{2} \pm \frac{1}{2\omega_0^2} \sqrt{\omega_0^4 + (4\pi\omega_0)^2 (1 + \Gamma^2) \sigma_{Rx}^2} \quad (4.59)$$

The real component of the conductivity is a function of a certain number of parameters of the HM and the temperature. Introducing Eq. (4.59) into Eq. (4.57) would give a result for the reflectivity of a 2D HM on a rectangular lattice, as a function of parameters of the lattice sides, the temperature

and the ratio of conductivities along the two sides. This amounts to opening the possibility of modeling a 2D material with a rectangular lattice.

As the easiest example, take that  $\Gamma = 0$ . This means that one of the lattice sides is not conducting, and the problem reduces to a 1D HM.

What would the conductivity be if the system is highly anisotropic, for example, if  $\Gamma = 0.1$ ? Practically speaking, this would mean that the conductivity along the  $y$  axis is 10 times smaller than along the  $x$  axis of the lattice. Details of the calculation are available in [34], and the final result is shown in Figure 4.10.

Note on Figure 4.10 that for low temperatures the value of  $R$  tends to zero. This again points to the same conclusion as the one reached after Figure 4.9—that the lower the temperature, the more difficult it becomes to see an object.

Figure 4.11 shows the reflectivity of a 2D lattice expressed as a function of the temperature for the case when the ratio of conductivities along the two axes is  $1/2$ . It is interesting to note that the only change between Figures 4.10 and 4.11 is the value of reflectivity around the point  $T = 60$  K.

An interesting problem, having potential applicability is the dependence of the reflectivity on doping. Especially in the case of the 2D HM, any such dependence could have direct implications on the manufacture of various kinds of optically active planar surfaces.

The series in Eq. (4.56) is convergent under the condition that

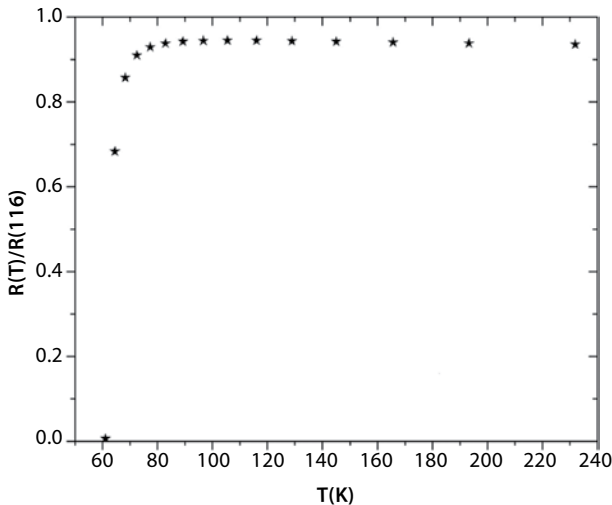


**Figure 4.10** Reflectivity of a 2D rectangular lattice for  $\Gamma = 0.1$ .

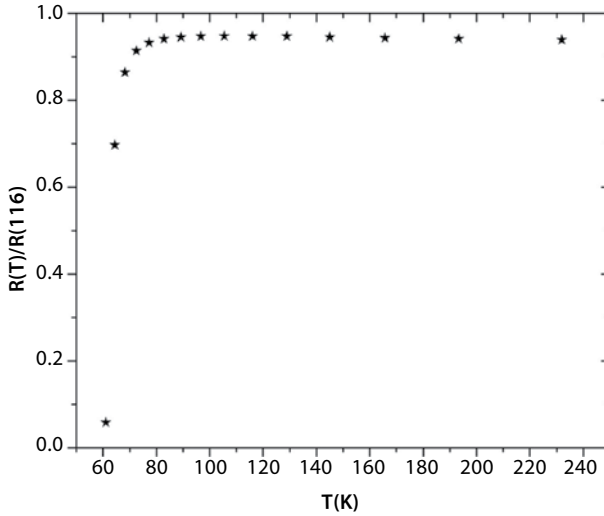


**Figure 4.11** Reflectivity of a 2D rectangular lattice for  $\Gamma = 0.5$ .

$$\frac{K\omega_0}{\pi\sigma_R} < 1 \quad (4.60)$$

Figure 4.4 gives the dependence of the conductivity of a 2D lattice on the parameter denoted by  $\theta = n_y/n_x$ . This parameter describes the variation of band filling of one lattice axis with respect to the other, which amounts to variation of doping. Take arbitrarily two points at  $T = 150$  K as representative:  $\theta = 0.4$ ;  $\theta = 0.8$ . Making all the calculations, it follows (up to first order) that for  $\theta = 0.4$ ;  $R \cong 0.496$  and for the second chosen point  $R \cong 0.5288$ . A graph of this dependence for the temperature  $T = 150$  K is shown on Figure 4.12.

The ratio  $\theta$  is defined as the quotient  $n_y/n_x$ . A simple inspection of Figure 4.11 shows that reflectivity increases with the increase of this ratio. This further means that (up to first-order) Hubbard plains made up of rectangular lattices are more reflecting the more their axes differ in band fillings.

#### 4.4.1 HM and Invisibility

Rendering and object invisible basically means making “somehow” its reflectivity equal or close to zero. In a multitude of recent papers, it is attempted to achieve this by enclosing the object under study in various



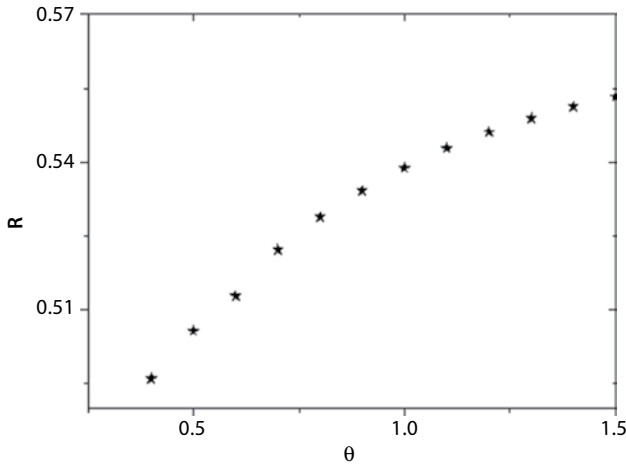


**Figure 4.12** Reflectivity of a 2D lattice as a function of  $\theta$  for  $T = 150$  K.

kinds of cloaks. Some years ago, the present author became interested in a simpler theoretical approach to the problem. The logic of this approach is extremely simple.

Imagine that there exists a (somehow derived) theoretical expression for the calculation of the reflectivity and that it contains a certain number of material parameters. Then it should be possible to invert the calculation: that is to choose the parameters so as to obtain a value of the reflectivity arbitrarily close to zero. This would mean theoretically achieving invisibility within a particular model of a material. In the present chapter, this was attempted within the HM.

First results are presented on Figures 4.10–4.12, which give the reflectivity as a function of various material parameters: the temperature and (essentially) doping along the two lattice axes. It can be seen on Figures 4.10 and 4.11 that the reflectivity drops to values close to zero at  $T \approx 60$  K. Figure 4.12 shows the dependence of the reflectivity on the ratio of the band fillings of the two axes, for a fixed temperature. It shows a steep decrease of reflectivity with the decrease of the parameter  $\theta$ .

Analytically, a simple estimate can be made of the position of the point at which  $R = 0$ . Impose the condition  $R = 0$  on Eq. (4.56) and solve for the value of  $K\omega_0/\pi\sigma_R$ . It follows by a simple calculation that

$$R = 0 \Leftrightarrow \frac{K\omega_0}{\pi\sigma_R} = 0.7449 \quad (4.61)$$

Reflectivity is a function of a set of material parameters. All of them can be tuned in experiments, but the one which is easiest to tune is the

temperature. This presents another possibility to theoretically achieve invisibility of an object. The reflectivity can be expressed as

$$R(T) \cong R(T_0) + \frac{\partial R}{\partial T}(T - T_0) \quad (4.62)$$

where

$$\frac{\partial R}{\partial T} = \frac{\partial R}{\partial \sigma_R} \frac{\partial \sigma_R}{\partial T} \quad (4.63)$$

All the derivatives in Eq. (4.63) can be determined using the results of the present chapter. The temperature at which reflectivity becomes close to zero can be calculated from Eq. (4.62) as

$$T = T_0 - \left( \frac{\partial R}{\partial T} \right)^{-1} R(T_0) \quad (4.64)$$

## 4.5 Conclusions

The aim of this chapter was to present a self-contained introduction to the HM and some of the possible applications. The choice of the applications was influenced by the research experience of the author. The model was introduced and its basics explained by using known literature approaches. Concerning the calculations, the MFM was introduced and its main equations presented. The DMRG method was described and some of the main references given. The MFM was applied to the calculation of the electrical conductivity of the 1D and 2D rectangular lattices. Variation of the parameters led to interesting results of the conductivities, and this was explored to some extent. In this way, modelization of materials became possible.

The reader has probably noted that the calculations were performed for 2D square rectangular lattices, but without any kind of explanation. The motivation is that there is general belief that such lattices capture the essential physics of high-temperature superconductors. This idea was initiated by P.W. Anderson back in 1988.

It would be exaggerated to pretend that this chapter is a “complete” treatment of the HM. This chapter goes into considerable detail in several aspects of the HM: the basics, methodology of calculation, use of the calculated transport properties in modeling 1D and 2D materials. As a difference with various other reviews of the HM, the present chapter considers the problem of reflectivity of the HM in some detail. Apart from the

calculation of reflectivity, this chapter contains a brief consideration of the problem of invisibility within the HM.

Calculations discussed in this chapter are methodologically correct, but the numerical results are only approximate; various developments have been pursued only to lowest order. In any future work on the HM, it will be attempted to improve several aspects of this text or add some which were not considered at all.

All the developments will be pushed to a higher number of terms. Expressions thus obtained will be used in actual calculations. The results discussed in this chapter represent a form of the phase diagram of the HM, both in 1D and 2D. These considerations will be generalized in the future.

A very interesting aspect of the HM has not been considered at all in this text. This is the application of the gauge–gravity duality to research in condensed matter physics [37]. A very attractive aspect of this duality is that it opens the possibility of linking research in gravitation theory with work in condensed matter.

## Acknowledgment

This study was prepared within the project OI 171017 of the Ministry of Education, Science and Technological Development of Serbia.

## References

1. Thomson, J. J., “Cathode rays”, *The Electrician*, 39, 104, 1897.
2. Mott, N. F., “Metal-insulator transitions”, *Proc. Roy. Soc. London*, A382, 1, 1982.
3. Imada, M., Fujimori, A., and Tokura, Y., “Metal-insulator transitions”, *Rev. Mod. Phys.*, 70, 1039, 1998.
4. Hubbard, J., “Electron correlations in narrow energy bands”, *Proc. Roy. Soc. London* A276, 238, 1963.
5. Editorial, “The Hubbard model at half a century”, *Nat. Phys.*, 9, 523, 2013.
6. Geim, A. K. and Novoselov, K. S., “The rise of graphene”, *Nat. Mater.*, 6, 183, 2007.
7. Mermin, N. D., “Crystalline order in two dimensions”, *Phys. Rev.*, 176, 250, 1968.
8. Ferrari, A. C. *et al.* “Science and technology roadmap for graphene, two-dimensional crystals and hybrid systems”, *Nanoscale*, 7, 4598, 2015.
9. Lieb, E. H. and Wu, F. Y., “Absence of Mott transition in an exact solution of the short-range, one band model in one dimension”, *Phys. Rev. Lett.*, 20, 1445, 1968.

10. Lieb, E. H. and Wu, F. Y., “The one-dimensional Hubbard model: a reminiscence”, *Physica A*, 321, 1, 2003.
11. White, S. R., “Density matrix formulation for quantum renormalisation groups”, *Phys. Rev. Lett.*, 69, 2863, 1992.
12. White, S. R., “Density matrix algorithms for quantum renormalisation groups”, *Phys. Rev., B*, 48, 10345, 1993.
13. Schollwoeck, U., “The density-matrix renormalisation group”, *Rev. Mod. Phys.*, 77, 259, 2005.
14. Schollwoeck, U., “The density-matrix renormalisation group in the age of matrix product states”, *Ann. Phys.*, 326, 96, 2011.
15. Stroudenmire, E. M. and White, S. R., “Studying two-dimensional systems with the density matrix renormalization group”, *Annu. Rev. Condens. Matt. Phys.*, 3, 111, 2012.
16. Kubo, R., “Statistical-mechanical theory of irreversible processes I”, *J. Phys. Soc. Jpn*, 12, 570, 1957.
17. Mori, H., “Transport, collective motion and Brownian motion”, *Progr. Theor. Phys.*, 33, 423, 1965.
18. Mori, H., “A continued-fraction representation of time-correlation functions”, *Progr. Theor. Phys.*, 34, 399, 1965
19. Götze, W. and Wölfle, P., “Homogenous dynamical conductivity of simple metals”, *Phys. Rev. B*, 6, 1226, 1972.
20. Argyres, P. N. and Resendes, D. G., “Discussion of the memory function method”, *J. Phys.: Condens. Matter*, 1, 7001, 1989.
21. Lucas, A. and Sachdev, S., “Memory matrix theory of magnetotransport in strange metals”, *Phys. Rev. B*, 91, 195122, 2015.
22. Voit, J., “A brief introduction to Luttinger liquids”, *preprint cond-mat/0005114*, 2000.
23. Haldane, F. D. M., “Luttinger liquid theory of one-dimensional quantum fluids: I. Properties of the Luttinger model and their extension to the general 1D interacting spinless Fermi gas”, *J. Phys. C: Solid State Phys.*, 14, 2585, 1981.
24. Celebonovic, V., “Q1D organic metals—a theoretical determination of the electrical conductivity”, *Phys. Low-Dim. Struct.*, 3/4, 65, 1997.
25. Celebonovic, V., “The Hubbard model: useful for stretchable nano-materials?” *J. Phys. Conf. Ser.* 558, 012006, 2014.
26. Hussey, N. E., McBrien, M. N., Balicas, L. *et al.* “Three-dimensional Fermi-liquid ground state in the quasi-one-dimensional cuprate  $\text{PrBx}_2\text{Cu}_4\text{O}_8$ ”, *Phys. Rev. Lett.*, 89, 086601, 2002.
27. Lebed, A. G., “Non-Fermi-liquid crossovers in a quasi-one-dimensional conductor in a tilted magnetic field”, *Phys. Rev. Lett.*, 115, 157001, 2015.
28. Wallis, R. F. and Balkanski, M. *Many-Body Aspects of Solid State Spectroscopy*, North Holland, Amsterdam (1986).
29. Celebonovic, V. in *Trends in Materials Science Research*, Editor Caruta, B. M., Nova Science Publishers, New York, pp. 245–260 (2006).
30. Rogers, J. A. *et al.* “Materials and mechanics for stretchable electronics”, *Science*, 327, 1603, 2010.

31. Kim, Y., Zhu, J., Yeom, B. *et al.* “Stretchable nanoparticle conductors with self-organized conductive pathways”, *Nature*, 500, 59, 2013.
32. Gasiorowicz S., *Quantum Physics*, John Wiley, New York (1974)
33. Canfield, P. C., “Fishing the Fermi Sea”, *Nat. Phys.*, 4, 167, 2008.
34. Celebonovic, V., “The Hubbard model and optics: reflectivity of 1D and 2D systems”, *J. Phys. Conf. Ser.*, 398, 012009, 2012.
35. Chen, X., Luo, Y., Zhang, J. *et al.* “Macroscopic invisibility cloaking of visible light”, *arXiv 1012.2783*, 2010.
36. Yu, D., Lu, L., Joannopoulos, J. D. *et al.* “An invisible metallic mesh”, *arXiv1510.00016*, 2015.
37. Sachdev, S., “What can gauge-gravity duality teach us about condensed matter physics?” *Annu. Rev. Condens. Matter Phys.*, 3, 9, 2011.

# Heating and Melting in Impacts: Basic Theory and Possible Applications

V. Celebonovic<sup>1</sup> · M. Nikolic<sup>1</sup>

Received: 22 March 2015 / Accepted: 7 July 2015 / Published online: 23 July 2015  
© Springer Science+Business Media New York 2015

**Abstract** Mutual collisions and impacts of solids occur in systems of widely different scales. The aim of this paper is to present a calculation of the change of temperature which a solid target undergoes when hit by a solid impactor. As a test, the equations derived are applied to examples of laboratory experimental data, and the results are physically plausible.

**Keywords** Modeling · Heating · Melting · Impacts

## 1 Introduction

Mutual collisions of solid objects with different masses occur in nature on scales ranging from impacts of “small bodies” into planetary surfaces to impacts of small projectiles and atoms or molecules into surfaces of solids in laboratory experiments. One of the expected consequences of such collisions is heating, and, under favorable circumstances, melting of the target at the point of impact.

The aim of this paper is to develop the basics of the theory of impact heating and melting. General expressions for the speed of the projectile needed to heat up the target will be derived, and then tested for a particular form of the critical stress needed to fracture the material of the target. Testing will be performed on a recent set of experimental data. This is a continuation and extension of earlier work on the subject by one of the authors [1].

---

✉ V. Celebonovic  
vladan@ipb.ac.rs

<sup>1</sup> Institute of Physics, University of Belgrade, Pregevica 118, 11080 Zemun-Belgrade, Serbia

## 2 The Basic Equations

Imagine a projectile heading for impact into a solid surface. It has some kinetic energy,  $E_k$ , which upon impact will be divided into two: a part, denoted by  $E_f$  will be used for fracturing the target, and the remainder  $E_H$  will “go” on heating and ultimately melting the target. Therefore,

$$E_k = E_f + E_H. \quad (1)$$

The kinetic energy is determined by the mass and speed of the projectile and  $E_H$  by the specific heat and volume of the material.

Assuming that the impactor is a sphere of radius  $r_1$ , made up of a material with mass density  $\rho_1$ , moving with speed  $v_2$ , its kinetic energy is given by

$$E_k = \frac{2\pi}{3} \rho_1 r_1^3 v_2^2. \quad (2)$$

According to standard solid-state physics, the energy needed for making a fracture in a solid material of volume  $V$  is given by

$$E_f = \sigma_C V, \quad (3)$$

where  $\sigma_C$  is the critical stress needed for fracturing a solid. Finally, the energy needed to heat a volume  $V$  of a material from an initial temperature  $T_0$  up to a temperature  $T_1$  is

$$E_H = C_V \times V \times (T_1 - T_0), \quad (4)$$

where  $C_V$  is the specific heat of the material. Inserting Eqs. 2–4 into Eq. 1, it follows that in order to heat the target to some temperature  $T_1$ , the speed of the incoming projectile must be given by the following:

$$v_{2h}^2 = \frac{3\sigma_C V}{2\pi\rho_1 r_1^3} \times \left[ 1 + \frac{C_V}{\sigma_C} (T_1 - T_0) \right]. \quad (5)$$

This is a general result, independent on the particular form of  $\sigma_C$  and  $C_V$ .

The energy needed to heat a volume  $V_m$  of a material up to the melting temperature  $T_m$  is

$$E_M = C_V \times V_m \times (T_m - T_0) \quad (6)$$

and it follows that in this case

$$v_{2m}^2 = \frac{3\sigma_C V}{2\pi\rho_1 r_1^3} \times \left[ 1 + \frac{C_V}{\sigma_C} \frac{V_m}{V} (T_m - T_0) \right]. \quad (7)$$

In expressions 5 and 7, the symbol  $V$  denotes the volume of the crater formed as a result of the impact, and  $V_m$  is the volume of the melted material of the target. It is assumed here that in an impact in which melting of the target occurs, the volume of the melt can be different from the geometrical volume of the impact crater.

The volume of a crater depends on its shape; modeling it as a half of a rotating ellipsoid, the volume is  $V = \frac{2}{3}\pi abc$ , where  $a$  and  $b$  denote the dimensions of the “opening” of the crater and  $c$  is the depth. In order to render these two results applicable, one needs either “practical” expressions for the specific heat  $C_V$  and the critical stress for fracturing the target  $\sigma_C$ , or their measured values.

## 2.1 The Specific Heat and Critical Stress

Standard condensed matter theory shows that the specific heat of a crystalline solid at temperature  $T$  is [2]

$$C_V \cong 3N\nu k_B \times \left[ 1 - \frac{1}{20} \left( \frac{\theta_D}{T} \right)^2 \right], \quad (8)$$

where  $\nu$  is the number of particles in the elementary crystal cell,  $N$  is the number of elementary crystal cells in the specimen, and  $k_B$  is Boltzmann’s constant. It can be shown that the ratio  $\theta_D/T$  is given by [3]

$$\frac{\theta_D}{T} = \frac{\hbar}{k_B T} \times \left[ \frac{9\nu N}{4\pi V} \right]^{1/3} \times \left( \frac{\partial P}{\partial \rho} \right)^{1/2}. \quad (9)$$

The symbols  $P$  and  $\rho$  denote the pressure and mass density of a material, and  $V$  is the volume. The ratio  $\theta_D/T$  obviously depends on the expression for the equation of state of the material.

There exist in the literature various estimates of the critical stress needed to fracture a solid. One of the first is the result due to Griffith, [4], who showed that

$$\sigma_C = \left( \frac{2E\sigma}{\pi\nu z} \right)^{1/2}. \quad (10)$$

The meaning of various symbols is as follows:  $\sigma$  is the surface tension of a material,  $E$  is Young’s modulus,  $\nu$  is Poisson’s ratio, and  $z$  is the half length of the focal line of a crack preexisting in a material.

It follows from Eqs. 8–10 that

$$\frac{C_V}{\sigma_C} \cong 3N\nu k_B \left( \left( \frac{\pi\nu z}{2E\sigma} \right) \right)^{1/2} \times \left[ 1 - \frac{1}{20} \left( \frac{\hbar}{k_B T} \right)^2 \left( \frac{9N\nu}{4\pi V} \right)^{2/3} \frac{\partial P}{\partial \rho} \right]. \quad (11)$$

Inserting Eq. 11 into Eqs. 5 and 7, it is possible to obtain expressions for the impactor speeds needed for heating and melting the target at the point of impact.



## 2.2 The Difference $C_P - C_V$

The calculations discussed in the present paper require the knowledge of  $C_V$ , while experiments sometimes give the value of  $C_P$ . The conversion can be performed by the well-known thermodynamical identity

$$K_T \times (C_P - C_V) = TV\alpha_P^2, \quad (12)$$

where  $K_T = \frac{1}{\rho} \left( \frac{\partial \rho}{\partial P} \right)_T$ ,  $\alpha_P = \frac{1}{V} \left( \frac{\partial V}{\partial T} \right)_P$ ,  $T$  is the temperature, and  $V$  is the volume.

Clearly  $K_T = \frac{1}{B_0}$ , where  $B_0$  is the bulk modulus of the material. It follows that

$$C_P - C_V = \frac{TV}{K_T} \times \alpha_P^2 = TVB_0 \times \alpha_P^2 = \frac{B_0 T}{V} \times \left( \frac{\partial V}{\partial T} \right)^2. \quad (13)$$

As  $\frac{\partial V}{\partial T} = -\frac{V}{\rho} \frac{\partial \rho}{\partial T}$ , one finally gets

$$C_P - C_V = B_0 TV \times \frac{1}{\rho^2} \times \left( \frac{\partial \rho}{\partial T} \right)^2 = T \times V \times B_0 \times K_T^2. \quad (14)$$

This relation means that for systems with small volumes or large densities, the difference of specific heats tends to zero.

## 3 Possible Applications

Equations derived in the preceding section are applicable to impacts of solid projectiles into solid targets in laboratory and possibly natural situations. They give the possibility of addressing two kinds of problems: determining the heating of the target in the impact by a projectile with given physical parameters and speed, and determining the speed, density, and radius of the impactor needed to produce a given thermal effect in a given material (for instance to melt the target).

As an illustration of a laboratory application, take the study of Suzuki et al. [5]. In this experiment, projectiles of various masses, kinetic energies, and chemical composition were fired into different targets, and the properties of the resulting impact craters were measured. Their paper contains the data, which can be used to test the applicability of the equations derived here.

Completely arbitrarily, the experimental run *HY04* was chosen for analysis. In this particular run, a projectile of mass  $m = 3.98 \times 10^{-6}$  kg, diameter  $D = 10^{-3}$  m, and density  $\rho_1 = 7930$  kg·m<sup>-3</sup> was fired into a calcite target with the impact velocity  $v = 3.6$  km·s<sup>-1</sup>. The volume of the resulting crater was  $V = 9.90 \times 10^{-8}$  m<sup>3</sup> and the area of the crater  $S = 1.1429 \times 10^{-4}$  m<sup>2</sup>.

The chemical formula of calcite is CaCO<sub>3</sub>. Various parameters of this material have the following values. The molecular mass is  $M = 100.09$ , the mass density under standard conditions is 2710 kg·m<sup>-3</sup>, and the volume of the unit cell is  $V_{\text{cell}} = 3.6785 \times 10^{-28}$  m<sup>3</sup>. The melting temperature is  $T_m = 1167$  K [7]. The Poisson ratio

is  $v = 0.309$  [8] and the surface energy is  $\sigma = 0.347 \text{ J}\cdot\text{m}^{-2}$  [9]. The molar volume is  $V_{\text{mol}} = 31.2 \times 10^{-6} \text{ m}^3$  [10]. Finally, at  $T = 300 \text{ K}$   $C_p \cong 84 \text{ J}\cdot\text{mol}\cdot\text{K}^{-1}$  [11].

Application of Eq. 5 gives  $T_1 - T_0 \cong 100 \text{ K}$ . Physically, this means that the temperature of the target increased for approximately 100 K at the point of impact. The obvious question is how long did this increase of temperature last, and did it change the “macroscopic” parameters of the target? This time interval can be estimated by dividing the diameter of the crater with the speed of the impactor, and in this case it is  $3 \times 10^{-6} \text{ s}$ . In such a short time interval, no change of the “macroscopic” parameters of the target is expected to occur.

As another “real life” example, take the run *HY14* from [5]. The projectile used there had a mass of  $m = 1.46 \times 10^{-6} \text{ kg}$ , diameter  $D = 10^{-3} \text{ m}$ , density  $\rho = 2500 \text{ kg}\cdot\text{m}^{-3}$ , and the impact velocity of  $v = 7.1 \text{ km}\cdot\text{s}^{-1}$ . The volume of the crater was  $V = 9.24 \times 10^{-8} \text{ m}^3$  and the area of the crater  $S = 1.17 \times 10^{-4} \text{ m}^2$ . Performing the calculation as in the preceding example gives  $T_1 - T_0 \cong 140 \text{ K}$  and the effect of this heating will last approximately  $9 \times 10^{-7} \text{ s}$ .

If a projectile used in the preceding case impacts into an iron target, what speed should it have in order to melt the target at the impact point? All the parameters of iron needed for such a calculation are available at <http://www.periodictable.com>. Take, purely as an illustration, that the volume of the impact crater is  $V = 10^{-7} \text{ m}^3$ . Assuming that  $V_m/V = 0.25$ , it follows from Eq. 7 that  $v_{2m} \cong 8.17 \text{ km}\cdot\text{s}^{-1}$ .

Inverting the calculation gives the possibility of estimating the ratio  $V_m/V$  for different values of the impactor speed. It thus follows that for the parameters given above and an impact speed of  $10 \text{ km}\cdot\text{s}^{-1}$ ,  $V_m/V \cong 0.377$ , while for the speed of  $15 \text{ km}\cdot\text{s}^{-1}$ , one gets  $V_m/V \cong 0.854$ .

## 4 Discussion and Conclusions

Mutual collisions and impacts of solid bodies occur in various situations, and one of the expected consequences is the heating and in some cases melting of one or both of the objects. In this paper, we have developed a simple theory of heating and melting in impacts. The approach proposed here is based on the law of conservation of energy, and it is “simple” because it takes into account only the two main components on which the kinetic energy of the impactor is partitioned.

The results of the calculations were applied to three examples of impacts of projectiles into solid targets; two of these were taken from a real recent data set, while the third is an extension. Physically plausible results were obtained for the amount of heating of the target and for the speed of the projectile needed to melt the target. In the first example, it was shown that at the point of impact, the target heats up by  $\approx 100 \text{ K}$ . This heating does not have any visible macroscopic consequences because it lasts only  $\approx 10^{-6} \text{ s}$ .

The present paper is a continuation and extension of [1]. In that paper, it was assumed that the temperature to which the target heats up in an impact is smaller than the melting temperature, which was in turn calculated by a particular form of the Lindemann rule, and a possible allowed interval of various parameters of the impact was obtained.

Two approximations, deliberately made in the present work, will be corrected in the future. It was assumed here that the difference  $C_P - C_V$  tends to zero, and that one can use the measured value of  $C_P$  of the target material.

No account was taken of the possibility that in the moment of impact, some pieces of the target material get launched some distance away, carrying some kinetic energy. In the future, the calculation discussed here will be continued by invoking the result for the melting temperature of solids obtained in [6]. Another open possibility for application of this work is heating and melting under geophysically relevant conditions.

**Acknowledgments** This paper was prepared within the research Projects OI171017 and 171038 financed by the Ministry of Education, Science and Technological Development of Serbia.

## References

1. V. Celebonovic, *Serb. Astron. J.* **184**, 83–86 (2012)
2. L.D. Landau, E.M. Lifchitz, *Statistical Physics* (Nauka, Moscow, 1976)
3. O.L. Anderson, *Equations of State of Solids for Geophysics and Ceramic Science* (OUP, Oxford, 1995), pp. 52–53
4. A.A. Griffith, *Philos. Trans. R. Soc.* **A221**, 163–198 (1921)
5. A. Suzuki, S. Hakura, T. Hamura et al., *J. Geophys. Res.* **117**, E08012 (2012)
6. U. Buchenau, R. Zorn, M.A. Ramos, [arXiv:1311.4739](https://arxiv.org/abs/1311.4739) preprint (2013)
7. <http://www.mindat.org>. Accessed 13 July 2015
8. H. Gerceg, *Int. J. Rock Mech. Min. Sci.* **44**, 1–13 (2007)
9. A.T. Santhanam, Y. Gupta, *Int. J. Rock Mech. Min. Sci. Geomech. Abstr.* **5**, 253–259 (1968)
10. <http://www.database.iem.ac.ru/mincryst>. Accessed 10 Mar 2015
11. G.K. Jacobs, D.M. Kerrick, K.M. Krupka, *Phys. Chem. Miner.* **5**, 35–59 (1981)

## Luminescence thermometry via the two-dopant intensity ratio of $\text{Y}_2\text{O}_3:\text{Er}^{3+}, \text{Eu}^{3+}$

This content has been downloaded from IOPscience. Please scroll down to see the full text.

2016 J. Phys. D: Appl. Phys. 49 485104

(<http://iopscience.iop.org/0022-3727/49/48/485104>)

View [the table of contents for this issue](#), or go to the [journal homepage](#) for more

Download details:

IP Address: 131.232.13.6

This content was downloaded on 16/11/2016 at 12:04

Please note that [terms and conditions apply](#).

You may also be interested in:

[Sensing temperature via downshifting emissions of lanthanide-doped metal oxides and salts. A review](#)  
Miroslav D Dramianin

[Eu<sup>3+</sup>/Tb<sup>3+</sup>-codoped Y<sub>2</sub>O<sub>3</sub> nanophosphors: Rietveld refinement, bandgap and photoluminescence optimization](#)  
S Som and S K Sharma

[Temperature luminescence properties of Eu<sup>3+</sup>-doped Gd<sub>2</sub>O<sub>3</sub> phosphors](#)  
M G Nikoli, A Z Al-Juboori, V orevi et al.

[Luminescence properties of single-phase SrMg<sub>2</sub>La<sub>2</sub>W<sub>2</sub>O<sub>12</sub>:Tb<sup>3+</sup>, Sm<sup>3+</sup>, Tm<sup>3+</sup> phosphor for multicolor and white light emitting LEDs](#)  
K Pavani, J Suresh Kumar and L Rama Moorthy

[Rare earth \(Sm<sup>3+</sup> and Dy<sup>3+</sup>\)-doped gadolinium oxide nanomaterials for luminescence thermometry](#)  
Ayad Zwayen M Al-Juboori

[Thermographic properties of a Eu<sup>3+</sup>-doped \(Y<sub>0.75</sub>Gd<sub>0.25</sub>\)<sub>2</sub>O<sub>3</sub> nanophosphor under UV and x-ray excitation](#)  
M G Nikoli, V Lojpur, Ž Anti et al.

# Luminescence thermometry via the two-dopant intensity ratio of $\text{Y}_2\text{O}_3:\text{Er}^{3+}, \text{Eu}^{3+}$

Mihailo D Rabasović<sup>1</sup>, Branka D Murić<sup>1</sup>, Vladan Čelebonović<sup>1</sup>,  
Miodrag Mitrić<sup>2</sup>, Branislav M Jelenković<sup>1</sup> and Marko G Nikolić<sup>1</sup>

<sup>1</sup> Institute of Physics, University of Belgrade, Pregrevica 118, 11080 Belgrade-Zemun, Serbia

<sup>2</sup> Institute of Nuclear Sciences 'Vinča', University of Belgrade, PO Box 522, 11001 Belgrade, Serbia

E-mail: [nikolic@ipb.ac.rs](mailto:nikolic@ipb.ac.rs)

Received 14 June 2016, revised 30 September 2016

Accepted for publication 12 October 2016

Published 4 November 2016



## Abstract

In this work we investigated the photoluminescence properties of  $\text{Y}_2\text{O}_3:\text{Er}^{3+}, \text{Eu}^{3+}$  as a function of temperature and the possibility to use this material as a temperature sensor. Photoluminescence emission measurements with 532 nm laser excitation were recorded in the temperature range from 303 up to 573 K. The measured intensity ratio of erbium  $^4\text{S}_{3/2} \rightarrow ^4\text{I}_{15/2}$  and europium  $^5\text{D}_0 \rightarrow ^7\text{F}_2$  emission lines was used for determination of the temperature calibration curve. These emission lines are intense, narrow and well defined. The distance between the lines, being 47 nm, can be easily measured even with a low-resolution spectrometer. The calculated relative sensitivity of the temperature sensor was  $1.4\% \text{ K}^{-1}$  at 303 K, in the physiological temperature range, meaning that it could be successfully applied in biological studies.

Keywords: luminescence thermometry, temperature sensor,  $\text{Y}_2\text{O}_3:\text{Er}^{3+}, \text{Eu}^{3+}$

(Some figures may appear in colour only in the online journal)

## 1. Introduction

The measurement of temperature is important for the control and understanding of the behavior of various processes in engineering and science. Luminescent thermometry has recently become a very interesting topic in the field of scientific research, which has been shown by the significant number of works dealing with this topic [1–4]. This measurement technique is noninvasive and precise, working remotely by way of an optical detection system. It can be applied to the measurement of temperature of fast moving objects [5], and for temperature measurements in strong electric and magnetic fields as well as in devices where heating is achieved by microwaves [6]. It is possible to make very small submicron particles of phosphor materials that can be used as temperature sensors [7]. Traditional liquid-filled thermometers, thermocouples, pyrometers, and thermistors are generally not suitable for temperature measurements on scales below 10  $\mu\text{m}$  [8]. In order to improve this method there is a rising need for new thermophosphors with better characteristics, such as, higher sensitivity, greater quantum efficiency and wider temperature region of applicability.

Rare-earth luminescent phosphors represent an important group of materials since they have a very high luminescence quantum yield [9]. They have applications in many areas such as optics [10], bioimaging [11], high-energy physics [12], thermometry [13] etc. Rare earth oxides have high refractive index, large band gap, low phonon energy, chemical stability in high-temperature environments and do not react with harsh chemicals.

The luminescence intensity ratio method for temperature measurements is based on temperature dependence of a ratio of two emission line intensities in a photoluminescence spectrum. Two lines are considered appropriate for these measurements if they both have strong emission intensity in the entire temperature range and if their intensity ratio gives high temperature resolution. In the case of one dopant, the intensity ratio of two emission lines originating from different upper levels is used for temperature measurement (for example, see the works of Nikolić *et al*, Lojpur *et al*, Đačanin *et al* [14–16]). The main difficulty with this method is the low intensity of the emission line from the higher excitation level. In the case of  $\text{Eu}^{3+}$  ions, this is the emission line which corresponds to the transition  $^5\text{D}_1 \rightarrow ^7\text{F}_1$ , which can be seen in the work by

Dačanin *et al* [16]. In order to eliminate this problem and increase the intensity of measuring emission lines, we used two different dopant ions  $\text{Er}^{3+}$  and  $\text{Eu}^{3+}$ .

These two dopant ions are chosen, because they have different luminescence properties as a function of temperature. The difference in the position of energy levels of these two  $\text{RE}^{3+}$  ions leads to different dependence of luminescence intensity as a function of temperature. The big difference in energies between the ground state and excited states in  $\text{Eu}^{3+}$  indicates that the main process of temperature luminescence quenching will occur at higher temperatures through the charge transfer region. In the case of the  $\text{Er}^{3+}$  ion, the energy gap is several times lower than in the  $\text{Eu}^{3+}$  ion and the temperature luminescence quenching will be dominant at lower temperatures through a process of multiphonon relaxation. This leads to the conclusion that in the case of  $\text{Er}^{3+}$  and  $\text{Eu}^{3+}$  dopants, with their different temperature dependences of luminescence, high intensity ratio changes will be observed.

Furthermore,  $\text{Er}^{3+}$  and  $\text{Eu}^{3+}$  dopant ions have upper levels very close to the energy of the 532 nm photon, and laser excitation at 532 nm can be very efficient for both dopants. The concentration of dopant ions is determined in such a way that the emission line intensities are easily measured in the full desired temperature range. Emission lines are narrow and well defined, approximately 47 nm apart, and can easily be resolved even with a low-resolution spectrometer.

Applications of luminescence thermometry with two different dopants are discussed in publications of several authors. Combination of  $\text{Tb}^{3+}$  and  $\text{Eu}^{3+}$  dopant ions can be found in the work of Brites *et al* [17]. Maximum sensitivity of this thermophosphor was  $4.9\% \text{ K}^{-1}$  at 150 K, with a region of applicability from 100 to 200 K. Another group of authors have also used the same dopant ions,  $\text{Tb}^{3+}$  and  $\text{Eu}^{3+}$ , where they obtained the relative sensitivity of  $2.85\% \text{ K}^{-1}$  at 14 K. This thermophosphor can be used in the temperature interval from 14 to 320 K [18]. Rai *et al* and Dey *et al* have shown in their works that  $\text{Y}_2\text{O}_3:\text{Eu}^{3+}, \text{Er}^{3+}, \text{Yb}^{3+}$  phosphor can also be used for temperature measurement [19, 20]. In these papers authors are using 980 nm excitaton and the intensity ratio of two  $\text{Er}^{3+}$  emission lines. In the work of Ishiwada *et al*  $\text{Y}_2\text{O}_3:\text{Tb}^{3+}, \text{Tm}^{3+}$  thermographic phosphor is used for high-temperature thermometry up to 1100 K [21].

When two dopants are used, their homogeneous distribution in the matrix is crucial for intense and uniform luminescence signal response. We already pointed out the advantages of soft chemistry methods, such as spray pyrolysis and hydrothermal synthesis, in the synthesis of such particles [22, 23]. Along with them, the polymer complex solution combustion method is proved to be simple and efficient for the synthesis of nanometric size particles [24–26]. The simplicity and easiness to control the particle size of the products enables synthesis of well crystallized nanoparticles sized from 20 to 100 nm, which can be easily functionalized towards biological application [27] or converted in transparent ceramic which retains good optical properties of the starting nano powders [26]. In this study we used the same method for the synthesis of  $\text{Y}_2\text{O}_3:\text{Er}^{3+}, \text{Eu}^{3+}$  phosphor particles and corresponding synthered specimens in order to investigate their

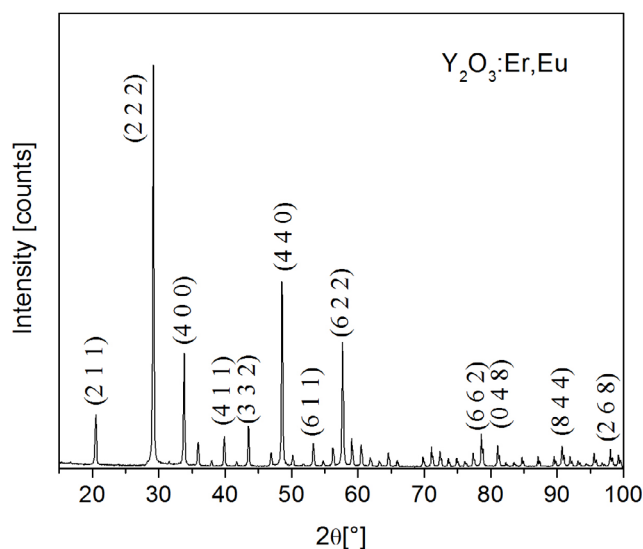


**Figure 1.** XRD patterns of the  $\text{Y}_2\text{O}_3:\text{Er}^{3+}, \text{Eu}^{3+}$  sample, indexed according to space group Ia-3 (no. 206).

potential application as a temperature sensor in the physiological temperature range (25–45 °C). It is well-known that temperature plays a crucial role in determining cell division rates, affects structure of the biomolecules and its monitoring could be used for early detection of many diseases. Today, various optically active nanosized crystals have attracted considerable attention because of strongly size-dependent optical properties. To be applicable for such a purpose they should be nontoxic, stable under specific light irradiation and hydrophilic. To accomplish the latter,  $\text{RE}^{3+}$  doped  $\text{Y}_2\text{O}_3$  particle surfaces were usually functionalized with amino groups (which do not deteriorate luminescence) via a reverse microemulsion [28] or the Stöber method [27]. A review of bulk ceramics already used luminescent probes and sensors for temperature measuring, see Wang *et al* [29].

## 2. Materials and methods

A sample of  $\text{Y}_2\text{O}_3:\text{Er}^{3+}, \text{Eu}^{3+}$  with a concentration of 3 at.%  $\text{Er}^{3+}$  and 1 at.%  $\text{Eu}^{3+}$  ions, was prepared by the polymer complex solution combustion method. The sample powder was pressed (200 MPa) into a pellet and sintered at 1200 °C for three hours.

The phase structures of the sample were measured by the powder x-ray diffractometer type Philips PW 1050 instrument, using Ni filtered Cu K 1.2 radiation in a  $2\theta$  range from 10–100 counting for 5 s in 0.05 steps. X-ray diffraction analysis confirms that  $\text{Y}_2\text{O}_3:\text{Er}^{3+}, \text{Eu}^{3+}$  powder samples crystallize in a cubic bixbyite type and measured diffraction peaks of the sample are presented in figure 1. The diffraction peaks are indexed according to space group Ia-3 (no. 206).

The experimental setup for luminescence measurement as a function of temperature is shown in figure 2. The photoluminescence emission spectra measurements were performed under continuous excitation light of the 30 mW diode pumped solid state cw laser at 532 nm and collected by the Ocean Optics USB 2000 spectrometer. Temperature of the sample is

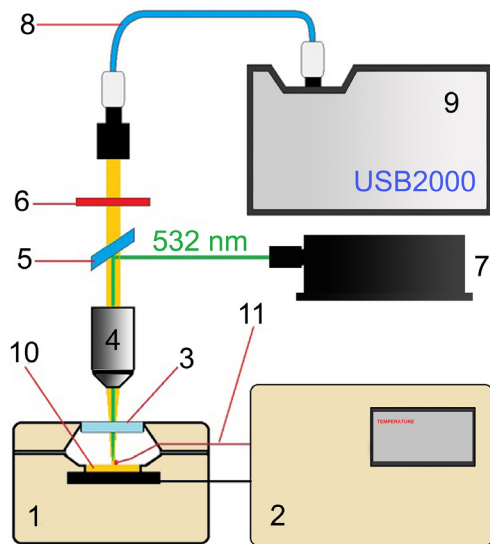


**Figure 2.** Experimental setup for temperature measurements by luminescence: 1—furnace; 2—temperature control unit; 3—quartz window; 4—microscope objective 4 $\times$ ; 5—beam splitter; 6—band-stop filter at 540 nm; 7—532 nm laser; 8—optical fiber; 9—spectrometer; 10—sample; 11—thermocouple.

controlled by a home-made furnace. The luminescence excitation measurements were performed at room temperature on the Spex Fluorolog spectrofluorometer system with C31034 cooled photomultiplier, utilizing 500 W Xenon lamp as the excitation source.

### 3. Results and discussion

The excitation spectra of the sample are shown in figure 3. They are recorded at wavelengths of 565 and 611 nm which correspond to the positions of the most intense emission lines of the  $\text{Er}^{3+}$  and  $\text{Eu}^{3+}$  dopant ions. It can be seen that the excitation laser wavelength of 532 nm is at the same position as the absorption lines  $^4I_{15/2} \rightarrow ^2H_{11/2}$  of  $\text{Er}^{3+}$  and  $^7F_0 \rightarrow ^5D_1$  of  $\text{Eu}^{3+}$ .

The luminescent emission spectrum of  $\text{Y}_2\text{O}_3:\text{Er}^{3+}, \text{Eu}^{3+}$  is shown in figure 4(a). Intense narrow lines in the emission spectrum are a result of the  $4f - 4f$  transition. Schematic diagram of  $\text{Er}^{3+}$  and  $\text{Eu}^{3+}$  energy levels and the main transitions are presented in figure 4(b).

The green emission line at 564 nm is the result of the  $^4S_{3/2} \rightarrow ^4I_{15/2}$  transition in  $\text{Er}^{3+}$ . The red emission at 611 nm is the transition  $^5D_0 \rightarrow ^7F_2$  in  $\text{Eu}^{3+}$  and the luminescence line at 661 nm is the result of a transition  $^4F_{9/2} \rightarrow ^4I_{15/2}$  in  $\text{Er}^{3+}$ .

In the luminescence intensity ratio method for temperature measurements we used the intensity ratio of  $\text{Er}^{3+}^4S_{3/2} \rightarrow ^4I_{15/2}$  and  $\text{Eu}^{3+}^5D_0 \rightarrow ^7F_2$  emission lines. Emission spectra as a function of temperature (normalized to the  $\text{Eu}^{3+}$  line at 611 nm) are presented in figure 5(a). These two emission lines have high emission intensities in the whole temperature range from 303 to 573 K. Sharp and strong peaks can eliminate problems of optical noise and black body radiation at high temperatures, so that the emission intensities at line peaks

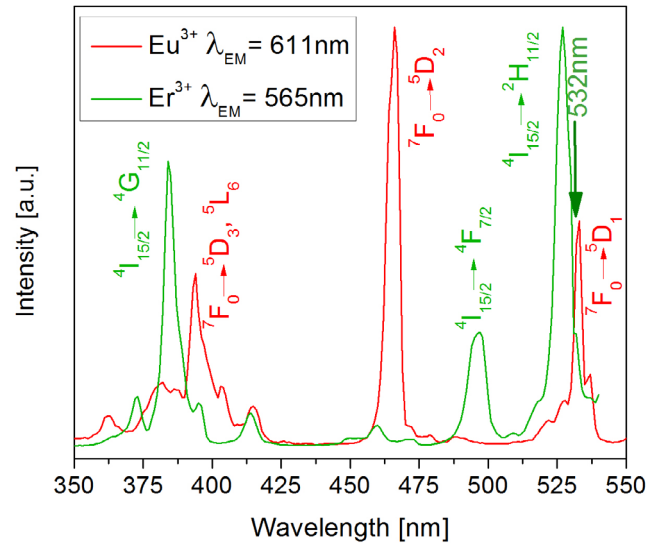


**Figure 3.** Luminescent excitation spectra of  $\text{Y}_2\text{O}_3:\text{Er}^{3+}, \text{Eu}^{3+}$ . The red excitation spectrum is measured at 611 nm ( $\text{Eu}^{3+}$  emission) and green was measured at 565 nm ( $\text{Er}^{3+}$  emission).

are easily measurable. The dependence of  $\text{Er}^{3+}^4S_{3/2} \rightarrow ^4I_{7/2}$  and  $\text{Eu}^{3+}^5D_0 \rightarrow ^7F_2$  emission line intensities in  $\text{Y}_2\text{O}_3:\text{Er}^{3+}, \text{Eu}^{3+}$  as a function of temperature are shown in figure 5(b). The intensity of the  $\text{Eu}^{3+}^5D_0 \rightarrow ^7F_2$  emission line slightly decreases from 300 to 375 K, starting to increase up to 500 K and then decreases once more. In contrast, the intensity of the  $\text{Er}^{3+}^4S_{3/2} \rightarrow ^4I_{15/2}$  emission line was reduced by around seven times in the same temperature interval.

There is a clear distinction between the intensity temperature dependence of the  $\text{Eu}^{3+}^5D_0 \rightarrow ^7F_2$  line in  $\text{Y}_2\text{O}_3:\text{Er}^{3+}, \text{Eu}^{3+}$  compared to  $\text{Y}_2\text{O}_3:\text{Eu}^{3+}$ . This emission line intensity in  $\text{Y}_2\text{O}_3:\text{Eu}^{3+}$  is constantly decreasing in temperature range from 300 K up to 1000 K, which can be seen in the work of Bosze *et al* [30]. The process of energy transfer occurs from  $\text{Er}^{3+}$  ( $^2H_{11/2}, ^4S_{3/2}$ ) to  $\text{Eu}^{3+}$  ( $^5D_1, ^5D_0$ ) in  $\text{Y}_2\text{O}_3:\text{Er}^{3+}, \text{Eu}^{3+}$  due to the fact that there is a small difference between energy levels of  $\text{Er}^{3+}$  and  $\text{Eu}^{3+}$ . This effect leads to the growth of  $^5D_0$  energy level population and the  $\text{Eu}^{3+}$  line intensity increase as a function of temperature. The energy transfer from  $\text{Er}^{3+}$  to  $\text{Eu}^{3+}$  in  $\text{Y}_2\text{O}_3:\text{Er}^{3+}, \text{Eu}^{3+}$  is also presented in the work of Rai *et al* [19].

In addition to this effect, in complex systems with two dopants many other parameters, such as different probabilities of non-radiative transitions in two dopants or different probabilities of the excitation light absorption, can also influence the temperature dependence of the emission intensity ratio. According to Riseberg and Moos [31] a non-radiative process (multi phonon relaxation) is the transition from an excited level to a lower level with the energy being dissipated into phonons. The probability of this non-radiative relaxation depends strongly on the energy gap between the excited level and the energy level beneath them,  $\Delta E$ , and phonon energy,  $\hbar\omega$ . For  $\text{Er}^{3+}$  and  $\text{Eu}^{3+}$  ions in  $\text{Y}_2\text{O}_3$  values of  $\Delta E$  are  $3.07 \cdot 10^3 \text{ cm}^{-1}$  and  $12.49 \cdot 10^3 \text{ cm}^{-1}$ , respectively [2]. The phonon energy is the same for both dopants since they are in the same the  $\text{Y}_2\text{O}_3$  matrix. It can be concluded that the non-radiative processes in  $\text{Er}^{3+}$  ions (with

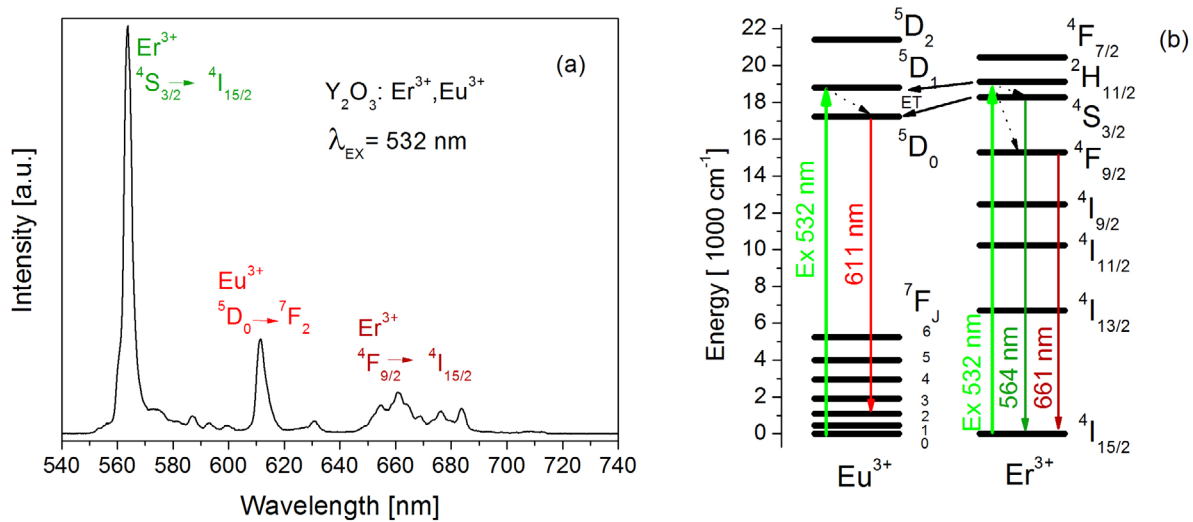


**Figure 4.** (a) Luminescent emission spectrum of  $\text{Y}_2\text{O}_3:\text{Er}^{3+}, \text{Eu}^{3+}$ ; (b) energy levels of  $\text{Er}^{3+}$  and  $\text{Eu}^{3+}$ .

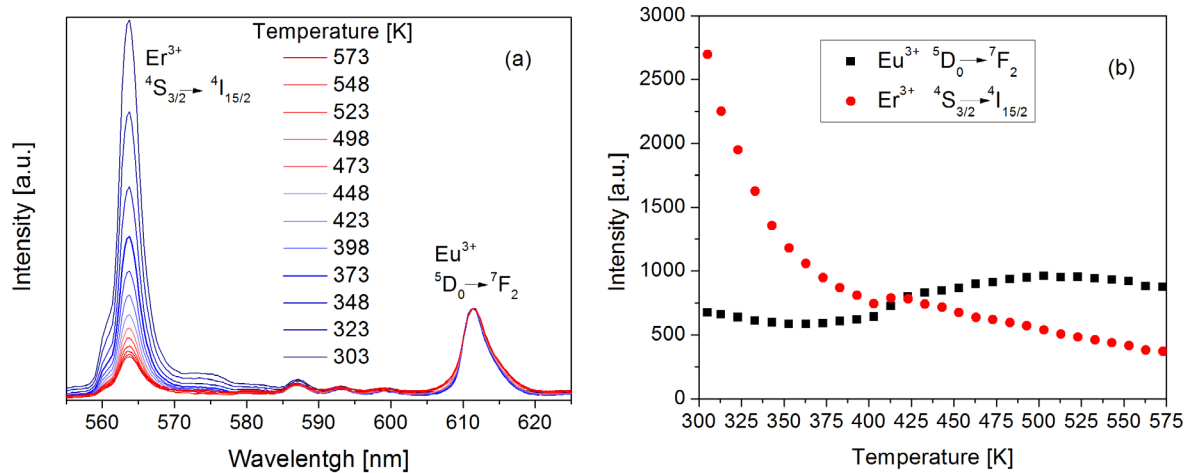


**Figure 5.** (a) Emission spectra as a function of temperature normalized to the  $\text{Eu}^{3+}$  line at 611 nm; (b)  $\text{Y}_2\text{O}_3 \text{Er}^{3+} 4\text{S}_{3/2} \rightarrow 4\text{I}_{15/2}$  and  $\text{Eu}^{3+} 5\text{D}_0 \rightarrow 7\text{F}_2$  emission line intensities as a function of temperature.

smaller  $\Delta E$ , see figure 2(b)) will occur at lower temperatures than in  $\text{Eu}^{3+}$  ions, and this leads to strong temperature changes of luminescence emission of  $\text{Er}^{3+}$  relative to  $\text{Eu}^{3+}$ . Broadening and shift of dopant absorption lines, due to the increase of the temperature, can also influence the emission intensity ratio. The change in the absorption probability, which is a function of temperature, can induce changes in populations of the excited levels. Furthermore, changes in the dominant phonon energy of the matrix, as a result of an increase in temperature, can induce changes in the probabilities of non-radiative processes in the different dopants with different energy  $\Delta E$ .

A small peak in the intensity of emission lines  $\text{Er}^{3+} 4\text{S}_{3/2} \rightarrow 4\text{I}_{15/2}$  and  $\text{Eu}^{3+} 5\text{D}_0 \rightarrow 7\text{F}_2$  at a temperature of 413 K can be seen in figure 5(b). It is caused by some accidental variation in experimental conditions during the measurement (increasing of excitation laser power, motion of the sample or furnace due to the rise of temperature, etc). The intensity ratio method is insensitive to these changes. Using this method, a number of errors arising from fluctuations in

excitation intensity and deviation of optical conditions can be eliminated. In figure 6(a) it can be seen that the measured intensity ratio of  $\text{Er}^{3+} 4\text{S}_{3/2} \rightarrow 4\text{I}_{15/2}$  and  $\text{Eu}^{3+} 5\text{D}_0 \rightarrow 7\text{F}_2$  values are monotonic in the entire temperature range and do not have the deviation from the fitted curve at a temperature of 413 K.

In order to apply the intensity ratio method in thermometry, it is required to calculate a calibration function of each phosphor sample that will be used for temperature measurements. Fitting the measured intensity ratio  $\text{IR} = I_{\text{Er}}/I_{\text{Eu}}$  values was performed by using the empirical function:  $\text{IR} = A + C \cdot e^{-\alpha T}$  [18], where  $T$  is temperature in K, and empirical constants obtained through fitting of measured data are  $A = 0.394$ ,  $C = 398.9$  and  $\alpha = 0.0155 \text{ K}^{-1}$ .

The relative thermal sensitivity of this sensor  $S_R$  is determined using formula:

$$S_R = \left| \frac{1}{\text{IR}} \frac{d\text{IR}}{dT} \right|$$



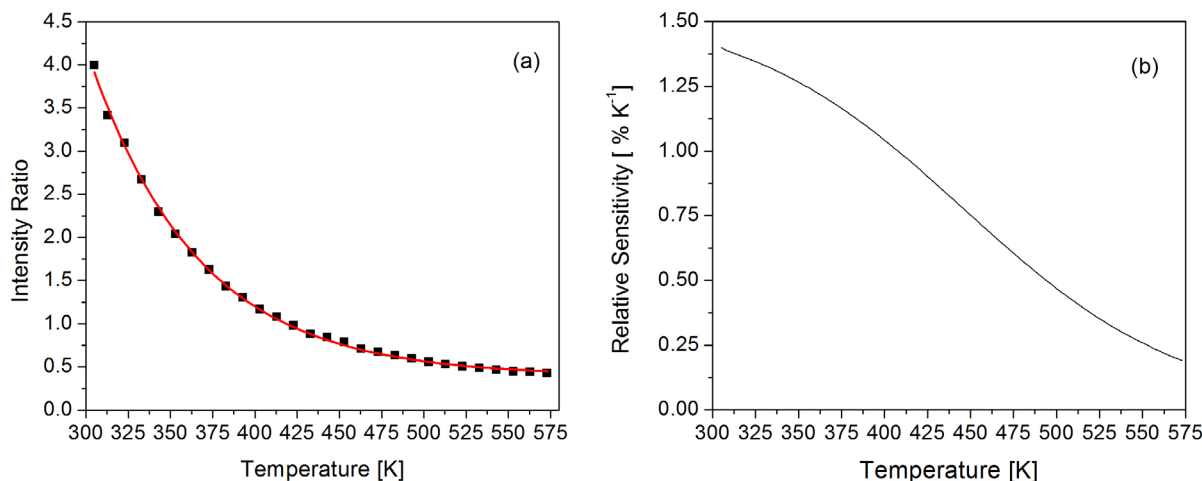


**Figure 6.** (a) The intensity ratio of  $\text{Er}^{3+4}\text{S}_{3/2} \rightarrow ^4\text{I}_{15/2}$  and  $\text{Eu}^{3+5}\text{D}_0 \rightarrow ^7\text{F}_2$  emission lines (black squares) and temperature calibration curve (red line); (b) temperature sensor relative sensitivity at different temperatures.

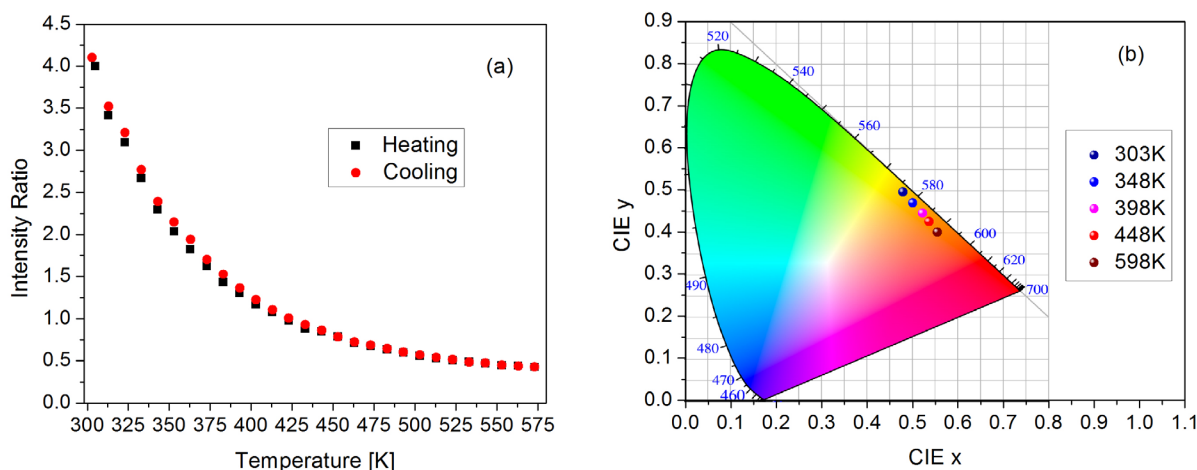


**Figure 7.** (a) Measurement repeatability. Black squares show the results during the heating and the red circles are the results during sample cooling; (b) CIE chromaticity diagram showing the temperature dependence of the  $(x, y)$  color coordinates.

and it has a maximum value of  $1.4\% \text{ K}^{-1}$  at 303 K, and it is shown in figure 6(b). This relative sensitivity is among the highest recorded for inorganic thermographic phosphor for this temperature (see for comparison the comprehensive list of relative sensors sensitivity presented by Brites *et al* [7]).

The important parameter for any measurement is repeatability and as well for materials which can be used for temperature measurement by the luminescence intensity ratio method. The intensity ratio of emission lines of  $\text{Y}_2\text{O}_3:\text{Er}^{3+}, \text{Eu}^{3+}$  ( $\text{Er}^{3+4}\text{S}_{3/2} \rightarrow ^4\text{I}_{15/2}$  and  $\text{Eu}^{3+5}\text{D}_0 \rightarrow ^7\text{F}_2$ ) as a function of temperature is shown in figure 7(a), in processes of the sample cooling and heating. The presented results show a high repeatability and very low hysteresis which is a good characteristic of this material for applicability in temperature measurement.

The resulting spectra at different temperatures were used to calculate the changes in the color of the sample as a function of temperature by the calculus of the Commission Internationale d'Éclairage (CIE)  $(x, y)$  color coordinates (figure 7(b)). In the temperature range of 303–573 K, the color of the sample changes from yellow to orange red.

#### 4. Conclusions

The intensity ratio method was used for  $\text{Er}^{3+}, \text{Eu}^{3+}$  doped  $\text{Y}_2\text{O}_3$  samples in order to examine the potential applicability of this type of phosphor as a temperature sensor. The variation of the emission intensity with increasing temperature is monitored for the main transitions of  $\text{Er}^{3+}$  ions:  $^4\text{S}_{3/2} \rightarrow ^4\text{I}_{15/2}$  and  $\text{Eu}^{3+}$  ions:  $^5\text{D}_0 \rightarrow ^7\text{F}_2$ . Measurements recorded from 303 K up to 573 K show that  $\text{Y}_2\text{O}_3$  doped with 3 at.%  $\text{Er}^{3+}$  and 1 at.%  $\text{Eu}^{3+}$  has the relative sensitivity of  $1.4\% \text{ K}^{-1}$  at 303 K. This material has the ability to fine-tune the emission color as a function of temperature. The accomplished results demonstrate the performance of high sensitivity thermographic phosphors and the fact that the measurements can even be performed with low cost equipment. Furthermore, this thermographic phosphor is a good candidate for biological applications due to the fact that it has high sensitivity at a temperature of 303 K. Besides, it can be prepared in the form of nano and micro particles. We have also taken into account that the wavelength excitation is not in the field of invasive UV radiation. Based on all of the shown characteristics, this thermographic phosphor clearly represents a good candidate for phosphor thermometry.

## Acknowledgments

Authors acknowledge the financial support of the Ministry of Education and Science of the Republic of Serbia (Projects OI171005, OI171038 and III45016).

## References

- [1] Khalid A H and Kontis K 2008 Thermographic phosphors for high temperature measurements: principles, current state of the art and recent applications *Sensors* **8** 5673–44
- [2] Chambers M D and Clarke D R 2009 Doped oxides for high-temperature luminescence and lifetime thermometry *Annu. Rev. Mater. Res.* **39** 325–59
- [3] Allison S W and Gillies G T 1997 Remote thermometry with thermographic phosphors: instrumentation and applications *Rev. Sci. Instrum.* **68** 2615
- [4] Brübach J, Pflitsch C, Dreizler A and Atakan B 2013 On surface temperature measurements with thermographic phosphors: a review *Prog. Energy. Combust. Sci.* **39** 37–60
- [5] Heyes A L, Feist J P, Chen X, Mutasim X and Nicholls J R 2008 Optical nondestructive condition monitoring of thermal barrier coatings *J. Eng. Gas Turbines Power* **130** 61301–8
- [6] Samulski T and Shrivastava P N 1980 Photoluminescent thermometer probes: temperature measurements in microwave fields *Science* **208** 193–4
- [7] Brites C D S, Lima P P, Silva N J O, Millán A, Amaral V S, Palacio F and Carlos L D 2012 Thermometry at the nanoscale *Nanoscale* **4** 4799–829
- [8] Jaque D and Vetrone F 2012 Luminescence nanothermometry *Nanoscale* **4** 4301–26
- [9] Jadhav A P, Pawar A U, Palc U and Kang Y S 2014 Red emitting  $Y_2O_3:Eu^{3+}$  nanophosphors with >80% down conversion efficiency *J. Mater. Chem. C* **2** 496–500
- [10] Blasse G and Grabmaier B C 1994 *Luminescent Materials* (Berlin: Springer)
- [11] Maldiney T et al 2014 The *in vivo* activation of persistent nanophosphors for optical imaging of vascularization, tumours and grafted cells *Nat. Mater.* **13** 418–26
- [12] Lecoq P and Korzhik M 2000 Scintillator developments for high energy physics and medical imaging *IEEE Trans. Nucl. Sci.* **47** 1311–4
- [13] Nikolić M G, Antić Ž, Čulubrk S, Nedeljković J M and Dramićanin M D 2014 Temperature sensing with  $Eu^{3+}$  doped  $TiO_2$  nanoparticles *Sensors Actuators B* **201** 46–50
- [14] Nikolić M G, Al-Juboori A Z, Đorđević V and Dramićanin M D 2013 Temperature luminescence properties of  $Eu^{3+}$ -doped  $Gd_2O_3$  phosphors *Phys. Scr.* **157** 014056
- [15] Lojpur V, Antić Z, Krsmanović R, Medic M, Nikolić M G and Dramićanin M D 2012 Thermographic properties of  $Eu^{3+}$ - and  $Sm^{3+}$ -doped  $Lu_2O_3$  nanophosphor *J. Serb. Chem. Soc.* **77** 1735–46
- [16] Đaćanin Lj R, Dramićanin M D, Lukić-Petrović S R, Petrović D M and Nikolić M G 2013  $Eu^{3+}$  doped  $YNbO_4$  phosphor properties for fluorescence thermometry *Radiat. Meas.* **56** 143–6
- [17] Brites C D S, Lima P P, Silva N J O, Millán A, Amaral V S, Palacio F and Carlos L D 2010 A luminescent molecular thermometer for long-term absolute temperature measurements at the nanoscale *Adv. Mater.* **22** 4499–504
- [18] Ananias D, Brites C D S, Carlos L D and Rocha J 2016 Cryogenic Nanothermometer based on the MIL-103(Tb,Eu) metal–organic framework *Eur. J. Inorg. Chem.* **2016** 1967–71
- [19] Rai V K, Pandey A, and Dey R 2013 Photoluminescence study of  $Y_2O_3:Er^{3+}, Eu^{3+}, Yb^{3+}$  phosphor for lighting and sensing applications *J. Appl. Phys.* **113** 083104–6
- [20] Dey R, Pandey A and Rai V K 2014  $Er^{3+}-Yb^{3+}$  and  $Eu^{3+}-Er^{3+}-Yb^{3+}$  codoped  $Y_2O_3$  phosphors as optical heater *Sensors Actuators B* **190** 512–5
- [21] Ishiwada N, Fujioka S, Ueda T and Yokomori T 2011 Co-doped  $Y_2O_3:Tb^{3+}, Tm^{3+}$  multicolor emitting phosphors for thermometry *Opt. Lett.* **36** 760–2
- [22] Lojpur V, Nikolić M G, Mancić L, Milosević O and Dramićanin M D 2013  $Y_2O_3:Yb, Tm$  and  $Y_2O_3:Yb, Ho$  powders for low-temperature thermometry based on up-conversion fluorescence *Ceram. Int.* **39** 1129–34
- [23] Lojpur V, Nikolić M G, and Dramićanin M D 2014 Luminescence thermometry below room temperature via up-conversion emission of  $Y_2O_3:Yb^{3+}, Er^{3+}$  nanophosphors *J. Appl. Phys.* **115** 203106
- [24] Krsmanović R M, Antić Ž, Bartova B and Dramićanin M D 2010 Characterization of rare-earth doped  $Lu_2O_3$  nanopowders prepared with polymer complex solution synthesis *J. Alloys Compd.* **505** 224–8
- [25] Andrić Ž, Dramićanin M D, Mitrić M, Jokanović V, Bessiere A and Viana B 2008 Polymer complex solution synthesis of  $(Y_xGd_{1-x})_2O_3:Eu^{3+}$  nanopowders *Opt. Mater.* **30** 1023–74
- [26] Krsmanović R M, Andrić Ž, Nikolić M G, Mitrić M and Dramićanin M D 2011 Preparation of  $Y_2O_3:Eu^{3+}$  nanopowders via polymer complex solution method and luminescence properties of the sintered ceramic *Ceram. Int.* **37** 525–31
- [27] Chavez D H, Contreras O E and Hirata G A 2016 Synthesis and upconversion Luminescence of nanoparticles  $Y_2O_3$  and  $Gd_2O_3$  Co-doped with  $Yb^{3+}$  and  $Er^{3+}$  *Nanotechnol. Nanomater.* **67** 1–10
- [28] Das G K and Yang Tan T T 2008 Rare-earth-doped and codoped  $Y_2O_3$  nanomaterials as potential bioimaging probes *J. Phys. Chem. C* **112** 11211–7
- [29] Wang X-d, Wolfbeis O S and Meier R J 2013 Luminescent probes and sensors for temperature *Chem. Soc. Rev.* **42** 7834
- [30] Bosze E J, Hirata G A and McKittrick J 2011 An analysis of  $Y_2O_3:Eu^{3+}$  thin films for thermographic phosphor applications *J. Lumin.* **131** 41–8
- [31] Riseberg L A and Moos H W 1968 Multiphonon orbit-lattice relaxation of excited states of rare-earth ions in crystals *Phys. Rev.* **174** 429–38

# *The Hubbard Model and Piezoresistivity*

**V. Celebonovic & M. G. Nikolic**

**Journal of Low Temperature Physics**

ISSN 0022-2291

Volume 190

Combined 3-4

J Low Temp Phys (2018) 190:191-199

DOI 10.1007/s10909-017-1830-y

Volume 190 • Numbers 3/4 • February 2018

Journal of  
Low Temperature  
Physics

10909 • ISSN 0022-2291  
190(3/4) 101-224 (2018)

 Springer

 Springer

**Your article is protected by copyright and all rights are held exclusively by Springer Science+Business Media, LLC. This e-offprint is for personal use only and shall not be self-archived in electronic repositories. If you wish to self-archive your article, please use the accepted manuscript version for posting on your own website. You may further deposit the accepted manuscript version in any repository, provided it is only made publicly available 12 months after official publication or later and provided acknowledgement is given to the original source of publication and a link is inserted to the published article on Springer's website. The link must be accompanied by the following text: "The final publication is available at [link.springer.com](http://link.springer.com)".**

# The Hubbard Model and Piezoresistivity

V. Celebonovic<sup>1</sup>  · M. G. Nikolic<sup>1</sup>

Received: 9 August 2017 / Accepted: 30 October 2017 / Published online: 7 November 2017  
© Springer Science+Business Media, LLC 2017

**Abstract** Piezoresistivity was discovered in the nineteenth century. Numerous applications of this phenomenon exist nowadays. The aim of the present paper is to explore the possibility of applying the Hubbard model to theoretical work on piezoresistivity. Results are encouraging, in the sense that numerical values of the strain gauge obtained by using the Hubbard model agree with results obtained by other methods. The calculation is simplified by the fact that it uses results for the electrical conductivity of 1D systems previously obtained within the Hubbard model by one of the present authors.

**Keywords** Hubbard model · Electrical conductivity · Piezoresistivity · Strain gauge factor

## 1 Introduction

Piezoresistivity was discovered by Lord Kelvin around the middle of the nineteenth century, in an analysis of the changes of resistivity of underwater telegraph cables [1]. It was reported for the first time in [2] that Si and Ge had a “large” piezoresistive shear coefficient, and a couple of years after that first measurements of the strain gauge factor were taken. This was a “trigger” for various applications of this effect in many

---

This study was financed within the Projects 171005 and 171038 of the Ministry of Education, Science and Technological Development of Serbia.

---

✉ V. Celebonovic  
vladan@ipb.ac.rs

M. G. Nikolic  
nikolic@ipb.ac.rs

<sup>1</sup> LEX Laboratory, Institute of Physics, University of Belgrade, Pregrevica 118, Belgrade 11080, Serbia

kinds of sensors; there have also been some extremely interesting medical applications. Contemporary applications include accelerometers, strain gauges, pressure sensors. For some recent examples see [3–7], and for historical details see [8].

The sensitivity of a sensor based on piezoresistivity is given by

$$G = \frac{-1}{\sigma} \frac{\partial \sigma}{\partial \epsilon} \tag{1}$$

where  $\sigma$  is the conductivity and  $\epsilon$  the strain.

Calculating the value of  $G$  for a real 3D material is a task of considerable complexity. A suitable example is [9]. In the present paper the function  $G$  will be calculated for materials having 1D and rectangular 2D lattices. Knowing the Hamiltonian of a system enables the calculation of its transport properties. One of the methods for such calculations is the so-called memory function (MFA), developed in the 1970s as a consequence of previous work of Kubo. The calculation will be performed by using the Hubbard model (HM).

The remainder of this paper is divided into several sections. The next section contains the main equations of the HM, the memory function method and the resulting expression for the electrical conductivity of a 1D system. The third section is devoted to the derivation of an expression for the function  $G$ . Section 4 contains results of the calculation of  $G$  for 1D and rectangular 2D systems, while Sect. 5 discusses the case of strain-dependent hopping. The final part contains the conclusions.

## 2 Theory

The Hamiltonian of the HM in 1D, expressed in the formalism of second quantization, has the following form

$$H = -w \sum_{l,\sigma} \left( c_{l,\sigma}^+ c_{l+1,\sigma} + c_{l+1,\sigma}^+ c_{l,\sigma} \right) + U \sum_j n_{j,\uparrow} n_{j,\downarrow} \tag{2}$$

where  $w$  denotes the hopping and  $U$  is the interaction energy of a pair of electrons having opposite spins on a lattice site  $j$ . Symbols of the form  $c_{l,\sigma}^+$  denote a creation operator for an electron having spin  $\sigma$  on lattice site  $l$ .  $c_{l+1,\sigma}$  is the annihilation operator for an electron at lattice site  $l + 1$  with spin  $\sigma$ . The current operator is

$$j = -iw \sum_{l,\sigma} \left( c_{l,\sigma}^+ c_{l+1,\sigma} - c_{l+1,\sigma}^+ c_{l,\sigma} \right) \tag{3}$$

The MFA is extensively discussed in the literature. A few examples of such publications are ([10–13]). The crucial equations of the MFA are

$$\begin{aligned} \chi_{AB}(\omega) = & \lll A; B \ggg = \\ & -i \int_0^\infty \exp i\omega t \langle [A(t), B(0)] \rangle dt \end{aligned} \tag{4}$$

and

$$\sigma(z) = i \frac{\omega_p^2}{4\pi z} \left[ 1 - \frac{\chi(z)}{\chi(0)} \right] \tag{5}$$

Expression (4) is a general definition of the linear response of a physical quantity represented by the operator  $A$  to the perturbation by a physical quantity described by an operator  $B$ .  $A(t)$  denotes the Heisenberg representation of the operator  $A$ . Inserting  $A = B = [j, H]$  into Eq. (4) can give the current–current correlation function.

The following symbols have been used:  $j$  is the current operator,  $H$  is the Hamiltonian, and  $\langle\langle \dots \rangle\rangle$  is the mean value of the time-ordered product of operators  $A(t)$  and  $B(t = 0)$ ,  $\sigma$  denotes the electrical conductivity,  $z$  is the complex frequency,  $\omega_p$  is the plasma frequency,  $\chi(z)$  is the frequency-dependent susceptibility, and  $\chi(0)$  is the static susceptibility. The time-ordered product of operators is defined in such a way that every operator in it has later operators to the left and earlier operators to the right (see, for example, [14]).

As  $z$  is the complex frequency, it can be expressed as  $z = z_1 + iz_2 = z_1 + i\alpha z_1$ , where  $\alpha > 0$ . The complex conductivity  $\sigma(z)$  can be separated into a real  $\sigma_R$  and imaginary components  $\sigma_I$ . It can be shown that

$$\sigma_R = \frac{\omega_p^2 \chi_I}{4\pi z_1 \chi_0} \tag{6}$$

and

$$\sigma_I = \frac{\omega_p^2}{4\pi z_1} \left( 1 - \frac{\chi_R}{\chi_0} \right) \tag{7}$$

The final result for the electrical conductivity is given by [12]

$$\sigma_R(\omega_0) = (1/2\chi_0) \left( \omega_p^2/\pi \right) \left[ \omega_0^2 - (bw)^2 \right]^{-1} (Uw/N^2)^2 \times S \tag{8}$$

and the symbol  $S$  denotes the following function

$$\begin{aligned} S = & 42.49916 \times (1 + \exp(\beta(-\mu - 2w)))^{-2} \\ & + 78.2557 \times (1 + \exp(\beta(-\mu + 2w \cos(1 + \pi))))^{-2} \\ & + (bw/(\omega_0 + bw)) \times (4.53316 \\ & \times (1 + \exp(\beta(-\mu - 2w)))^{-2} \\ & + 24.6448(1 + \exp(\beta(-\mu + 2w \cos(1 + \pi))))^{-2} \end{aligned} \tag{9}$$

The symbol  $\mu$  denotes the chemical potential of the electron gas on a 1D lattice [12]

$$\mu = \frac{(\beta w)^6 (ns - 1) |w|}{1.1029 + .1694(\beta w)^2 + .0654(\beta w)^4} \tag{10}$$

### 3 The Strain Gauge Factor

In order to calculate the strain gauge factor  $G$ , as defined by Eq. (1), one needs explicit expressions for the electrical conductivity and the strain, as well as some assumptions concerning the dependence of the hopping energy on the strain. As a first approximation, it will be assumed in this section that the hopping is strain independent. A later part of the paper will explore the influence of the strain dependence of the hopping on  $G$ . The strain  $\epsilon$  is defined as

$$s_\epsilon = s_0(1 - \epsilon) \tag{11}$$

where  $s_0$  denotes the value of the lattice constant at zero strain. Inserting Eq. (11) into Eqs. (8)–(10) and then using Eq. (1) one gets the result for the strain gauge factor. The expression thus obtained is too long to be written here. Expanding the sums and products, and taking only the first term, one finally gets the following approximate result for  $G$ .

$$G \cong \frac{2 \exp[\beta(-2w - \mu)]ns_0w^7\beta^8}{(1 + \exp[\beta(-2w - \mu)])(1.1029 + \dots)} + \dots \tag{12}$$

and  $\beta$  denotes the inverse temperature. Generalizing, the function  $G$  can be expressed as a power series in strain  $\epsilon$ :

$$G = \sum_{i=0}^K G_i \epsilon^i \tag{13}$$

where  $K$  denotes the number of terms taken into account. Taking as an example  $K = 3$ , it follows that the coefficient  $G_0$  is given by

$$G_0 = \frac{2ns_0w^6\beta^7|w|\exp[\beta(-2w + \dots)]}{(1 + \exp[\beta(-2w + \mu)])(1.1029 + \dots)} \tag{14}$$

This implies that apart from the strain  $\epsilon$  the function  $G$  depends on various material parameters.

### 4 Examples of Applications

In this section, the expression for  $G$  derived in the preceding part of this paper will be applied for various values of material parameters. The parameters will have the same values as in [12], but for convenience they are given here. For the meanings of various symbols see [12]. Therefore,  $b = -1.83879$ ;  $s_0 = 1$ ;  $N = 150$ ;  $U = 4w$ ;  $\omega_P = 12w$ ;  $\omega_0 = 2.8w$ ;  $\chi_0 = 1/3$ . The band filling  $n$ , electronic hopping energy  $w$  and the temperature  $T$  were assigned arbitrary but physically realistic values. All the figures were normalized to 1 at the same point:  $n = 1.1$ ;  $\epsilon = 0$ ;  $T = 116K$ .

Note in Fig. 1 that an increase of the strain from  $\epsilon = 0.1$  to  $\epsilon = 0.2$  leads to a drastic increase of  $G$ . Increasing the temperature and keeping  $n$  and  $t$  constant gives drastically smaller values of  $G$  (Fig. 2). Figure 3 shows the behavior of  $G$  but for a system at a higher temperature. All the other parameters are kept constant.



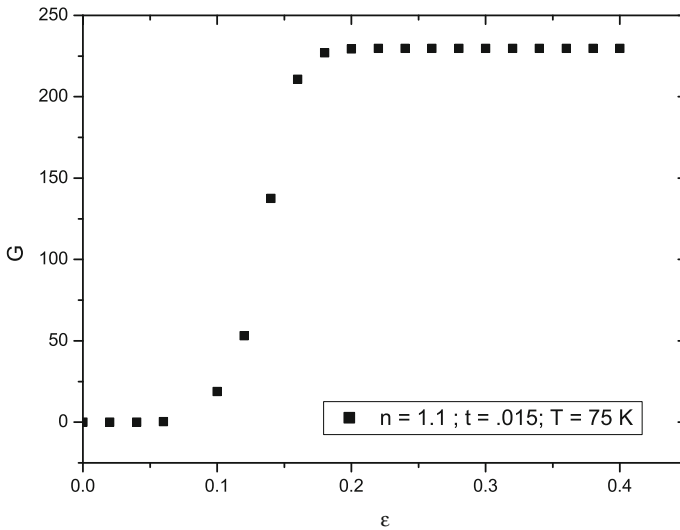


**Fig. 1** Values of  $G$  for  $T = 75$  K

Slightly changing the parameters of the problem and repeating the calculation for two values of the temperature gives Fig. 4. All the figures were normalized to 1 at the same point:  $n = 1.1$ ;  $\epsilon = 0$ ;  $T = 116K$ .

### 4.1 The Simplest 2D Case

The calculations discussed so far refer to the 1D case. In the case of a 2D rectangular lattice, the expression for  $G$  can be derived in an extremely simple way. As shown in [12], the conductivity of a rectangular 2D lattice is given by

$$\sigma^2 = \sigma_x^2 + \sigma_y^2 \tag{15}$$

where the suffixes  $x$  and  $y$  denote the two lattice axes. In the simplest case  $\sigma_y = \sigma_x$ , which means that  $\sigma = \sigma_x\sqrt{2}$ . Applying Eq. (1) leads to the following result for a rectangular 2D lattice:

$$G_{2D} = -\frac{1}{\sigma_x} \frac{\partial \sigma_x}{\partial \epsilon} = G_x \tag{16}$$

The same result is obtained in the case  $\sigma_y = \alpha \sigma_x$ , where  $\alpha$  is a real number.

### 5 The Strain Dependence of the Hopping

All the equations concerning the electrical conductivity of the Hubbard model contain the hopping energy  $t$ , which depends on the overlap of the electronic wave functions on adjacent nodes of the crystal lattice. Physical intuition dictates that the value of  $t$  decreases with the stretching of the lattice, that is, when the strain  $\epsilon$  is positive. A

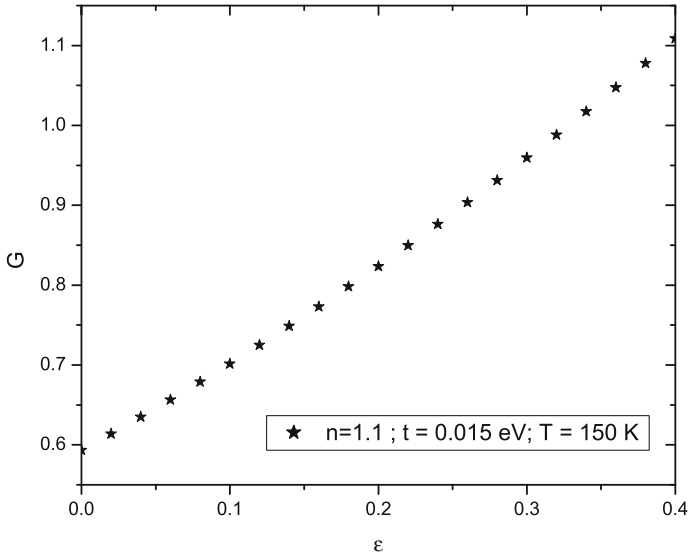


**Fig. 2** Values of  $G$  for  $T = 150$  K

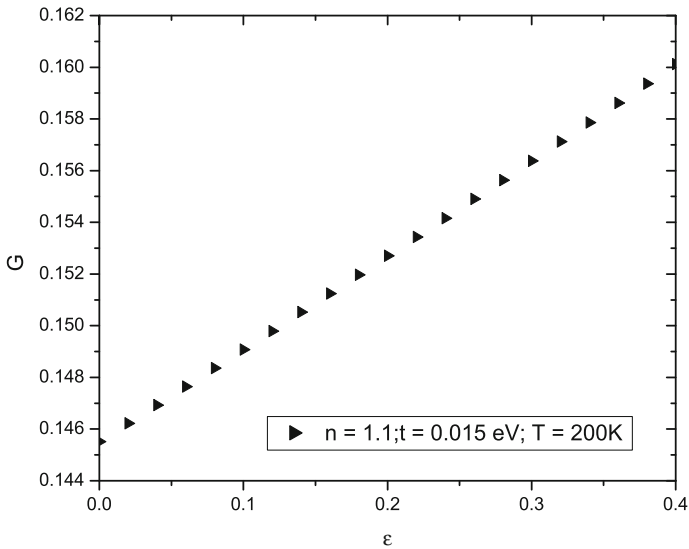


**Fig. 3** Values of  $G$  for  $T = 200$  K

complete quantum-mechanical expression for the distance dependence of the hopping can be found, for example, in Hubbard's second paper [15]. Performing such a calculation would be prohibitively complicated for this paper. As discussed to some extent in [16] using the standard quantum-mechanical form for the overlap integral and for simplicity retaining only terms of first order in  $\epsilon$ , the strain dependence of the hopping

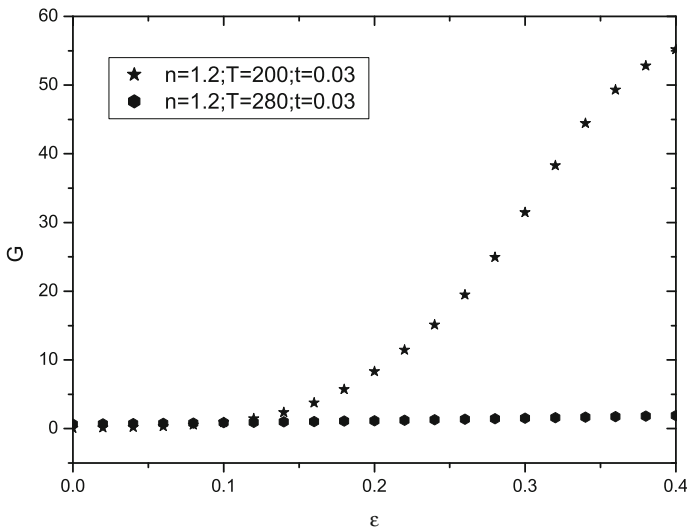


Fig. 4 Values of  $G$  for  $T = 200$  K and  $T = 280$  K,  $n = 1.2$ ,  $t = 0.03$

in the case of lattice stretching can be expressed as

$$t \cong 0.86t_0(1 - 0.286\epsilon) \tag{17}$$

where  $t_0$  denotes the hopping energy when the strain is zero. Figures 5 and 6 show values of  $G$  calculated for the band filling of  $n = 1.1$ , the hopping energy  $t_0 = 0.015$  and two values of the temperature  $T$ . The values of all the constants are the same as in Sect. 4, as is the point at which the curves were normalized to 1.

## 6 Discussion and Conclusions

Several conclusions can be drawn from the calculation presented in this paper. A bibliographical search performed in the middle of September 2017 on the Web site <http://scholar.google.com/> with the keywords “Hubbard model and piezoresistivity” gave zero result. A partial explanation of this can be found in the fact that the electrical conductivity of a 1D Hubbard model has been calculated within the memory function approach only relatively recently [12]. This implies that the present paper is the first attempt of using the Hubbard model in work on piezoresistivity.

Examples of values of the function  $G$  obtained for a set of values of the input parameters are shown in the figures. Figure 1 shows that the highest value of  $G$  obtained for the indicated values of the parameters is around 250. Results for  $G$  obtained in [9] are somewhat higher and go up to  $G$  1000. A similar comparison could be made with [17]. It can be concluded that the order of magnitude similarity between results of the present paper and those in [9, 17] has been achieved. A closer agreement could certainly be obtained by varying the parameters taken into account in the present paper. Comparing Figs. 1 and 5 illustrates the influence of the strain dependence of

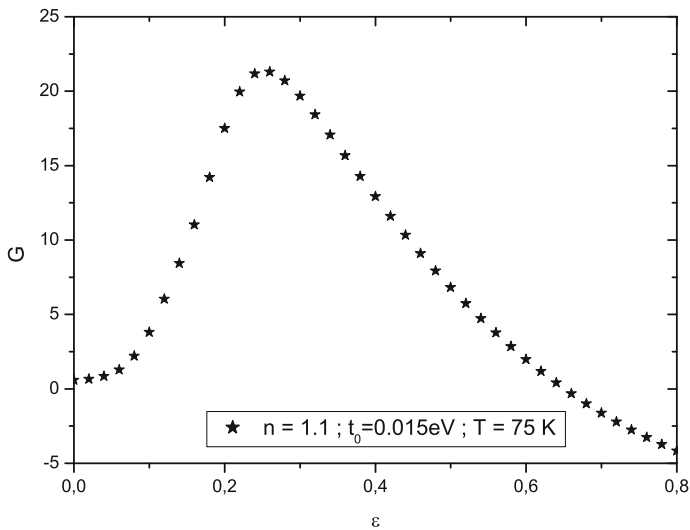


**Fig. 5** Values of  $G$  for  $T = 75$  K,  $n = 1.1$ ,  $t_0 = 0.015$

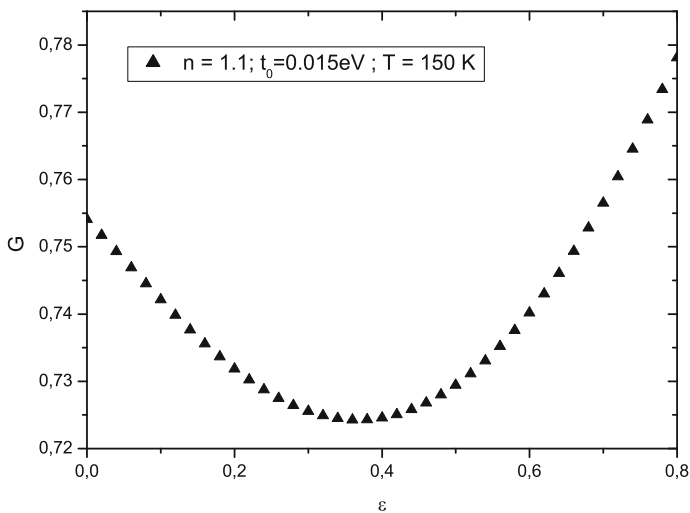


**Fig. 6** Values of  $G$  for  $T = 150$  K,  $n = 1.1$ ,  $t_0 = 0.015$

the hopping  $t$  on the strain  $\epsilon$ . Clearly, for  $\epsilon \leq 0.3$  the trend of  $G$  on both figures is the same, but the numerical values of  $G$  are smaller in Fig. 5. This shows that the dependence of  $t$  on the strain influences the function  $G$ . It would be interesting to repeat the same calculation but with more terms taken into account in  $t(\epsilon)$ .

Another interesting result is the fact that the shape of the function  $G(\epsilon)$  is temperature dependent. A limited literature search shows that this is in qualitative agreement with existing results. Examples of results on this aspect are [18, 19]. There is however a difference of possible importance between this paper and [18, 19]. That is the fact that

in the present paper we have obtained a change of sign of the derivative  $\partial G/\partial\epsilon$  on the curves  $G(\epsilon)$  at a fixed temperature, while the experimental curves do not show such a point. For example, a material called *modco*, which is a N–Cr alloy, has a negative temperature dependence of  $G$  [19]. It will be attempted to explore the origin of this point in the future.

Purely mathematically, equations used in the present work are not very complicated and can be used analytically, which is a clear advantage. However, the whole approach is limited to 1D and 2D systems, while standard considerations of piezoresistivity do not have such a limitation. This points to the region of possible applicability of this approach, and these are high-temperature superconductors and organic conductors.

The strain gauge factor  $G$  calculated here characterizes the sensitivity of various sensors. The results obtained can be used in two ways. One can choose the parameters of the system (i.e., some material) calculate  $G$  and perhaps vary the parameters until a more satisfactory  $G$  is found. The other possibility is to fix the maximal value of the strain  $\epsilon$  for a given material and then calculate the corresponding value of  $G$ . Details will be discussed in the future.

**Acknowledgements** The authors are grateful to the referee for useful comments on a previous version of this manuscript.

#### Compliance with Ethical Standards

**Conflict of interest** The authors declare that they have no conflict of interest.

## References

1. W. Thomson, Proc. R. Soc. Lond. **8**, 550 (1856)
2. C.S. Smith, Phys. Rev. **94**, 42 (1954)
3. C.H. Bruot, J.L. Palma, L. Xiang et al., Nat. Commun. **6**, 1 (2015)
4. J. Grottrup, S. Kaps, J. Carstensen et al., Phys. Status Solidi **A213**, 2208 (2016)
5. D. Jarwala, T.J. Marks, M.C. Hersam, Nat. Mater. **16**, 170 (2017)
6. J. Park, M. Kim, Y. Lee et al., Sci. Adv. **1**, e1500661 (2015)
7. P. Meiser, M.R. Koblischka, U. Hartmann, Meas. Sci. Technol. **26**, 085903 (2015)
8. A.A. Barlian, W.T. Park, J.R. Mallon et al., Proc. IEEE **97**, 513 (2009)
9. F. Murphy-Armando, S. Fahy, Phys. Rev. B **86**, 035205 (2012)
10. W. Götze, P. Wölfle, Phys. Rev. B **6**, 1228 (1971)
11. A. Lucas, S. Sachdev, Phys. Rev. B **91**, 195122 (2015)
12. V. Celebonovic, in *Advanced 2D Materials*, ed. by A. Tiwari, A. Syvajarvi (Scrivener Publishing LLC, Salem, MA, 2016), p. 115
13. P. Bhalla, N. Das, N. Singh, Phys. Lett. **A380**, 2000 (2016)
14. D.N. Zubarev, Sov. Phys. Uspekhi **3**, 320 (1960)
15. J. Hubbard, Proc. R. Soc. **A277**, 237 (1964)
16. V. Celebonovic, J. Phys. Conf. Ser. **558**, 012006 (2014)
17. P. Neuzil, C.C. Wong, J. Reboud, Nano Lett. **10**, 1248 (2010)
18. P. Schmid, C. Zarfl, G. Balogh, U. Schmid, Proc. Eng. **87**, 172 (2014)
19. [www.hbm.com](http://www.hbm.com) This is the web-site of HBM industry in Darmstadt. Accessed 3 Nov 2017

## Some calculational improvements in applying the Hubbard model to nanomaterials

This content has been downloaded from IOPscience. Please scroll down to see the full text.

2017 J. Phys.: Conf. Ser. 794 012008

(<http://iopscience.iop.org/1742-6596/794/1/012008>)

View [the table of contents for this issue](#), or go to the [journal homepage](#) for more

Download details:

IP Address: 147.91.1.45

This content was downloaded on 24/02/2017 at 12:12

Please note that [terms and conditions apply](#).

You may also be interested in:

[Charge instabilities of the two-dimensional Hubbard model with attractive nearest neighbour interaction](#)

Raymond Frésard, Kevin Steffen and Thilo Kopp

[Negativity in the Extended Hubbard Model under External Magnetic Field](#)

Yang Zhen and Ning Wen-Qiang

[Fermionic Concurrence in the Extended Hubbard Model](#)

Deng Shu-Sa and Gu Shi-Jian

[Nanomaterials in Food - Current and Future Applications and Regulatory Aspects](#)

K Aschberger, S Gottardo, V Amenta et al.

[Nanomaterials in construction and demolition - how can we assess the risk if we don't know where they are?](#)

Wendy Jones, Alistair Gibb, Chris Goodier et al.

[Algebraic Bethe ansatz for integrable extended Hubbard models](#)

Anthony J Bracken, Xiang-Yu Ge, Mark D Gould et al.

[Quantum fluctuations in the one dimensional doped Hubbard model](#)

Norikazu Tomita

[Physics of the Hubbard model and high temperature superconductivity](#)

T Yanagisawa

[Algebraic Bethe ansatz for integrable one-dimensional extended Hubbard models](#)

Xiang-Yu Ge and Mark D Gould

# Some calculational improvements in applying the Hubbard model to nanomaterials

Vladan Celebonovic

Institute of Physics, University of Belgrade, Pregrevica 118, 11080 Belgrade, Serbia

E-mail: vladan@ipb.ac.rs

**Abstract.** John Hubbard proposed "his model" ( $HM$ ) nearly sixty years ago, and one could be tempted to expect that everything (or almost so) about it is well known. Quite to the contrary, the  $HM$  is still arising interest and its applicability seems to be rising. The aim of this paper is to discuss several examples of new or already existing but improved results concerning the 2D  $HM$  and its applicability to nanomaterials. The following issues will be discussed: increasing the number of terms in various expressions used in calculating the conductivity; introducing the strain in these expressions (which is important for experiments under high pressure); defining the pressure in a 2D system and calculating the reflectivity but taking into account the imaginary part of the conductivity.

## 1. Introduction

Towards the middle of the last century, one of the outstanding problems of condensed matter physics was the metal to insulator transition ( $MI$ ). John Hubbard tried to contribute to finding an explanation of the  $MI$  transition by proposing what later became known as the Hubbard model -  $HM$  [1]. In spite of the time elapsed since Hubbard's proposal, the  $HM$  is still attracting considerable interest.

The publication of the  $HM$  greatly helped launch the study of correlated electron systems. There exists a semi-documented detail, illustrating this point: Mr. Hubbard was sitting and reading a book on many body theory, when his mother in law passed by and asked him what was the book about. To which Hubbard replied "A murder mystery" [2].

It is common knowledge that the behavior of a physical system is determined by its Hamiltonian  $H$  from which all the thermodynamical functions can be derived. The Hamiltonian of the  $HM$  is *apparently* simple. It contains only two terms, one describing the hopping of electrons within the lattice, and the other the interactions of a pair of electrons with opposite spins on a lattice node. The equations are available in the literature, for example [3]. The fact that the  $HM$  is only *apparently* simple becomes clearly visible when attempting to solve it. The  $HM$  was solved in the 1D case [4], while work on solving the 2D case is ongoing within the Density matrix renormalisation group (DMRG) approach [5]. This kind of work is of course extremely interesting from the point of view of mathematical physics, but the obvious question is the applicability of 1D and 2D  $HM$  in material science.

In the years around 1980 and for some time after it was thought that the so called Bechgaard salts were materials which could be described by the 1D  $HM$  and that they were the simplest cases of strongly correlated electron systems. Applying the  $HM$  to these materials gave results



agreeing with experiments, but they have not been as helpful as expected in understanding the high  $T_c$  materials. See, for example, [6].

Nanomaterials in  $2D$  present a much wider field of possibilities for the application of the  $HM$ . To name just a few examples, these include organic electronics [7], stretchable electronic materials [8], photothermal cancer therapy [9].

There exist numerous publications on various aspects of the  $HM$ , including some by the present author [10]. What is the aim of another paper on the  $HM$ ? The main aim of the present paper is improving the results obtained in previous papers. In practical terms, this means increasing the number of terms taken into account in various developments into series, and taking into account the fact that the imaginary conductivity is different from zero. It will be attempted to introduce a suitable definition of pressure in  $2D$  systems. In that respect, it will be a distinct improvement over previous results. A detailed comparison of the experimental results with the predictions of these "improved" calculations will be performed in the future.

### 1.1. The method

The calculations to be discussed in the remainder of this paper were performed using the so called *memory function* method. It uses the idea, known in statistical mechanics, that knowledge of the Hamiltonian of a system gives the possibility of calculating its electrical conductivity. For a recent review see, for example, [11]. The essential equations of the method are

$$\chi_{AB}(\omega) = \langle\langle A; B \rangle\rangle = -i \int_0^\infty \exp i\omega t \langle [A(t), B(0)] \rangle dt \quad (1)$$

where  $A = B = [j, H]$ ,  $j$  denotes the current operator,  $H$  the Hamiltonian and

$$\sigma(\omega) = i \frac{\omega_P^2}{4\pi z} \left[ 1 - \frac{\chi(z)}{\chi(0)} \right] \quad (2)$$

where  $\sigma$  denotes the electrical conductivity,  $z$  is the complex frequency,  $\omega_P$  is the plasma frequency,  $\chi(\omega)$  is the frequency dependent susceptibility and  $\chi(0)$  the static susceptibility. As  $z$  is the complex frequency, it can be expressed as  $z = z_1 + iz_2 = z_1 + i\alpha z_1$ , where  $\alpha > 0$ . It can be shown that

$$\sigma_R = \frac{\omega_P^2 \chi_I}{4\pi z_1 \chi_0} \quad (3)$$

and

$$\sigma_I = \frac{\omega_P^2}{4\pi z_1} \left( 1 - \frac{\chi_R}{\chi_0} \right) \quad (4)$$

## 2. Calculation of the electrical conductivity

### 2.1. Existing results

The Hamiltonian of the  $HM$  in  $1D$ , expressed in the formalism of second quantisation, has the following form

$$H = -t \sum_{l,\sigma} (c_{l,\sigma}^+ c_{l+1,\sigma} + c_{l+1,\sigma}^+ c_{l,\sigma}) + U \sum_j n_{j,\uparrow} n_{j,\downarrow} \quad (5)$$

where all the symbols have their standard meanings, and the current operator is

$$j = -it \sum_{l,\sigma} (c_{l,\sigma}^+ c_{l+1,\sigma} - c_{l+1,\sigma}^+ c_{l,\sigma}) \quad (6)$$



Using these two expressions it becomes possible to calculate the commutators  $A = B = [j, H]$ , to take into account their time dependence and obtain an expression for the current-current correlation function. All these steps are discussed in [12], and the final result is

$$\begin{aligned} \chi(z) = \sum_{p,g,k,q} & (32i(1/[(1 + \exp[\beta(-\mu - 2t \cos[g])])(1 + \exp[\beta(-\mu - 2t \cos[k])])]) - \\ & -1/[(1 + \exp[\beta(-\mu - 2t \cos[p])])(1 + \exp[\beta(-\mu - 2t \cos[q])])]) \times \\ & (Ut)^2(\alpha z_1 + i(z_1 + 2t(\cos[q] + \cos[p] - \cos[g] - \cos[k]))) \times \\ & (\cos(p + g)/2)(\cos((q + k)/2)(\cosh(g - p) - 1)/ \\ & (N^4((\alpha z_1^2 + (z_1 + 2t(\cos(q) + \cos(p) - \cos(g) - \cos(k))))^2)) \end{aligned} \tag{7}$$

The symbol  $N$  denotes the number of lattice sites,  $\mu$  is the chemical potential and the summations are limited to the first Brioullin zone. The chemical potential  $\mu$  of the electron gas on a  $1D$  lattice is given by [13]

$$\mu = \frac{(\beta t)^6(na - 1)|t|}{1.1029 + 0.1694(\beta t)^2 + 0.0654(\beta t)^4} \tag{8}$$

where  $\beta$  denotes the inverse temperature,  $a$  the lattice constant and  $n$  is the band filling. Summation of eq.(5) taking into account the smallest possible number of terms has been published in [12]. The result was an expression for the electrical conductivity of a  $1D$  system of correlated electrons, which was applied to the Bechgaard salts, and the results obtained were in reasonable agreement with experiments.

The purely mathematical aim of the present calculation is to increase the number of terms taken into account in eq.(7),and in the subsequent calculation of the electrical conductivity. On the physical side, it will be attempted to take into account the dependence of the conductivity on the strain. This result will have applications in studies of nano materials under high external pressure.

### 2.2. New results for the conductivity

The starting point for this calculation is the summation in eq.(7). In order to take into account the influence of the external pressure (that is, the variability of  $a$ ),one has at first to insert  $a > 1$  in eq.(7), and after that introduce a change of variables in this expression. This has to be of the form  $k \rightarrow x/a$ ;  $g \rightarrow y/a$ ;  $p \rightarrow r/a$ ;  $q \rightarrow w/a$ . Introducing all these changes in eq.(7), and summing over the variables  $(k, y, r, w) \in (-\pi, \pi)$ ,one gets the following expression for the susceptibility

$$\begin{aligned} \chi \approx & (32i(\frac{1}{(1 + \exp[\beta(2t - \mu)](1 + \exp(\beta \ll 1 \gg)))} - \\ & \frac{1}{(1 + \exp[\beta \ll 1 \gg])(1 + \exp(\beta \ll 1 \gg \ll 1 \gg))})(tU)^2 \\ & (\alpha z_1 + i(z_1 + 2t(\cos[1] - \cos[2]))) \cos[\frac{1}{2}(\frac{1 - \pi}{a}) + (\frac{2 - \pi}{a})a] \\ & (-1 + \cosh[(\frac{1 - \pi}{a}) + (\frac{2 - \pi}{a})a])/(N^4(z_1^2\alpha^2 + (z_1 + 2t(\cos[1] - \cos[2]))^2)) + \\ & \frac{32i \ll 6 \gg (-1 + \cosh(\frac{\ll 1 \gg}{a}) - \ll 1 \gg)a}{N^4((z_1\alpha)^2 + (z_1 + \ll 1 \gg))^2}) + \ll 3736 \gg \end{aligned} \tag{9}$$

Numbers in parenthesis  $\ll .. \gg$  denote the number of terms omitted. This long expression for  $\chi$  is impractical in any real calculation.

An applicable expression can be obtained by a relatively simple procedure. Multiply out the products and powers in eq.(9), and express the result as a sum. This is a well defined operation, the end result of which is a huge sum of more than 30000 terms, which is far from applicable.

However, take the first 10 terms of this huge sum, expand it and take only the real part of the frequency into account (as done in [12] but for a small number of terms). One thus gets an expression for the real part of the susceptibility of a 1D HM. So, what is the improvement of this result compared to [12]? The number of terms taken into account in various developments into series has been doubled. The result for  $\chi_R$ , taking into account only the first 7 terms is

$$\begin{aligned} \chi_R \cong & \frac{192 \exp[3\beta\mu + 2\beta t] t^3 U^2 \cos[1/2]}{(\exp[\beta\mu] + \exp[2\beta t])^2} \times \frac{1}{N^4(\omega + 4t(\sin[1/2])^2)^2} \\ & \times \frac{1}{(\exp[\beta\mu] + \exp[2\beta t \cos[1]])^2} + \frac{128 \exp[3\beta\mu + 2\beta t] (tU)^2 \omega \cos[1/2]}{(\exp[\beta\mu] + \exp[2\beta t])^2} \\ & \frac{1}{N^4(\omega + 4t(\sin[1/2])^2)^2} + \times \frac{1}{(\exp[\beta\mu] + \exp[2\beta t \cos[1]])^2} \end{aligned} \quad (10)$$

Inserting eq.(10) into expression (4) one can obtain the imaginary part of the electrical conductivity. Using the Kramers-Kronig relations [12],[14] it becomes possible to determine the imaginary part of the susceptibility as the following integral .

$$\chi_I(\omega_0) = -2 \frac{\omega_0}{\pi} P \int_0^\infty \frac{\chi_R(\omega) d\omega}{(\omega^2 - \omega_0^2)} \quad (11)$$

where  $P$  is the principal value of the integral. The final result for the electrical conductivity of a 1D HM is

$$\begin{aligned} \sigma_R \cong & \frac{\omega_P^2}{4\pi\omega\chi_0} \times \left[ \frac{1536 \exp[2t\beta + 2\beta\mu] t^4 U^2 \omega_0^3 \sin[1/2] \sin[2]}{(\exp[2t\beta] + \exp[\mu\beta])} \right] \\ & \times \frac{1}{N^4\pi} \times \frac{1}{(\exp[2t\beta] + \exp[\beta\mu])} \times \frac{1}{(\omega_0^2 - 16t^2(\sin[1/2])^4)^4} + \dots \end{aligned} \quad (12)$$

The advantage of this expression, compared to the one previously presented in [12] is in the increased number of terms taken into account in various developments into series. This should allow a more precise comparison with experimental data on the conductivity.

A more complicated case is the 2D lattice, the simplest of which is a square lattice of side length  $a$  which can be treated as an extension of these results. If the lattice sides are denoted by  $x$  and  $y$ , the electric current flowing through such a system can be expressed as

$$\vec{j} = j_x \vec{e}_x + j_y \vec{e}_y \quad (13)$$

where  $\vec{e}_x$  and  $\vec{e}_y$  are unitary vectors of the two lattice axes. The total current is given by

$$j^2 = j_x^2 + j_y^2 \quad (14)$$

By definition  $j = \sigma E$  where  $\sigma$  is the electrical conductivity and  $E$  the electric field, and assuming that  $E_x = E_y = E$ , it finally follows that

$$\sigma_{2D}^2 = \sigma_x^2 + \sigma_y^2 \quad (15)$$

The conductivities along the two axes are assumed to be mutually independent.

### 3. Compressing and stretching a material

The calculation of the electrical conductivity of the HM discussed in the preceding section refers to standard pressure. However, in nature, applications and various experiments, situations occur in which a material is subdued to variable pressure. The obvious effect which increased pressure has on a material is a decrease of its characteristic dimensions and of all the characteristics of the material which depend on it. Therefore the question is how can one take into account the influence of external pressure on the conductivity of the HM. The consequences of stretching on the conductivity of a material, within the HM, have been discussed to some extent in [3].

#### 3.1. The 1D HM

Mathematically speaking, in the case of a 1D material, the function characterizing the influence of high pressure on the conductivity would be the ratio

$$\frac{\partial\sigma}{\partial a} \quad (16)$$

where  $\sigma$  is the conductivity and  $a$  the lattice constant. The influence of external pressure on a material is characterized by the strain  $\epsilon$ . The strain applied to an object of initial length  $l_0$  so that it achieves length  $l < l_0$  is defined by  $\epsilon = (l_0 - l)/l_0$ . Therefore, eq.(16) can be transformed in the form

$$\frac{\partial\sigma}{\partial a} = \frac{\partial\sigma}{\partial\epsilon} \left(\frac{\partial a}{\partial\epsilon}\right)^{-1} \quad (17)$$

The conductivity depends on the strain only indirectly, through the chemical potential, so that

$$\frac{\partial\sigma}{\partial a} = \frac{\partial\sigma}{\partial\epsilon} \left(\frac{\partial a}{\partial\epsilon}\right)^{-1} = \frac{\partial\sigma}{\partial\mu} \frac{\partial\mu}{\partial\epsilon} \left(\frac{\partial a}{\partial\epsilon}\right)^{-1} \quad (18)$$

Using expression (8) for the chemical potential and the definition of the strain, it turns out that the product  $(\partial\mu/\partial\epsilon)(\partial\epsilon/\partial a)$  does not depend on  $a$ , which means that it does not depend on external pressure. However, the conductivity itself depends (among other factors) on the external pressure. It can be shown, performing some algebra on eq.(12), that

$$\frac{\partial\sigma}{\partial\mu} \cong \frac{1152 \exp[2\beta(t + \mu)] t^8 U^2 \beta \omega_0 \omega_P^2 \dots}{N^4 \pi^2 \chi_0 \omega (\exp[2\beta t] + \exp[\beta\mu])^2 \dots} \quad (19)$$

Inserting eqs.(8) and (19) in full form into eq.(18), one could obtain an explicit expression for the strain dependence of the conductivity.

#### 3.2. The simplest 2D case

A more complex, and more interesting case is the 2D HM. The simplest possible case of a 2D lattice is a rectangular lattice, with sides of length  $a$  and  $b$ . If the external pressure is acting within the plane of the lattice, its effect will be to reduce the surface of the elementary lattice cell. Denoting this surface by  $S$ , it follows that the influence of external pressure on the conductivity will be characterized by the derivative  $\partial\sigma/\partial S$ .

Changes of the dimensions of the lattice cell under pressure enter the calculation through the change of its sides. In the case of a rectangular lattice, the surface of the elementary lattice cell is given by

$$S = ab \quad (20)$$

As  $a = a_0(1 - \epsilon)$  and  $b = b_0(1 - \epsilon)$ , where  $\epsilon$  is the strain, it follows that

$$S = S_0(1 - \epsilon)^2 \quad (21)$$

It follows that

$$\frac{\partial \sigma}{\partial S} = \frac{\partial \sigma}{\partial \epsilon} \frac{\partial \epsilon}{\partial S} = \frac{\partial \sigma}{\partial \mu} \frac{\partial \mu}{\partial \epsilon} \left( \frac{\partial S}{\partial \epsilon} \right)^{-1} \quad (22)$$

Clearly  $\frac{\partial S}{\partial \epsilon} = -2S_0(1 - \epsilon)$ , so

$$\frac{\partial \sigma}{\partial S} = -\frac{1}{2S_0(1 - \epsilon)} \frac{\partial \sigma}{\partial \mu} \frac{\partial \mu}{\partial \epsilon} \quad (23)$$

How do we approximate the chemical potential of the electron gas on a  $2D$  rectangular lattice? This was solved in [15], where it was shown that

$$n = \frac{1}{2ab} \left[ 1 - \exp[-\mu/T] I_0\left(\frac{2t_x}{T}\right) I_0\left(\frac{2t_y}{T}\right) \right] \quad (24)$$

where  $n$  is the filling factor and  $I_0$  the modified Bessel function of the first kind of order 0. Developing into series, taking  $t_x$  and  $t_y$  as small parameters, and limiting the development to lowest order terms, one gets the following result

$$\exp[-\mu/T] = \frac{1 - 2nab}{1 + \left(\frac{t_x^2 + t_y^2}{T^2}\right) + \left(\frac{t_x^2 t_y^2}{T^4}\right)} \quad (25)$$

Taking the natural logarithm of both sides, developing and retaining only the lowest order terms, one gets the following approximate result for the chemical potential of the electron gas on a  $2D$  rectangular lattice:

$$\mu \cong k_B T \left[ 2abn + 2(abn)^2 + \left(\frac{8}{3}\right)(abn)^3 + \left( \left(\frac{t_x t_y}{(k_B T)^2}\right)^2 - \frac{t_x^2 + t_y^2}{(k_B T)^2} \right)^4 + \dots \right] \quad (26)$$

Introducing the strain  $\epsilon$  in eq.(26) by  $a = a_0(1 - \epsilon)$  and  $b = b_0(1 - \epsilon)$ , it becomes possible to determine the derivative  $\partial \mu / \partial \epsilon$ . The derivative  $\partial \sigma / \partial \epsilon$  can (in principle) be calculated from the previously defined and calculated conductivity of the  $2D$  rectangular lattice. Combining those partial results, one gets the final approximation for  $\partial \sigma / \partial S$ , which describes the influence of high pressure on the conductivity of this particular  $2D$  lattice.

Equation (24) gives the possibility of determining the region (or point) in phase space in which the chemical potential of a  $2D$  electron gas becomes approximately equal to zero. In  $1D$  problems, the point  $\mu = 0$  corresponds to a half-filled band, and experimentally to a "clean" specimen. Inserting  $\mu = 0$  into eq.(24) it follows that

$$1 - I_0(2t_x/T) I_0(2t_y/T) - 2S_0 n (1 - \epsilon)^2 = 0 \quad (27)$$

which can be solved to give

$$n = \frac{1 - I_0(2t_x/T) I_0(2t_y/T)}{2S_0 (1 - \epsilon)^2} \quad (28)$$

This is the value of the filling factor for which  $\mu = 0$ , expressed as a function of various lattice parameters and the strain provoked by the application of pressure.

It would be interesting mathematically to determine if a point for which  $\partial \sigma / \partial S = 0$  exists in principle, or for some particular combination of material parameters. From the experimental point of view, the existence of such a point would imply that a material is not sensitive to applied pressure.

#### 4. Optics, invisibility and the HM

The electrical conductivity of a material is linked to its reflectivity. This theoretical result is known for decades and it has very interesting experimental consequences. Namely, the existence of this link opens up the possibility of calculating the conductivity from the measured values of the reflectivity. The only "ingredient" of such a calculation is some theoretical model of the material under study; in this paper we shall discuss to some extent the *HM*. Full details of this calculation have recently been discussed in [10], but some possibilities for improvement shall be presented here.

Two parameters characterize the propagation of an electromagnetic wave through an an-magnetic material. These are the dielectric function  $\epsilon(\omega)$  and the refractive index  $N(\omega)$ , with  $N(\omega) = \sqrt{\epsilon(\omega)}$  [10]. It is known from theory of optics that

$$\begin{aligned}\epsilon &= \epsilon_R(\omega) + i\epsilon_I(\omega) \\ N(\omega) &= n(\omega) + iK(\omega)\end{aligned}\quad (29)$$

$K(\omega)$  denotes the extinction coefficient. Reflectivity of a material is defined by the following quotient [10]

$$R(\omega) = \frac{(n-1)^2 + K^2}{(n+1)^2 + K^2}\quad (30)$$

Algebraic manipulation, discussed in [10], leads to

$$K^4 + K^2 \times \left[1 - \frac{4\pi\sigma_I}{\omega}\right] - \left(\frac{2\pi\sigma_R}{\omega}\right)^2 = 0\quad (31)$$

The final expression for the reflectivity is [10]

$$R(\omega) = \frac{(2\pi\sigma_R)^2 - K\omega \times [4\pi\sigma_R - K\omega(1 + K^2)]}{(2\pi\sigma_R)^2 + K\omega \times [4\pi\sigma_R - K\omega(1 + K^2)]}\quad (32)$$

This is the expression linking the reflectivity with the real and imaginary parts of the electrical conductivity of a material. Inserting the appropriate expressions for  $\sigma_R$  and  $\sigma_I$  would lead to a long equation expressing the reflectivity as a function of various material parameters, which are experimentally measurable. This equation would be the "bridge" between the transport and optical parameters of a material. In general form, without making any reference to the *HM*, this equation is

$$R \cong \frac{-4\pi(\sigma_I^2 + \sigma_R^2) + \omega[\sigma_I - \sigma_R\sqrt{\cdot}]}{4\pi\sigma_I^2 - \sigma_I\omega + \dots}\quad (33)$$

Equations (4),(10),(11),(12) and (15) lead to the functions  $\sigma_R$  and  $\sigma_I$  for the case of a *2D* rectangular lattice. Inserting these results into the full expression for  $R$ , would give the dependence of the reflectivity on various measurable parameters of a material.

This opens up the possibility of calculating the value of the reflectivity for various values of material parameters. Turning the reasoning "upside down", it also gives the opportunity of finding the values of material parameters for which reflectivity will have any given value. The final implication is that it thus becomes possible to find values of material parameters for which reflectivity will become zero, or have any arbitrarily small value.

The importance of this conclusion is clear. We see ( by microscope, telescope or any other instrument) non-radiating objects due to the fact that they reflect light (from some source)

which is incoming on their surfaces. Logically, if the reflectivity is small, the object in question will be hardly visible, and ultimately will become invisible. The conclusion is that invisibility, or visibility with difficulty of an object, can be achieved by a careful choice of the parameters of its material, and not only by various forms of cloaking.

The experimental parameter which can be controlled most easily is the temperature of the material. This fact opens another possibility of theoretically reaching the situation of  $R \cong 0$ . It is clear that the following expression holds:

$$R(T) \cong R(T_0) + \left(\frac{\partial R}{\partial T}\right)(T - T_0) \quad (34)$$

with

$$\frac{\partial R}{\partial T} = \frac{\partial R}{\partial \sigma_R} \frac{\partial \sigma_R}{\partial T} \quad (35)$$

All the functions in his equation can be calculated using results presented in this paper. The reflectivity becomes zero at the temperature given by

$$T = T_0 - \left(\frac{\partial R}{\partial T}\right)^{-1} R(T_0) \quad (36)$$

## 5. Conclusions

The preparation of this paper was started with a double aim: to present improvements in calculations on the *HM* performed by the present author (reviewed recently in [10]), and to apply those improved results to some *2D* nano materials. In the course of writing, this plan was somewhat changed, to "just" presenting several mathematical improvements to previously performed calculations.

The improvements discussed are as follows: In the calculation of the electrical conductivity, the number of terms which intervene in various developments into series was drastically increased compared to [12]. This was made possible by improvements in computing technology compared to what was available back in 1997. The physical motivation for this calculation was enable the comparison between the experimental data and the theoretical predictions with an increased precision. The calculation of the conductivity of a *2D* rectangular lattice was made possible by a simple change of variables.

The influence of external pressure on the conductivity of this *2D* lattice was characterized by the derivative  $\partial\sigma/\partial S$ . This function was calculated, and the mechanical strain was introduced.

Finally, the link between the *HM* and optics was discussed to some extent. In this discussion we have touched the problem of invisibility, and pointed out that it can be achieved without cloaking.

It is hoped that in the future all these improvements will be used in real calculations pertaining to nano materials.

## Acknowledgments

Prepared within the research project 171005 of the Ministry of Education, Research and Technological Development of Serbia.

## 6. References

- [1] Hubbard J 1963 *Proc R Soc London* **A 276** 238
- [2] Editorial 2013 *Nature Physics* **9** 523
- [3] Celebonovic V 2014 *J.Phys.: Conf.Series* **558** 012006
- [4] Lieb E H and Wu F Y 1968 *Phys Rev Lett* **20** 1445
- [5] <http://www.itp.uni-hannover.de/~jeckelm/dmrg/>
- [6] Giamarchi T 2016 *C.R.Physique* **17** 322

- [7] Anthony J E 2014 *Nature Materials* **13** 773
- [8] Kim Y, Zhu J, Yeom B, Di Prima M, Su X, Kim J-G, Yoo S J, Uher C and Kotov N 2013 *Nature* **500** 59
- [9] Chen Yu, Lianzhou W and Jianlin S 2016 *Nano Today*, in print
- [10] Celebonovic V 2016 Hubbard Model in Materials Science: Electrical Conductivity and Reflectivity of Models of Some 2D Materials, in *Advanced 2D Materials*, A.Tiwari and A.Syvajarvi (eds.) Scrivener Publishing LLC pp.115-144
- [11] Bhalla P, Das N and Singh N 2016 *Phys Lett* **A380** 2000
- [12] Celebonovic V 1997 *Phys.Low-Dim.Struct.* **3/4** 65
- [13] Celebonovic V 1996 *Phys.Low-Dim.Struct.* **11/12** 25
- [14] Peiponen K E and Saarinen J J 2009 *Rep.Progr.Phys.* **72** 056401
- [15] Celebonovic V 2002 *Phys.Low-Dim. Struct* **9/10** 105 and preprint cond-mat/0211640

PAPER • OPEN ACCESS

## Theoretically choosing multifunctional materials

To cite this article: V Celebonovic and M G Nikolic 2019 *J. Phys.: Conf. Ser.* **1186** 012001

View the [article online](#) for updates and enhancements.



**IOP | ebooks™**

Bringing you innovative digital publishing with leading voices to create your essential collection of books in STEM research.

Start exploring the collection - download the first chapter of every title for free.



# Theoretically choosing multifunctional materials

V Celebonovic and M G Nikolic

LEX Laboratory, Inst of Physics, Univ. of Belgrade, Pregrevica 118, 11080 Zemun-Belgrade, Serbia

E-mail: vladan@ipb.ac.rs

**Abstract.** The aim of this paper is to discuss the possibility of theoretically engineering multifunctional nanomaterials. The calculations were performed for 1D and 2D nanomaterials by using results obtained within the Hubbard model (HM). The main results of the HM are briefly reviewed. The conclusion is that the approach taken in this paper is a distinct improvement over those in the literature. In the present paper results of applications of the HM are directly used in examples of engineering nanomaterials. On the other hand, in the literature calculations were performed by ab initio methods and then fitted to the form of the Hamiltonian of the HM.

## 1. Introduction

This paper is devoted to the problem of theoretically predicting values of parameters of multifunctional materials. It seems appropriate to start by defining these materials. Multifunctional materials can be defined as the materials which perform multiple functions in a system to which they belong [1]. They can exist naturally, but they can also be artificially synthesized. The probably best known natural multifunctional material is the human skin.

Multifunctional nanomaterials offer interesting possibilities for applications. A recent list [1] shows as much as 11 areas of human activity in which multifunctional materials have important impact.

Just as an illustration, note that applications of multifunctional nanomaterials in medicine are particularly interesting. A recent example is a drug called Kadcyla produced by the chemical industry Roche. In it, two materials in the form of nanoparticles which are separately known to be cancer-toxic (called transtuzumab and DM1) are joined together and sent to find and destroy HER2 positive cancer cells. Details are available at <http://www.roche.com>.

In the example just mentioned, and in principle in any attempt of applying nanomaterials, there arises a practical question: how does one choose parameters of a multifunctional material? Experimentally, one could proceed by the "trial and error" method until reaching a satisfactory result. There is also the theoretical approach of modeling a material within some particular model. The calculations to be presented in this paper will be performed within the Hubbard model (HM).

Before embarking on the calculations, there are two questions which should be tackled to some extent. In view of the fact that large calculational projects, such as NOMAD (Novel Materials Discovery) (<http://nomad-coe.eu>), exist is it useful to perform small scale calculations like those to be presented here? Another big material science project is the Materials Genome



Initiative (<http://www.mgi.gov>). Concerning the Hubbard model, is it applicable to modeling of materials?

Concerning NOMAD, the answer is positive. It is true that NOMAD guarantees high precision in treatment of any problem in material science. However, attempting to achieve the same goal by using any particular model is certainly easier as it bypasses problems related to access to NOMAD. Therefore, calculations discussed here can be treated as a first approximation to work possible by using NOMAD. A similar conclusion applies to MGI, which also has a data repository.

A bibliographical search concerning the applicability of the Hubbard model to modelling materials gave encouraging results. A search with the keywords "hubbard model material" on <http://prola.aps.org> published "anytime" performed beginning October 2018 gave 9218 results. The clear implication is that this model can be applied to modelling materials. Classified as "most relevant" in this list is [2]. In this paper, the authors used *ab initio* electronic structure methods to design a material whose Hamiltonian matches as closely as possible that of the single band Hubbard model. Another interesting paper from this list is [3]. That paper is devoted to the computation of the ground-state phase diagram of the Hubbard model.

The next two sections contain a brief reminder of the main results of the HM needed in this paper, while the rest of the paper is devoted to the application of the HM in the choice of parameters of multifunctional nanomaterials.

## 2. The Hubbard model

This is a reminder of the main equations of the HM, while the reader interested in details is referred to [4,5]. See also [6].

The basic point for the study of any physical system is its Hamiltonian. For a 1D system, within the second quantisation formalism, the Hamiltonian has the following form

$$H = -w \sum_{l,\sigma} (c_{l,\sigma}^+ c_{l+1,\sigma} + c_{l+1,\sigma}^+ c_{l,\sigma}) + U \sum_j n_{j,\uparrow} n_{j,\downarrow} \quad (1)$$

The following symbols have been used:  $w$  denotes the hopping and  $U$  is the interaction energy of a pair of electrons having opposite spins on a lattice site  $j$ . Symbols of the form  $c_{l,\sigma}^+$  denote a creation operator for an electron having spin  $\sigma$  on lattice site  $l$ , while  $c_{l+1,\sigma}$  is the annihilation operator for an electron at lattice site  $l + 1$  with spin  $\sigma$ . The current operator is

$$j = -iw \sum_{l,\sigma} (c_{l,\sigma}^+ c_{l+1,\sigma} - c_{l+1,\sigma}^+ c_{l,\sigma}) \quad (2)$$

Knowing the Hamiltonian of a system enables the calculation of its transport properties. One of the methods for such calculations is the so called "memory function" approximation (MFA), developed in the 1970s as a consequence of previous work of Kubo. The MFA is extensively discussed in the literature (some references are given in [4]). Without repeating this discussion, we shall just state the final result for the electrical conductivity of a 1D system [4].

The final result for the electrical conductivity is given by

$$\sigma_R(\omega_0) = (1/2\chi_0)(\omega_P^2/\pi)[\omega_0^2 - (bw)^2]^{-1}(Uw/N^2)^2 S \quad (3)$$

and the symbol  $S$  denotes the following function

$$\begin{aligned} S = & 42.49916(1 + \exp(\beta(-\mu - 2w)))^{-2} + 78.2557(1 + \exp(\beta(-\mu + 2w \cos(1 + \pi))))^{-2} \\ & + \frac{bw}{\omega_0 + bw} (4.53316 \times (1 + \exp(\beta(-\mu - 2w)))^{-2} \\ & + 24.6448(1 + \exp(\beta(-\mu + 2w \cos(1 + \pi))))^{-2}). \end{aligned} \quad (4)$$

The symbol  $\mu$  denotes the chemical potential of the electron gas on a 1D lattice [6],  $n$  is the filling factor of the lattice,  $N$  the number of sites in the lattice,  $b$  a numerical constant,

$$\mu = \frac{(\beta w)^6 (ns - 1) |w|}{1.1029 + 0.1694(\beta w)^2 + 0.0654(\beta w)^4} \quad (5)$$

### 3. Optics

Relations between the electrical conductivity and reflectivity of solids are known since the middle of the twenties of the last century. These are the so called Kramers-Kronig (KK) relations. Detailed considerations on the KK equations can be found, for example, in [6,10]. In the context of this paper, there is one logically arising question: can these relations be used in theoretically choosing a nano-material? The answer is, as the reader may suppose, positive.

Skipping the details of the calculation (see [6] for example) it can be shown that the reflectivity is given by

$$R = \frac{(2\pi\sigma_R)^2 - K\omega[4\pi\sigma_R - K\omega(1 + K^2)]}{(2\pi\sigma_R)^2 + K\omega[4\pi\sigma_R + K\omega(1 + K^2)]} \quad (6)$$

and

$$K_{1,2}^2 = \frac{4\pi\omega\sigma_I - \omega^2 \pm [(4\pi\omega\sigma_R)^2 + (\omega^2 - 4\pi\omega\sigma_I)^2]^{1/2}}{2\omega^2}, \quad (7)$$

where the symbols  $\omega, \sigma_R$  and  $\sigma_I$  denote the frequency, the real and imaginary components of the conductivity. These two expressions are applicable to 1D materials. Their applicability can be extended to 2D materials by a change of variables:  $\sigma = [\sigma_x^2 + \sigma_y^2]^{1/2}$  [9].

The KK relations can be applied in several ways in engineering a nanomaterial. For example, what parameters a nanomaterial must have in order to have reflectivity close to zero? Or, if a material has a particular value of  $t_x$  what value of  $t_y$  must it have in order to have a particular value of the reflectivity?

### 4. Choosing multifunctional materials

Every part of any system performs a certain task within the domain of possibilities of the system as a whole. If a part of a system, or the system as a whole can perform multiple tasks, it is called a *multifunctional system*. Going a step further, a nanomaterial is called a *multifunctional nanomaterial* if its behavior can be controlled by the application of various external fields [8].

#### 4.1. 1D material under a thermal field

One of the parameters of a material is the chemical potential of the electron gas. In the 1D case, it is given by eq.(5), and discussed in more detail [4,6]. It was shown by Lieb and Wu [7] that the chemical potential is zero for half filling, regardless of the temperature. Speaking from the experimental point of view, the half-filled case means that the material is pure (not doped) and that it is not a conductor of electricity [6].

Taking into account the fact that in real experiments materials are at some non-zero temperature, the obvious question is: can the chemical potential become close to zero for the lattice filling factor  $n$  different from one? A positive answer to that question would have some interesting consequences in the applications of the HM.

Take equation (5) and arbitrarily normalize the chemical potential to  $\mu = 1$  at the point  $n = 1.1, T = 116K$  and  $t = 0.02$ . Repeating the same calculation for  $n = 1.3$ , and then plotting the two graphs, one gets figure 1. Figure 1. shows that for  $T \geq 180 K$ , the chemical potential tends approximately to zero.

This is a difference with the standard results of the HM, which state that the chemical potential and the electrical conductivity are zero for  $n = 1$ . In fact, this means that the

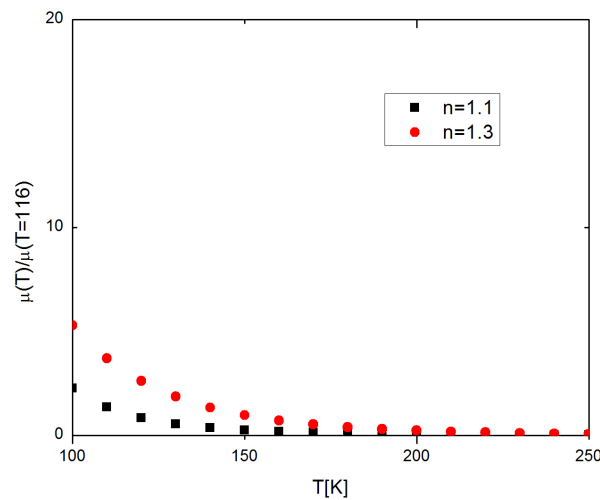


**Figure 1.** The chemical potential of 1D electron gas for  $n = 1.1$  and  $n = 1.3$

material becomes electrically neutral at values of temperature above some limiting value of the temperature. In the context of choosing a nano-material this can be taken to imply that designing an electrically neutral material can be achieved by heating it above a limiting value of the temperature.

#### 4.2. the conductivity of a 1D material under a thermal field

As described in the preceding section, a prerequisite for the calculation of the electrical conductivity of any physical system is the knowledge of its Hamiltonian. A frequent choice for such calculations is the memory function method. Applying this approach to the 1D Hubbard model, and using the formalism of second quantisation, one gets expressions (3)-(4) for the electrical conductivity.

The chemical potential, which contains the dependence on the doping and temperature, is given by equation (5). It is generally agreed that equations (3)-(5) can be applied to 1D systems of correlated electrons, such as low dimensional organic conductors and/or superconductors. The following two figures illustrate the behavior of systems of 1D correlated electrons under the control of a thermal field (i.e., under variable temperature).

Figure 2 shows the characteristic shape of the  $\sigma(T)$  curve. As the position of the maximum is sharp, this result opens up (in principle) the possibility of theoretically choosing a nanomaterial which will have a predetermined position of the maximum conductivity in the  $(\sigma, T)$  plane.

Experimentally speaking, the filling factor  $n$  denotes the doping of a material. Figure 3 shows that exposing a material to a varying doping field changes its conductivity in a characteristic manner, and thus opens up the possibility of designing a material with a specified values of the couple  $\sigma, n$ .

Figure 4 is even more interesting, because it shows the behavior of the conductivity of a material under the influence of two variable fields: the thermal field, and (what could be called) the hopping field, under constant doping  $n$ . In the region  $T < 180$  K the relative differences of the conductivities for the largest and smallest values of the hopping  $t$  amount to as much as 50 per cent. Using calculations like those which led to this figure, one can theoretically design

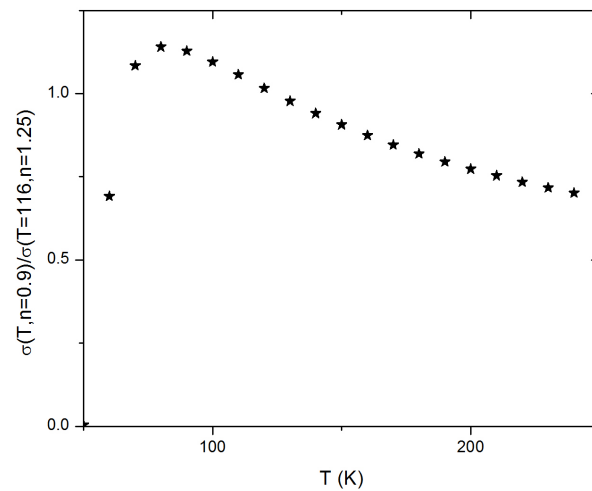


**Figure 2.** The normalized elect. conduct. of 1D electron gas for  $n = 0.9$

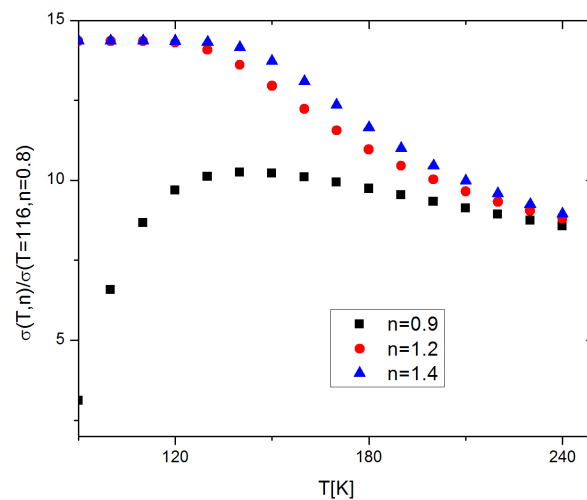


**Figure 3.** The normalized conductivity for three values of  $n$  for a 1D material

materials with predetermined values of the conductivity for certain values of the doping and/or hopping. Practically, one would have to choose pairs of  $(n, t)$  values, or fix  $n$  and vary  $t$  and then calculate the conductivity.

#### 4.3. The two dimensional materials

The HM is at present solved only for the case of 1D [7]. In the special case of a 2D rectangular lattice where the conductivities along the axes are mutually independent and denoted by  $\sigma_x$  and

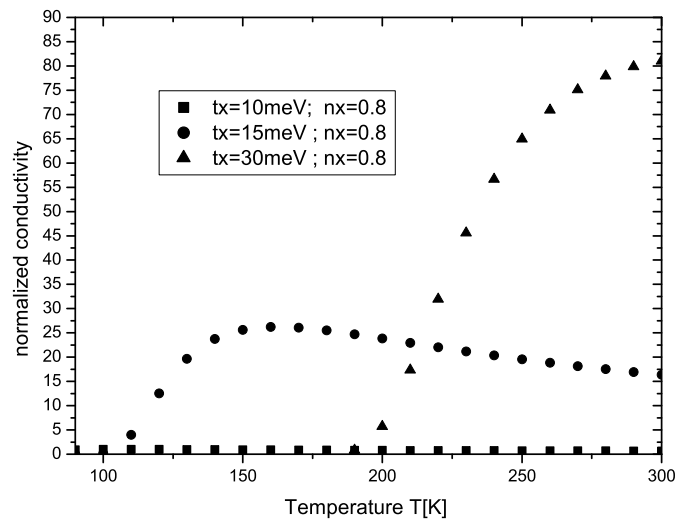


**Figure 4.** The normalized conduct. of a 2D rectang. lattice for 3 values of  $t$

$\sigma_y$ , the conductivity of the lattice can be expressed as

$$\sigma = [\sigma_x^2 + \sigma_y^2]^{1/2}. \quad (8)$$

Theoretically choosing the parameters of a system having such a link between the conductivities of its parts may seem complicated. In fact, this 2D problem reduces to two 1D problems along the two lattice axes.

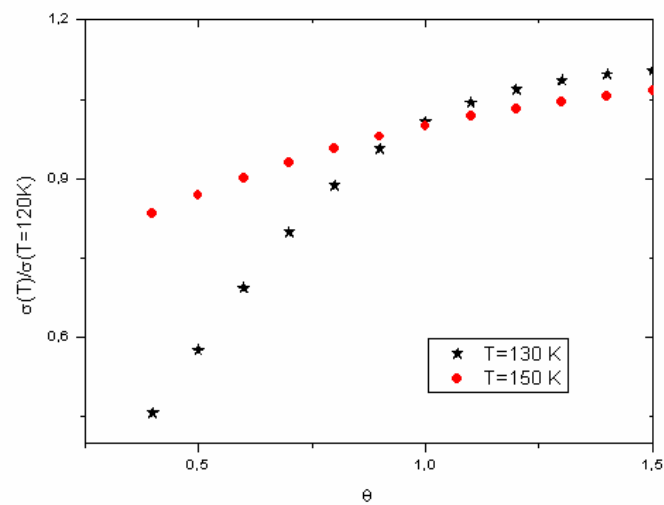


**Figure 5.** The normalized reflectivity of a 2D rectangular lattice for 2 values of  $T$

Figure 5 taken from [6] is an example of the influence of external fields on a rectangular 2D lattice which is moderately useful for theoretically choosing a nanomaterial. It represents the dependence of the normalized electrical conductivity of a 2D lattice on the ratio of the filling factors along the two lattice axes. This ratio is symbolized by  $n_y/n_x = \theta$  and the parameters for which this figure was calculated are available in [6]. The point which could be useful in choosing a nanomaterial is here the turning point of one of the curves.

#### 4.4. designing the optical properties of nano materials

An interesting, but complicated way of engineering a nano material is to predict theoretically the value of its reflectivity and link it to the values of various material parameters. It can be shown ([6] and references given there) that the reflectivity can be expressed as the following sum

$$R \cong 1 - 2\left(\frac{K\omega_0}{\pi\sigma_R}\right) + 2\left(\frac{K\omega_0}{\pi\sigma_R}\right)^2 - \dots \quad (9)$$

This expression for the reflectivity implicitly depends on the dimensionality of the system through  $\sigma_R$  and  $K$ . An illustrative example of the temperature dependence of the reflectivity is presented on fig.6.

Note an interesting detail on this figure, useful for theoretically choosing a nano material. The derivative  $dR/dT$  drastically changes at the temperature of approximately  $T \cong 70K$ . The position of this point can be theoretically predicted, and it depends on the values of the hopping  $t$  and the filling factor  $n$ . This means that fixing the temperature and which  $R$  changes, one can theoretically determine the values of  $t$  and  $n$ .

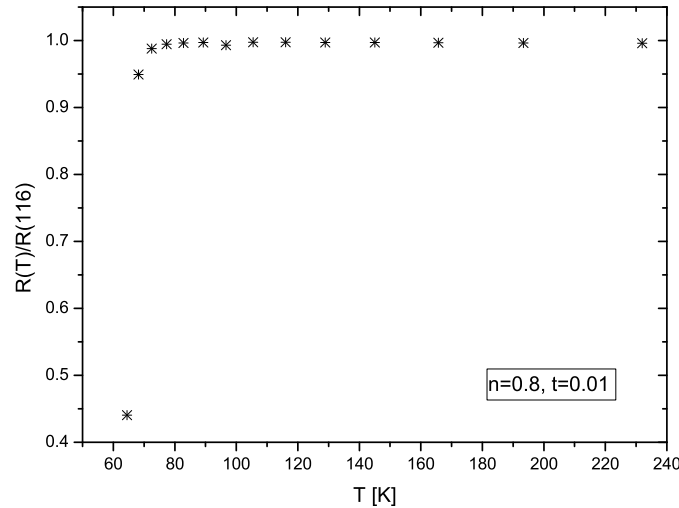


**Figure 6.** The reflectivity of 1D HM for  $n = 0.8$   $t = 0.01$

The first step was the calculation of the electrical conductivity. It was normalized to  $\sigma_R = 1$  for  $n = 0.8$ ,  $t = 0.005$  eV and  $T = 116$  K. In the case of a 2D material, two important ratios influence the results of calculations discussed here. These are the ratio of the conductivities, denoted by  $\sigma_{Ry}/\sigma_{Rx} = \Gamma$ , and the ratio of the filling factors along the two lattice axes, symbolized by  $n_y/n_x = \theta$ . Note that all the 2D materials discussed here imply materials with a square lattice.

The dependence of the reflectivity under constant temperature of a 2D lattice on the parameter  $\theta$  is shown on the following figure, taken from [6]. Note that the decrease of  $\theta$  leads to a decrease of the value of  $R$ . In practical terms, this means that decreasing the ratio of filling factors along the two lattice axes leads to increasing difficulties in seeing the specimen. This conclusion could have implications in work on invisibility cloaks.

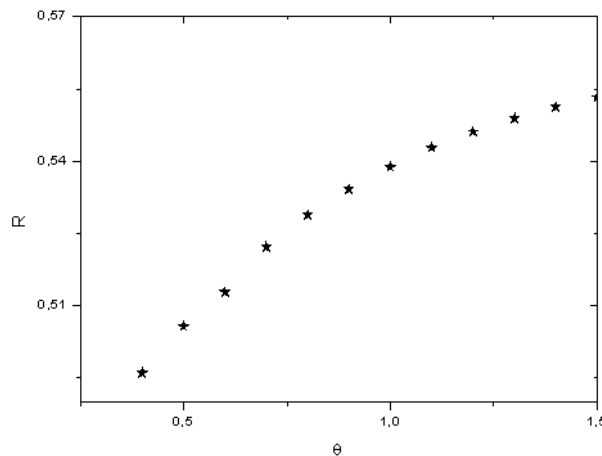


**Figure 7.** The reflectivity as a function of  $\theta$  for  $T = 150K$

## 5. Piezoresistivity under strain

In various situations, both in laboratory work and practical applications, the need may arise for a material which becomes better conductor of electricity when exposed to a strain  $\epsilon$ . Such a material can be chosen theoretically, but the situation is slightly more complex than in the cases discussed so far.

Namely, in such a situation one has to take into account the dependence of the hopping  $t$  on the strain. Using results on the overlap of atomic wave functions, in [11], the dependence of the hopping  $t$  on the interatomic distance  $r$  was approximated as

$$t = t_0[1 + r + (1/3)r^2] \exp(-r) \quad (10)$$

where  $r$  is measured in the units of Bohr radius.

As a practical application, in which theoretical choice of a material is needed, let us consider an instrument based on piezoresistivity [4]. In this case the problem we encounter can be stated as "At a given temperature  $T$  what value of the hopping  $t$  must the material have, in order to achieve some chosen value of the sensitivity  $G$ ?"

The sensitivity of a sensor based on piezoresistivity is defined as

$$G = -\frac{1}{\sigma} \left( \frac{\partial \sigma}{\partial \epsilon} \right) \quad (11)$$

where  $\sigma$  is the conductivity and  $\epsilon$  the strain. The dependence of  $G$  on the strain has been studied in [4]. Clearly, the lower the temperature the more pronounced this dependence becomes.



## 6. Compressibilities

What would be the result of attempting to engineer a nanomaterial under the influence of high pressure? To render the problem more complex, imagine that the nanomaterial in question is a compound, consisting of two specimens of nanomaterials with compressibilities of different signs. This combination is in principle possible [12]. Imagine an experiment in which two materials having different coefficients of thermal expansion are fixed together. If such a combination is heated, it will bend to one side. A similar situation will occur if the two nanomaterials are subjected to high pressure and have compressibilities of different signs [12].

The isothermal compressibility is defined as

$$\beta_T = -\frac{1}{V} \left( \frac{\partial V}{\partial p} \right)_T \quad (12)$$

where all the symbols have their standard meanings. The pressure  $P$  and volume  $V$  of a material are linked through the equation of state. Choosing an appropriate equation of state for a given nanomaterial is a delicate research subject. See, for example, [13].

In the case of a nanomaterial distributed along a straight line, the problem returns to those discussed earlier. However, if the materials are distributed along a curved line, the solution is strongly dependent upon the compressibilities and their signs. A detailed consideration of this problem is in preparation.

## 7. Conclusions

This paper attempted to answer an apparently simple question - is it possible to choose parameters of a nano-material theoretically so that they have certain pre-selected values? This choice of parameters is dependent on the theoretical model chosen to describe the material under study.

The calculations discussed in the present paper were performed for 1D and 2D materials within the Hubbard model. Calculations reported here are more direct than those in [2,3]. For example, in [2] the calculations were performed by *ab initio* methods, and then the Hamiltonian was matched to the Hamiltonian of the HM. On the other hand, in the present paper results of direct applications of the HM and the memory function method were used to demonstrate possibilities of engineering nano-materials, which is a distinct advantage. It was shown on several examples that it is possible to engineer multifunctional nano-materials by calculating their conductivity, reflectivity and sensitivity for piezoresistivity, making calculations within the Hubbard model a viable way in theoretically modelling nanomaterials.

## Acknowledgments

Prepared within the research projects 171005 and 171038 of the Ministry of Education, Research and Technological Development of Serbia. V C is grateful to ICTP (Trieste, Italy) for their hospitality and use of the libraries.

## References

- [1] <https://www.e-education.psu.edu/eme807/node/698>
- [2] Griffin S M Staar Schulthess et al 2016 *Phys. Rev. B* **93** 075115
- [3] B-Xiao Zheng and Chan G K L 2016, *Phys. Rev. B* **93** 035126
- [4] Celebonovic V and Nikolic M G 2018 *J. Low Temp. Phys.* **190** 191
- [5] Giammarchi T 2017 *Nature* **545** 414
- [6] Celebonovic V 2016 in *Advanced 2D Materials, edited by A Tiwari and M Syvajarvi* Advanced Materials Series, (Scrivener Publishing LLC) chap. 4
- [7] Lieb E H and Wu F Y 1968 *Phys. Rev. Lett.* **20** 1445
- [8] Suzdalev I P 2009 *Russ. Chem. Rev.* **78** 249
- [9] Celebonovic V 2010 *J. Phys. Conf. Ser.* **253** 012004.

- [10] Peiponen K E and Saarinen J J 2009 *Rep. Progr. Phys.* **72** 056401
- [11] Celebonovic V 2014 *J. Phys. Conf. Ser* **558** 012006
- [12] Gatt R and Grima J N 2008 *Phys. Stat. Sol. RRL* **2** 236
- [13] Chandra J and Kholiya K 2016 *J. Taibah Univ. Science* **10** 386

# The origin of impact craters: some ideas

Vladan Celebonovic

LEX Laboratory, Inst. of Physics, Univ. of Belgrade, Pregrevica 118, 11080 Belgrade, Serbia  
vladan@ipb.ac.rs

(Submitted on 31.08.2019. Accepted on 24.10.2019)

**Abstract.** The surfaces of solid objects in the planetary system are dotted by impact craters. From the viewpoint of condensed matter physics, the problem of the origin of these craters can be expressed in the following way: in a material of given chemical composition, there exists a hole of given dimensions. Assuming that this hole is a consequence of an impact, what can be concluded on the impactor? This problem can be analyzed in two ways: by using scaling laws and by the standard laws of condensed matter physics. The aim of this paper is to present basic notions of the two approaches, and give some of the results.

**Key words:** impacts craters, condensed matter, scaling laws

## 1. Introduction

Observation, ranging from those performed by the earliest telescopes to current work by space probes, shows that surfaces of many solid bodies in the planetary system are filled with craters. A part of them are of volcanic origin and they are outside the scope of this paper. The subject of this paper are impact craters; that is craters which are due to impacts of smaller solid bodies (often called impactors) in the surfaces of larger objects in the Solar system. Some impact craters have halos (Bart et al., 2019). Physically, the impactors are remnants from the epoch of formation of the Solar system (for example Perryman, 2011, Carlson, 2019).

According to the data base kept at the University of New Brunswick in Canada at <http://www.passc.net/>, at present there are 190 known impact craters on the Earth. Due to their number, their purely scientific interest, but also the possible dramatic consequences which an impact could have, the study of impact craters has become a well developed sub-field of planetary science.

The most widely known impact crater is certainly the Barringer crater in the Arizona desert, which is mentioned in publications ranging from elementary school textbooks to scientific papers. A much less studied impact structure seems to exist in the Falkland Plateau, north-west of the West Falkland island. Seismic reflection profiles indicate the presence of a large roughly circular basin with a diameter of approximately 250 km. The best explanation of this structure is the presence of a large buried impactor (Rocca et al., 2016). A much more recent impact event, which did not produce a crater, is the one of 15 February 2013, when a small asteroid entered the atmosphere over the city of Chelyabinsk in Russia. There were no victims, but a large number of people have been injured by shattered glass.

Finally, at the time of this writing (July 2019) there appeared an analysis concerning the possibility of Earth impact by asteroid 2009FD. The result, obtained using recent astrometry and radar data, is that the main impact possibility in 2185 is ruled out, but there remains a very small possibility in 2190 (DeVigna et al., 2019).

The aim of this paper is to present an introduction to two different theoretical approaches to the problem of impact craters. The second section is devoted

to the approach using scaling theory, while the third part uses standard condensed matter physics. Both approaches treat the same problem: having data on the target and the crater, what can be concluded on the impactor and the impact?

## 2. The scaling theory

Predicting the outcome of one event from the result of another is often called *scaling*. The relation used in this predicting is called the *scaling law*, and the parameters which change between the two events are named *scaled variables*. The need for the application of scaling in the problem of impact craters is obvious: impact craters in reality have diameters of the order of meters to kilometers, while craters in terrestrial experiments are smaller (Holsapple,1993).

There exist three ways in which the form of scaling laws can be predicted: these are impact experiments, analytical calculations and approximate theoretical calculations. The principle of impact experiments is simple, so it may be imagined that they are simple to perform. There is, however, a problem in impact experiments: currently accessible impactor velocities in laboratories are smaller than theoretically expected collision velocities (for example, Hibbert et al., 2017). In principle, projectiles of various mass and composition are fired with different speeds into targets of different composition. The aim is to measure diameters of the resulting craters as a function of the impact velocities and the chemical compositions of the target and the impactor. A detailed presentation of one of the actual installations for impact experiments, at the University of California in Davis, can be found at [http://geology.ucdavis.edu/read/stewart\\_shockwave](http://geology.ucdavis.edu/read/stewart_shockwave).

Analytical calculations on the impacts are founded on the laws of balance of mass, momentum and energy, with the addition of the equation of state (*EOS*) of the material of the target and of the impactor. The problem with this approach are the details in the knowledge of the (*EOS*) and thermodynamic potentials of the target and of the impactor. Work in this direction will be somewhat easier in the future, owing to results of big calculational projects in material science. Examples of such projects are the Materials Genome Initiative <http://www.mgi.gov> in the US and the mainly European project Novel Materials Discovery <http://www.nomad-coe.eu>.

These projects give material characteristics as a function of various parameters. However, the choice of a material for any particular astronomically interesting case is beyond their scope. In terrestrial applications it is (in principle) possible to collect pieces of the impactor and of the target. However, in the case of asteroid(s) moving towards the Earth, the only way of determining their composition is spectroscopy. Problems can arise if an asteroid is made up of a material with small albedo, which implies that the composition will be determined with a large relative error. Assuming that the impactor is sufficiently massive, and that the speed of impact is sufficiently high, in the moment of impact there occurs a phase transition *solid*  $\rightarrow$  *gas* or even *solid*  $\rightarrow$  *plasma*. After a rapid cooling, the result of the impact can be analyzed within solid state physics.

The basic idea of the approximate theoretical solutions is the so called "point source model". Simply stated, the phase immediately after impact is

described as a "point source" of shock waves propagating through the target. It was developed near the middle of the last century for analysis of nuclear explosions.

Attempting to predict the volume  $V$  of a crater formed in an impact is the simplest case of application of scaling laws in these problems. Denote the radius of the impactor by  $r$ , its velocity by  $v$  and density by  $\rho_1$ . The target has density  $\rho$ , gravitational acceleration at the surface  $g$ , and it is made up of material with material strength  $X$ . Material strength is defined as the ability of a material to withstand load without failure. In that case:

$$V = f[\{r, v, \rho_1\}, \{\rho, X\}, g]. \quad (1)$$

The first three variables describe the impactor, the following two - the material making up the planet and the last one - the surface gravity of the planet. Scaling laws can be derived from this expression by dimensional analysis.

It can be shown that equation (1) leads to

$$\frac{\rho V}{m} = f_1\left[\frac{gr}{v^2}, \frac{X}{\rho v^2}, \frac{\rho}{\rho_1}\right], \quad (2)$$

where  $m = \frac{4\pi}{3}\rho_1 r^3$  is the mass of the impactor. The quantity on the left side is the ratio of the mass of the material within the crater to the mass of the impactor. It is usually called cratering efficiency and denoted by  $\pi_V$ . The first term in the function is the ratio of the lithostatic pressure  $\rho g r$  to the initial dynamic pressure  $\rho v^2$ , generated by the impactor. The lithostatic pressure at a certain depth is defined as the pressure exerted by the material above it. This ratio is denoted by  $\pi_2$ ; the second term is the ratio of the material strength to the dynamical pressure, denoted by  $\pi_3$ . The final term is the ratio of the mass densities. If all the parameters of eq.(2) were known, or could be determined, it would not be too difficult to determine the volume of an impact crater. Finding the general solution of this equation is an open problem. As a consequence, solutions of this equation are usually studied in two limiting cases: the "strength" regime and the "gravity" regime.

The main difference of these two situations is in the value of the ratio of strength of the surface material and the lithostatic pressure. The "strength" regime is the situation in which the strength of the surface material is larger than the lithostatic pressure, which implies impactors with diameters of approximately one meter (Holsapple,1993). This means that

$$\frac{\rho V}{m} = f_1\left[\frac{X}{\rho v^2}\right], \quad (3)$$

where it was assumed that the ratio of the densities is approximately one. In this regime, the volume of the impact crater increases linearly with the volume of the impactor, its mass and its energy. Any dimension of the crater increases with the radius of the impactor. In the opposite case, when the diameter of the impactor is of the order of a kilometer or more, the lithostatic pressure is bigger than the material strength, meaning that

$$\frac{\rho V}{m} = f_1\left[\frac{gr}{v^2}\right]. \quad (4)$$

This is the definition of the "gravity" regime. Various experiments (discussed in Holsapple, 1993) have been performed on the dependence of  $\pi_V$  on  $\pi_2$ , the result being an exact power law. This can be explained, as discussed in (Holsapple, 1993), by the assumption that whenever there is a dependence on the impactor size and speed, it is actually the dependence on its kinetic energy. This idea was used in the early sixties, in scaling from a nuclear event called "Teapot ESS" to the creation of the Meteor Crater in Arizona. For some more details on this aspect of the problem see, for example Celebonovic (2017).

### 3. Condensed matter physics

Surfaces of objects in the solar system which contain impact craters are solid. It is known that impactors are solid objects, so the ensuing question is what can be concluded about the impacts by using laws of condensed matter physics and all kinds of measurable parameters of the target. Possibilities exist, and they will be discussed using previous results of the present author (Celebonovic and Souchay, 2010 ; Celebonovic, 2013, 2017).

The first condition for the creation of an impact crater is the velocity of the impactor, which must exceed some minimal value. This was determined in Celebonovic and Souchay (2010). It was postulated in that paper that a crater will be formed if the kinetic energy of a unit volume of the impactor is equal to the internal energy of a unit volume of the material of the target. As discussed in that paper, the minimal speed of the impactor is given by

$$v^2 = \frac{\pi^2}{5\rho_1} \frac{(k_B T)^4}{\hbar^3} \left( \frac{\partial P}{\partial \rho} \right)^{-3/2}, \quad (5)$$

where  $\rho_1$  is the mass density of the impactor,  $T$  the temperature of the target, and  $P, \rho$  are the pressure and mass density of the material of the surface of the target respectively. From the point of view of condensed matter physics, this equation is physically correct. In order to test its applicability in a real astronomical situation, it was applied to the case of an impactor made of olivine  $(Mg, Fe)_2SiO_4$ . The minimal speed of this object would be 16.3 km/s. For comparison, note that the impact velocity of a real object, asteroid 99942 Apophis, is estimated to be between 13 and 20 km/s. This means that two completely different methods: celestial mechanics and condensed matter physics give mutually close results on the same problem, which is extremely encouraging.

It is stated sometimes that condensed matter physics can not be applied to impact cratering because in hyper velocity impacts the material of the target melts and can even evaporate. The final result of an impact is a crater. If the kinetic energy of the impactor is high enough, and if the target has a suitable value of the heat capacity, a consequence of the impact will be heating of the target. Heating in impacts has been studied in Celebonovic and Nikolic (2015). Depending on the kinetic energy of the impactor, the target may heat enough so as to melt, and possibly even evaporate at the point of impact. In this regime, condensed matter physics cannot be applied. Regardless of the amount of heating in the impact, the outcome is always the same: a certain quantity of material of the target gets "pushed aside" at the point of impact, implying the creation of a crater of certain dimensions. The aim of the calculations outlined

here is to draw conclusions about the impactor using measurable dimensions of the crater and various parameters of the target.

Using the vocabulary of condensed matter physics, the problem of formation of impact craters can be expressed as the following equivalent problem: how big must be the kinetic energy of the impactor in order to produce a hole of given dimensions in a target material with known parameters (Celebonovic,2013). It was assumed that the target is a crystal, that one of the usual types of bonding exists in it, and that the target does not melt as a consequence of the impact.

The calculation is based on a simple and acceptable physical idea: the kinetic energy of the impactor must be greater than, or equal to the internal energy of some volume  $V_2$  of the target. The kinetic energy of the impactor of mass  $m_1$  and speed  $v_1$  is obviously

$$E_k = \frac{1}{2}m_1v_1^2, \quad (6)$$

and the internal energy  $E_I$  consists of three components: the cohesion energy  $E_C$ , the thermal energy  $E_T$  and  $E_H(T)$  - the energy required for increasing the temperature of the material at the point of impact by an amount  $\Delta T$ . Therefore,

$$E_I = E_C + E_T + E_H(T), \quad (7)$$

and the condition for the formation of an impact crater as a consequence of an impact is

$$E_I = E_k. \quad (8)$$

Expressions for various terms in  $E_I$  exist in the literature, and are given in Celebonovic (2013). Details of the calculation are given in that paper, and the final result is

$$3k_B T_1 N \nu \left[ 1 - \frac{3}{8} \frac{T_D}{T_1} - \frac{1}{20} \left( \frac{T_D}{T} \right)^2 + \frac{1}{10} \left( \frac{T_D^2}{T T_1} \right) + \left( \frac{1}{560} \right) \left( \frac{T_D}{T} \right)^4 - \frac{1}{420} \frac{T^4}{T^3 T_1} - \frac{3\bar{u}^2 \rho \Omega_m}{n p \nu k_B T_1} \right] = \frac{2\pi \rho_1}{3} r_1^3 v_1^2. \quad (9)$$

This is the energy condition which has to be satisfied for the formation of an impact crater. Various symbols have the following meanings: the number  $N$  is the ratio of the volume of the crater to the volume of the elementary crystal cell,  $v_e$ :  $N = V/v_e$ ;  $k_B$  is Boltzmann's constant;  $T$  is the initial temperature of the target;  $T_1$  is the temperature to which the target heats;  $T_D$  is the Debye temperature of the target;  $\rho_1, r_1, v_1$  - mass density, radius and impact velocity of the projectile respectively;  $p, n$  - parameters of the interatomic interaction potential in the material of the target;  $\nu$  is the number of particles in the elementary crystal cell;  $\bar{u}$  is the speed of sound in the material of the target; and  $\Omega_m$  is the volume per particle pair.

It might seem at first glance, that eq.(9) is just a complicated expression without any physical purpose. Close inspection shows that this equation groups known or measurable parameters on the left hand side, while the right hand side contains parameters of the impactor. It means that this expression gives

the possibility of estimating parameters of the impactor from known data on the target.

As a test, this equation was applied to a well known case: the Barringer crater in Arizona. Assuming that the material of the crater is pure Forsterite ( $Mg_2SiO_4$ ), and making plausible assumptions about the other parameters of eq.(13), it was obtained that  $v_1 \cong 41$  km/s, which is far larger than existing estimates obtained by using celestial mechanics.

A possible solution is to assume that the material of the target is a chemical mixture. Suppose that only 10 percent of the material is Forsterite, and keep all the other parameters constant. This will give the value of  $v_1 \cong 15$  km/s, for the impact speed, which is much closer to the results obtained by celestial mechanics. Details of this calculation are available in Celebonovic (2013).

The calculation outlined above was performed using the notion of cohesive energy of solids, which is a very "impractical" quantity: it is defined as the energy needed to transform a sample of a solid into a gas of widely separated atoms (Marder,2010). As a consequence of this definition, it is difficult to measure experimentally and it is not related to the strength of solids measurable in experiments.

A much more "practical" notion is the stress. It is defined as the ratio of the force applied on a body to the cross section of the surface of a body normal to the direction of the force. After an impact, a crater will form if the stress in the material becomes sufficiently high for the formation of a fracture.

A fracture will occur in a material, if the stress  $\sigma$  in it is greater than the critical value  $\sigma_C$  (Tiley,2004; Celebonovic,2015).

$$\sigma_C = \frac{1}{2} \left( \frac{E\chi\tau}{r_0w} \right)^{1/2}, \quad (10)$$

where  $E$  is Young's modulus of the material,  $\chi$  is the surface energy,  $\tau$  is the radius of curvature of the crack,  $r_0$  the interatomic distance at which the stress becomes zero, and  $w$  is the length of a crack which preexists in the material. Defined in this way,  $\sigma_C$  has the dimensions of pressure.

Applying the law of conservation of energy to the moment of impact leads to interesting conclusions. The kinetic energy of the impactor,  $E_k$ , is used in the moment of impact for fracturing and heating the material of the target. That is

$$E_k = \sigma_C V + C_V V (T_1 - T_0), \quad (11)$$

where  $V$  is the volume of the crater formed as a result of the impact,  $C_V$  is the heat capacity of the target material, and  $T_0$  is the initial temperature of the target. At this point, one encounters the problem of finding a suitable mathematical approximation of the shape of a crater, in order to be able to make an analytical estimate of the volume  $V$ . In accordance with experiments, the volume of the crater is approximated by

$$V = \frac{1}{3} \pi b^2 c, \quad (12)$$

where  $b$  is the radius of the "opening" of the crater and  $c$  denotes its depth. If one approximates the impactor as a sphere of radius  $r_1$ , made up of a material



of density  $\rho_1$  and having impact velocity  $v_1$ , its kinetic energy is given by  $E_k = \frac{2\pi}{3}\rho_1 r_1^3 v_1^2$ . It follows from eq.(11) that

$$T_1 = T_0 + \frac{1}{C_V} \left( \frac{E_k}{V} - \sigma_C \right), \quad (13)$$

and after some algebra (Celebonovic, 2017):

$$V = \frac{2\pi}{3} \frac{\rho_1 r_1^3 v_1^2}{\alpha C_V T_0 + \sigma_C}, \quad (14)$$

where  $T_1 - T_0 = \alpha T_0$ , with  $\alpha > 0$ . Equation (14) can be transformed into the following form

$$V = \frac{E_k}{\alpha C_V T_0 + \sigma_C}, \quad (15)$$

which shows that the volume of a crater is a linear function of the kinetic energy of the impactor.

#### 4.A Granular Target?

It was assumed throughout this paper that the surface of the target is a crystal. This is very often, but not always true. As an example, should an impact occur in a sandy desert like Sahara, the material there certainly could not be approximated as a crystal. In general terms, the question encountered here can be expressed in the following way: how do the consequences of an impact change if the material of the target is granular and not a crystal? From the point of view of condensed matter physics, this "transition" is extremely interesting.

We shall concentrate on two particular aspects: the shape of impact craters when formed in a granular material, as compared to their shape in a crystal, and changes in the quantity of energy needed to heat a granular material compared to the energy needed to heat the same amount of crystalline material for the same temperature difference. In this paper, the volume of a crater was approximated with eq.(12). On the other hand, experiments with normal incidence of a solid spherical impactor into a deep non-cohesive granular bed have shown that the profile of a crater can be fitted by

$$z = z_c + \sqrt{b^2 + c^2 r^2}, \quad (16)$$

where  $z_c$ ,  $b$  and  $c$  are fitting parameters (de Vet and de Bruyn, 2007). Inserting this expression for the profile of a crater into eq.(12), and using the same notation in both cases, one gets the following result for the difference of crater volumes formed after an impact into a crystal ( $V_1$ ) and granular material ( $V_2$ ):

$$V_1 - V_2 = \frac{1}{3}\pi z r^2 - \frac{1}{3}\pi r^2 [z_c + \sqrt{b^2 + c^2 r^2}]. \quad (17)$$

A simple calculation shows that this difference can become equal to zero for

$$z = z_c + \sqrt{b^2 + c^2 r^2} \quad (18)$$

Physically, this means that there exist some conditions of impacts which lead to craters of equal volume in crystal and granular targets, assuming that all the other conditions are the same in the two cases.

Targets similar to terrestrial granular materials have been found in the planetary system. Well known examples are asteroids 253 Mathilde and 25143 Itokawa. It was shown that both of these objects consist of loosely bound pieces, so they later got the name "rubble piles". For a recent review see (Walsh, 2018).

Rubble piles are obviously *porous*, and the the main physical parameter characterizing them is the porosity, defined as the following ratio:

$$\phi = \frac{V_V}{V_T} < 1, \quad (19)$$

where  $V_V$  denotes the volume of voids and  $V_T$  the total volume of the object. The value of  $V_T$  can be decomposed as follows:

$$V_T = V_1 + V_V = V_1 + \phi V_T, \quad (20)$$

which means that

$$V_T = \frac{V_1}{1 - \phi}, \quad (21)$$

where  $V_1$  denotes the volume of the "solid component" of  $V_T$ .

The quantity of energy needed to heat a volume  $V_T$  of a material having the specific heat  $C_V$  by a temperature difference of  $\Delta T$  is given by:

$$Q = C_V V_T \Delta T = (C_{V1} + C_{V2}) \times \frac{V_1}{1 - \phi} \times \Delta T, \quad (22)$$

where  $C_{V1}$  denotes the specific heat of the "solid component" of  $V_T$  and  $C_{V2}$  is the specific heat of the voids. Finally,

$$Q = \frac{C_{V1} + C_{V2}}{1 - \phi} V_1 \Delta T, \quad (23)$$

which is the expression for the quantity of energy needed to heat up for  $\Delta T$  a volume  $V_1$  of a solid having the specific heat  $C_{V1}$ , the porosity  $\phi$  and the specific heat of voids  $C_{V2}$ .

The value of the specific heat  $C_{V1}$  depends on the chemical composition of the material. If the composition is known, then this value can either be measured or calculated. More interesting is the problem of the specific heat of the voids, denoted here by  $C_{V2}$ . The unknown quantity here is the composition of the voids. If they contain only vacuum, and if there is no source of thermal radiation within the voids, the specific heat  $C_{V2}$  will be zero. However, if the voids are filled with some gas, then the value of  $Q$  will depend on the ratio of the two specific heats.

How does this expression compare with the result for a pure solid? Using eq.(21), simple reasoning shows that

$$Q = Q_S + C_{V2} V_T \Delta T, \quad (24)$$

where  $Q_S$  is the quantity of energy needed to heat a "pure" solid. Clearly, this result strongly depends on the values of  $C_{V2}$  and the porosity  $\phi$ . The implication is that some more energy is needed to heat up a porous than a non-porous material, with all the parameters being the same. Obviously, the closer the value of  $\phi$  is to 1, the bigger the value of  $Q$  will be.

## Conclusion

In this contribution we have presented in some detail two approaches to the problem of impact craters on the surfaces of solid objects in the planetary system. One is the scaling theory, while the other is standard condensed matter physics. Both of these approaches have the same aim: using existing laboratory, field and observational data and relevant laws of physics, draw as much conclusions as possible on the impacts and the impactors.

Scaling theory attempts to link the craters of "celestial" origin with those resulting from man made explosions. The good side of this approach is generality, but the "minus" is the problem of treatment of phase transitions.

The approach founded on standard condensed matter physics is based on well known laws, but also has a weak point (at least one). It can treat either slow impacts or "not very massive" projectiles.

Both approaches give useful contributions to the problem, but they are both in need of improvement in the future.

## Acknowledgement

This study was performed within the project 171005 of the Ministry of Education, Science and Development of Serbia. The author is grateful to the referee for useful comments.

## References

- Bart, G.D., Daubar, I.J., Ivanov, B.A., Dundas, C.M. and McEwen, A.S., 2019, *Icarus* 328, 45  
 Perryman, M., 2011, *preprint arXiv 1111:1286*  
 Carlson R.W., 2019, *Science* 365, 243  
 Celebonovic, V. and Souchay, J., 2010, *Publ. Astron. Obs. Belgrade* 90, 205.  
 Celebonovic, V., 2013, *Rev. Mexicana de Astron. y Astrofis.* 49, 221.  
 Celebonovic, V., 2015, *J. Earth Sci. and Engineering* 5, 44 and preprint arXiv 1403.0862 at [www.arXiv.org](http://www.arXiv.org)  
 Celebonovic, V. and Nikolic, M.G., 2015, *Int. J. Thermophys.* 36, 2916.  
 Celebonovic, V. 2017 in *Horizons in World Physics*, editor Albert Reimer 291, 251, ISBN 978-1-53611-008-1, Nova Science Publishers Inc., New York  
 Del Vigna, A., Roa, J., Farnocchia, D. et al, 2019, *Astron. Astrophys.* 627, L11  
 Hibbert, R., Cole, M.J., Price, M.J and Burchell, M.J., 2017 *Procedia Engineering* 204, 208  
 Holsapple, K.A., 1993 *Ann. Rev. Earth Planet. Sci.* 21, 333  
 Marder, M.P., 2010, *Condensed matter Physics*, John Wiley and Sons, Hooken, NJ, p. 295  
 Rocca, M.C.L., Rampino, M.R. and Baez Presser, J.L., 2017 *Terra Nova* 29, 233  
 Tiley, R., 2004, *Understanding Solids: The Science of Materials*, John Wiley and Sons, Hoboken, NJ, p. 548.  
 Walsh, K.J., 2018, *Ann. Rev. Astron. Astrophys.* 56, 593.